UCSF
UC San Francisco Electronic Theses and Dissertations

Title
Mechanism of a memory-enhancing inhibitor of the integrated stress response

Permalink
https://escholarship.org/uc/item/9458k63d

Author
Anand, Aditya

Publication Date
2020

Supplemental Material
https://escholarship.org/uc/item/9458k63d#supplemental

Peer reviewed|Thesis/dissertation

eScholarship.org Powered by the California Digital Library
University of California

Mechanism of a memory-enhancing inhibitor of the integrated stress response

by
Aditya Anand

DISSERTATION
Submitted in partial satisfaction of the requirements for degree of
DOCTOR OF PHILOSOPHY

in

Biochemistry and Molecular Biology

in the

GRADUATE DIVISION
of the
UNIVERSITY OF CALIFORNIA, SAN FRANCISCO

Approved:

DocuSigned by:
Peter Walter
9C44B4D1D50740D...

Peter Walter

Chair

DocuSigned by:
Geeta Narlikar
[illegible]43B...

Geeta Narlikar

DocuSigned by:
Jonathan Weissman
[illegible]4E2...

Jonathan Weissman

DocuSigned by:
ADAM FROST
1E2FF75D7B5A48F...

ADAM FROST

Committee Members

Dedicated to my family

Cheyyur Jaya and Aruna Anand

ACKNOWLEDGEMENTS

The completion of a doctoral degree represents a combination of independent effort and the support of a broad community. Here, I will do my best to convey the deep gratitude I feel for all those who have supported me on this journey.

First, I would like to thank my parents, Cheyyur Jaya Anand and Aruna Anand, for their unfailing generosity and support. They have made immense sacrifices to help me achieve my goals, including but not limited to investing their time and finances in my education, and moving twice to a new country in search of a better life for our family. For this, I am grateful beyond words.

Next, I would like to thank my friends who have supported me on this journey since before I began graduate school. The following people deserve special mention: Shirley Pan, Ni Mu, Rowen Jin, Zachary Kozick, Christopher Upjohn, Christopher Grabski, Allison Wong, and Helen Kearns. Your company and support have been invaluable and irreplaceable. Thank you for making meals for me while I worked late nights in lab, always saving the most affordable room in our shared homes for me, including me in your adventures and showing me that the time I dedicated to research could be balanced with a rich experience of life. Ni, I further dedicate this thesis in your memory.

My work would not have been possible without the direction and support of my thesis advisor, Peter Walter. I am grateful to Peter for offering me a position in his lab to explore the effects of his exciting, newly discovered drug. Peter trained me to become a detail-oriented scientist, and a big picture thinker. For the knowledge he imparted, his inspiring scientific insights, and the depth of his generosity, I am profoundly grateful.

I can attribute much of the day-to-day science I learned in Peter's lab to my colleague and mentor, Jordan Tsai. My approach to science is predicated on Jordan's example. Thank you for your mentorship and friendship.

Thank you to all the members of the Walter lab for creating a supportive environment and for the times we shared through the years. I am especially grateful to the members of Team ISRIB, Morgane, Michael and Rosalie, for their scientific input, conversations and friendship. Additionally, none of our work in the lab would have been possible without the support of Christine Genero, Silke Nock, Francesca Sanchez and Marivic Dinglasan. Thank you for keeping our lab running smoothly and ensuring that I had a successful PhD.

Thank you to Adam Frost and Adam Renslo, and members of the Frost and Renslo labs for your mentorship and collaboration. I am profoundly grateful to Adam Frost for being my unofficial co-mentor and always finding time to discuss science with me. I will never forget our Friday morning meetings and how exciting it was during the months leading up to our papers when it seemed like we were making discoveries on a weekly basis. Thank you also to my collaborators Lakshmi Miller-Vedam, Lillian Kenner, Henry Nguyen and Priyadarshini Jaishankar for your contributions, mentorship and support on our shared projects. None of our projects would have come together without your efforts.

Finally, I would like to thank the TETRAD graduate program at UCSF and the MCB graduate program at the University of Washington for funding and support during my early years as a graduate student. The following people deserve special mention: Geeta Narlikar and Jonathan Weissman who served on my thesis committee; Ron Vale and Carol Gross who served on my qualifying exam committee; and David Morgan who served as program director and advisor during my early years as a student. My graduate class has been my rock through the

years and I could not have achieved my goals without each of you. Thank you to each of you for providing me with a memorable graduate school experience that I will always cherish.

MECHANISM OF A MEMORY-ENHANCING INHIBITOR OF THE INTEGRATED STRESS RESPONSE

ADITYA ANAND

ABSTRACT

Cells maintain their proteins in a functional and balanced state by regulating protein synthesis, folding, trafficking and degradation. A central regulatory target in this process is the nucleotide exchange factor eIF2B. Under favorable conditions eIF2B acts as a biological catalyst, efficiently unloading GDP from translation initiation factor 2 (eIF2), a GTPase that is required for protein synthesis. Under conditions of stress such as viral infection or starvation, a conserved signaling pathway known as the integrated stress response (ISR) couples stress detection to the phosphorylation of eIF2. This phosphorylation event renders eIF2 a potent inhibitor of eIF2B to restrict protein synthesis. Relieved of a heavy translational burden, cells are afforded more time and resources to cope with stress.

Recently, a small molecule called ISRIB (integrated stress response inhibitor) was found to activate eIF2B. When systemically administered to mice, ISRIB enhances cognition, confers neuroprotection, and reduces inflammation. These cytoprotective effects highlight the importance of eIF2B in human health and the potential that this pathway offers for therapeutic intervention. To better understand eIF2B-mediated translational control and the physiological effects of ISRIB, we solved a 2.8Å cryo-EM structure of ISRIB-bound human eIF2B. The structure identified ISRIB's binding site at the symmetric core of the eIF2B heterodecamer.

Structural and biochemical analyses revealed that the fully active eIF2B heterodecamer depends on the assembly of two identical tetrameric subcomplexes, and that ISRIB promotes this step by cross-bridging the symmetry interface.

Additional cryoEM structures of eIF2 bound to eIF2B in the dephosphorylated state revealed the eIF2B decamer to be a static platform upon which one or two flexible eIF2 trimers bind and align with eIF2B's bipartite catalytic centers to catalyze guanine nucleotide exchange. Phosphorylation refolds eIF2 alpha, allowing it to contact eIF2B at a different interface that is only present in the full decamer, and thereby sequesters eIF2B into a non-productive complex. Thus, regulation of eIF2B assembly emerges as a rheostat for eIF2B activity that tunes translation during the ISR and that can be further modulated by ISRIB.

TABLE OF CONTENTS

LIST OF FIGURES

CHAPTER 1

CHAPTER 2

LIST OF TABLES

CHAPTER 1

CHAPTER 2

APPENDIX A

Chapter 1

Structure of the nucleotide exchange factor eIF2B reveals mechanism of memory-enhancing molecule

Structure of the nucleotide exchange factor eIF2B reveals mechanism of memory-enhancing molecule

Jordan C. Tsai[1,2,†], Lakshmi E. Miller-Vedam[2,4,†], Aditya A. Anand[1,2,†], Priyadarshini Jaishankar[3], Henry C. Nguyen[2,4], Adam R. Renslo[3], Adam Frost[2,4,*], Peter Walter[1,2,*]

[1] Howard Hughes Medical Institute, University of California at San Francisco

[2] Department of Biochemistry and Biophysics, University of California at San Francisco

[3] Department of Pharmaceutical Chemistry, and Small Molecule Discovery Center, University of California at San Francisco

[4] Chan Zuckerberg Biohub, San Francisco, CA, USA

†The first three authors contributed equally to this work

This work was first submitted to bioRxiv as a preprint at doi.org/10.1101/222257

ABSTRACT

Regulation by the integrated stress response (ISR) converges on the phosphorylation of translation initiation factor eIF2 in response to a variety of stresses. Phosphorylation converts eIF2 from substrate to competitive inhibitor of its dedicated guanine nucleotide exchange factor, eIF2B, inhibiting translation. ISRIB, a drug-like eIF2B activator, reverses the effects of eIF2 phosphorylation, and enhances cognition and corrects cognitive deficits after brain injury in rodents. To determine its mechanism of action, we solved an atomic-resolution structure of ISRIB bound in a deep cleft within decameric human eIF2B by electron cryo-microscopy. Formation of fully active, decameric eIF2B holoenzyme depended on the assembly of two identical tetrameric subcomplexes, and ISRIB promoted this step by cross-bridging a central symmetry interface. Thus, regulation of eIF2B assembly emerges as a rheostat for eIF2B activity that tunes translation during the ISR and that can be further modulated by ISRIB.

INTRODUCTION

Protein quality control is essential to the maintenance of cellular and organismal health. To prevent the production of deleterious proteins, such as those from invading viruses or those produced in misfolding-prone environments, cells regulate protein synthesis. By arresting or accelerating the cardinal decision of translation initiation, cells effect proteome-wide changes that drive organismal functions, such as development, memory, and immunity (*1*-*3*).

A key enzyme in the regulation of protein synthesis is eukaryotic translation initiation factor 2B (eIF2B), a dedicated guanine nucleotide exchange factor (GEF) for translation initiation factor 2 (eIF2). eIF2B is composed of five subunits (α,β,γ,δ,ε) that assemble into a decamer composed of two copies of each subunit (*4*-*8*). The eIF2Bε subunit contains the enzyme's catalytic center and associates closely with eIF2Bγ (*9*). Two copies each of the structurally homologous eIF2Bα, β, and δ subunits form the regulatory core that modulates eIF2B's catalytic activity (*10*-*12*). eIF2B's substrate, eIF2 is composed of three subunits (α,β,γ) and binds methionine initiator tRNA and GTP to form the ternary complex required to initiate translation on AUG start codons. eIF2's γ subunit contains the GTP-binding pocket (as reviewed in (*13*, *14*)).

In response to various inputs, many of which are cell stresses, phosphorylation of eIF2α at serine 51 converts eIF2 from a substrate for nucleotide exchange to a competitive inhibitor of eIF2B. Phosphorylated eIF2 binds to eIF2B with enhanced affinity, effectively sequestering the limiting eIF2B complex from engaging unphosphorylated eIF2 for nucleotide exchange (*10*-*12*). Such inhibition leads to an attenuation of general translation and, paradoxically, the selective translation of stress-responsive mRNAs that contain small upstream open reading frames. This latter set includes mRNAs that encode transcriptional activators such as ATF4 (*15*, *16*). In this way eIF2 phosphorylation elicits an intricate gene expression program. This pathway was termed

the "integrated stress response", following the discovery of several kinases that all phosphorylate eIF2α at serine 51 to integrate different physiological signals such as the accumulation of misfolded proteins in the lumen of the endoplasmic reticulum, the accumulation of double-stranded RNA indicative of viral infection, the cell's redox status, and nutrient availability (*17*). We previously identified an ISR inhibitor (ISRIB) that reverses the effects of eIF2α phosphorylation, restoring translation in stressed cells and blocking translation of ISR-activated mRNAs, such as ATF4 (*18*, *19*). When administered systemically to wild-type rodents, ISRIB enhances cognition, leading to significant improvements in spatial and fear-associated learning (*18*). This effect relies on translation-dependent remodeling of neuronal synapses (*20*). eIF2 phosphorylation correlates with diverse neurodegenerative diseases and cancers, as well as normal aging (*21-24*). In addition, a number of mutations that impair eIF2B activity lead to a neurodegenerative disorder of childhood known as vanishing white matter disease (VWMD) that is marked by cerebellar ataxia, spasticity, hypersensitivity to head trauma and infection, coma and premature death (*25*). As a well-characterized small molecule with rapid cross-blood-brain barrier equilibration, reasonable bioavailability, and good tolerability in rodent efficacy models, ISRIB and related analogs offer great potential for treating VWMD and a range of other devastating diseases lacking therapeutic options (*18*, *26*). Indeed in rodents, ISRIB entirely reverses cognitive deficits associated with traumatic brain injuries (*27*) and protects against neurodegeneration (*26*).

Previous work identified eIF2B as the molecular target of ISRIB (*28*, *29*). ISRIB enhances eIF2B GEF activity three-fold, stabilizes a decameric form of the enzyme when analyzed in high salt conditions, and increases thermostability of eIF2Bδ (*28*). Mutations that render cells insensitive to ISRIB cluster in the N-terminal region of the eIF2Bδ subunit (*29*), and when projected onto

the crystal structure of *S. pombe* eIF2B, two of the mutated residues map to its symmetric interface (*8*). These data hinted that ISRIB may activate eIF2B by binding near adjacent δ subunits to exert its blunting effects on the ISR. Here we report mechanistic and structural insights into ISRIB's mechanism of action.

RESULTS

ISRIB stabilizes decameric eIF2B, accelerating GEF activity

To investigate the mechanism by which ISRIB enhances the GEF activity of eIF2B, we engineered a recombinant *E. coli* expression system for co-expression of all five subunits of human eIF2B (Figure 1.1A). eIF2B purified as a monodisperse complex that sedimented at 13.6S, corresponding to the size of a decamer containing two copies of each subunit (Figure 1.1B - AUC, Figure 1.S1A).

We adapted a fluorescent GDP exchange assay (*29*), to assess the enzymatic activity of recombinant eIF2B. We purified the substrate, non-phosphorylated human eIF2, from a *S. cerevisiae* expression system genetically edited to lack the only yeast eIF2 kinase (*gcn2Δ*) (*30*) (Figure 1.S2A, 1.S2B). First, in a "GDP loading assay" we added fluorescent Bodipy-GDP to GDP-bound eIF2. We observed an eIF2B concentration-dependent increase in fluorescence corresponding to the dislodging of bound GDP and subsequent binding of Bodipy-GDP to eIF2 (Figure 1.S2C, Figure 1.S2D). Second, in a "GDP unloading assay", we chased with a 1000-fold excess of unlabeled GDP and measured a decrease in fluorescence corresponding to the eIF2B-catalyzed dissociation of Bodipy-GDP from eIF2 (Figure 1.S2E). GEF activities were fit to a single-exponential (Figure 1.S2F) for calculating the reported k_{obs} values. Titrating substrate concentration to saturating levels in GDP unloading assays yielded K_m and k_{cat} values similar to those of eIF2B previously purified from mammalian cells (Figure 1.1C) (*31*).

To investigate how ISRIB activates eIF2B, we fixed eIF2B and eIF2 in a multi-turnover regime at concentrations of 10 nM and 1 μM, respectively. Under these conditions, the eIF2 is subsaturating given its K_m of 1.5 μM (Figure 1.1C). Previously, a three-fold stimulation of nucleotide exchange by ISRIB was seen under similar conditions (*28*). Surprisingly, ISRIB only

marginally activated the recombinant eIF2B decamer by 1.2-fold (Figure 1.1D, (- ISRIB): k_{obs} = 0.17 +/- 0.006 min^{-1} and (+ ISRIB): k_{obs} = 0.21 +/- 0.005 min^{-1}).

ISRIB stabilizes eIF2B decamers in lysates of HEK293T cells (*28*), suggesting a role during assembly of the active complex. To test this notion and its implications for ISRIB's mechanism of action, we purified eIF2B in the presence or absence of ISRIB. Under both conditions we obtained the fully assembled decamer (Figure 1.1E, peak 3); however, in the absence of ISRIB we also obtained a partially assembled complex lacking the α subunit that eluted from the anion exchange column at a lower ionic strength (Figure 1.1E, peak 2). These data suggest that ISRIB enhances the stability of the decamer. To test this idea, we expressed eIF2B(βγδε) and eIF2Bα separately (Figure 1.S1B, Figure 1.S1C). Surprisingly, eIF2B(βγδε) purified as a heterotetramer, as determined by analytical ultracentrifugation (Figure 1.S1D), while eIF2Bα purified as a homodimer, as previously observed (Figure 1.S1E) (*6*). We then combined eIF2B(βγδε) and eIF2B(α_2) under stringent conditions of elevated ionic strength (400 mM) to assess ISRIB's contribution to the stability of the decameric complex. When analyzed by velocity sedimentation in the absence of ISRIB, eIF2B(βγδε) sedimented as a tetramer (peak fractions 6-7), whereas eIF2B(α_2) peaked in fraction 4 (Figure 1.1F, upper panel). By contrast, in the presence of ISRIB, eIF2B(βγδε) and eIF2B(α_2) sedimented together as a higher molecular weight complex deeper in the gradient (peak fractions 7-9) (Figure 1.1F, lower panel). As we discuss below, the stabilized decamer peaked in fraction 10 of the gradient, indicating that under these conditions, the decamer partially dissociates during sedimentation. We surmise that dissociation during centrifugation led to the broad sedimentation profiles observed. Thus, ISRIB enhanced the stability of decameric eIF2B.

To understand the interplay between ISRIB binding, eIF2B(α_2) incorporation into the decamer, and GEF activity, we mixed independently purified eIF2B(α_2) and eIF2B($\beta\gamma\delta\varepsilon$) subcomplexes and assayed the combination for GDP unloading. When assayed under these conditions, the specific activity was four-fold reduced when compared to the fully assembled decamer (compare Figure 1.1D and 1G, k_{obs} = 0.17 +/- 0.006 min^{-1} and 0.04 +/- 0.009 min^{-1}). Importantly, the addition of ISRIB restored GEF activity three-fold toward the level of fully assembled decamer (k_{obs} = 0.11 +/- 0.002 min^{-1}) (Figure 1.1G), suggesting that ISRIB's activity reflects enhanced decamer stability.

Using the GDP loading assay, we found that eIF2B activity was reduced profoundly (k_{obs} = 0.01 +/- 0.007 min^{-1}) in the absence of eIF2B(α_2) (Figure 1.1H), as previously reported (*32*, *33*). Interestingly, ISRIB still activated eIF2B($\beta\gamma\delta\varepsilon$) (Figure 1.1I, k_{obs} = 0.04 +/- 0.003 min^{-1}), indicating that ISRIB can enhance GEF activity independent of eIF2B(α_2) incorporation into the holoenzyme. To reconcile these unexpected findings, we next sought a structural understanding of the ISRIB-stabilized human eIF2B decameric complex.

ISRIB binds in a deep cleft, bridging the two-fold symmetric interface of the eIF2B decamer

We determined an atomic resolution structure of eIF2B bound to ISRIB by electron cryo-microscopy (cryoEM). We classified and refined a single consensus structure from 202,125 particles to an average resolution of 2.8 Å resolution, that varied from 2.7 Å in the stable core to >3.4 Å in the more flexible periphery (Figure 1.S3). The overall structure bears clear resemblance to the *S. pombe* two-fold symmetric decameric structure determined by X-ray crystallography (*8*). The symmetry interface comprises contacts between the α, β, and δ subunits,

while the γ and ε subunits are attached at opposing ends (Figure 1.2A-C). As in the *S. pombe* crystal structure, the catalytic HEAT domains of the ε subunits were not resolved, indicating their flexible attachment to the regulatory core. By contrast, densities for the "ear" domains of the γ subunits were resolved, but at a resolution that precluded atomic interpretation (Figure 1.2B, Figure 1.S3-4).

Importantly, we observed a clearly defined density consistent with the dimensions of ISRIB and not attributable to protein bridging the symmetry interface of the decamer (Figure 1.2B, Figure 1.2D-E, Figure 1.S5). Modeling suggests that ISRIB binds with its central cyclohexane ring in the expected low-energy chair conformation and with the side chains projecting to the same face of the cyclohexane ring and inserting the distal 4-chlorophenyl rings into deep binding pockets (Figure 1.2D-F, Figure 1.S5). ISRIB's "U-shaped" conformation may be stabilized by intramolecular N-H---O hydrogen bonding interactions between its amide nitrogen N-H bond and the aryl ether oxygens, possibly explaining why non-ether-linked congeners of ISRIB are much less potent (Figure 1.S6) (*28*, *34*). The cryoEM density most likely corresponds with an average of at least two energetically equivalent ISRIB conformations related by 180° rotations about both N-C bonds to the cyclohexane ring (both depicted in Figure 1.2F and Figure 1.S4-5). This superposition of two conformers accounts for the apparently symmetric density observed, even though in isolation each individual conformer is pseudo-symmetric (Figure 1.S5). The multiple observed ISRIB binding modes may contribute to its free energy of binding by providing additional entropic wiggle room.

The N-terminal loop of the δ subunit contributes key residues to the binding pocket, and this loop differs significantly from the ligand-free *S. pombe* structure (*8*). Residues in this loop are important for ISRIB activity (*29*), including δV177 and δL179, which contribute directly to the

hydrophobic surface of the binding pocket (Figure 1.2F, Figure 1.S6). In addition, the δ subunits contribute δL485 to the hydrophobic wells that accommodate the halogenated benzene rings (Figure 1.2F, Figure 1.S6). The center of the binding site comprises residues from the β subunit, including βN162 and βH188, which lie near ISRIB's more polar functionality. In particular, one of the two C-H bonds at the glycolamide α-carbon is oriented perpendicular to the plane of the aromatic histidine ring (Figure 1.2F, Figure 1.S6), suggesting a C-H-π interaction with βH188. Residues on the β subunits also make key contributions to the hydrophobicity of the deep wells, including βV164 and βI190.

Thus, ISRIB enhances incorporation of the α subunit into the decamer despite not making direct contacts with this subunit. Rather, ISRIB stabilizes the symmetry interface of the β-δ core, which in turn favors stable eIF2B(α_2) binding. As such, ISRIB's enhancement of GEF activity derives from its ability to promote higher-order holoenzyme assembly.

Structural model predicts the activity of modified compounds and mutations

To validate the structural model, we synthesized ISRIB analogs bearing a methyl group at the α position of the glycolamide side chains. Two enantiomers, ISRIB-A19(*R,R*) and ISRIB-A19(*S,S*) were prepared (Figure 1.S7A) based on predicted steric clashes with residue δL179 for ISRIB-A19*(R,R)* or βH188 for ISRIB-A19*(S,S)* in the ISRIB binding pocket (Figure 1.2F, Fig S6). As expected, neither enantiomer enhanced GEF activity in vitro or in cells (Figure 1.3A, Figure 1.S7B), nor did they enhance the stability of purified decameric eIF2B (Figure 1.S7C). We next engineered eIF2B to accommodate the additional methyl groups on ISRIB-A19*(R,R)* by mutating δL179 to alanine. We tested the effects of both compounds on eIF2B(δL179A) by velocity sedimentation and GEF activity. As predicted, ISRIB-A19*(R,R)* stabilized formation of mutant

decamers (Figure 1.3B) and stimulated nucleotide exchange (Figure 1.3C). Treatment with ISRIB-A19*(R,R)* activated eIF2B(δL179A) approximately three-fold (Figure 1.3C, k_{obs} = 0.027 +/- 0.001 min^{-1}), a similar fold-activation to eIF2B WT by ISRIB. By contrast and as predicted, ISRIB-A19*(S,S)* failed to activate eIF2B(δL179A) (Figure 1.3C, k_{obs} = 0.007 +/- 0.001 min^{-1}). Notably, in the absence of ISRIB analogs, eIF2B(δL179A) was five-fold less active than eIF2B (compare Figure 1.3A and 3C, eIF2B k_{obs} = 0.04 +/- 0.009 min^{-1} and eIF2B(δL179A) k_{obs} = 0.008 +/- 0.002 min^{-1}), identifying δL179A as a novel hypomorphic mutation and underscoring the importance of this surface for holoenzyme assembly.

We next sought to verify the existence of a putative C-H-π interaction between βH188 and ISRIB by mutating βH188 to alanine. As predicted, ISRIB did not stabilize eIF2B(βH188A) decamers (Figure 1.3D-E, Figure 1.S8). By contrast, mutating βH188 to an aromatic tyrosine or phenylalanine—which are predicted to sustain and likely enhance C-H-π interactions—did not impair ISRIB's activity to stabilize decamers (Figure 1.3D, Figure 1.3F-G, Figure 1.S8). Rather, ISRIB stabilized eIF2B(βH188Y) and eIF2B(βH188F) decamers to an even greater extent than wild-type eIF2B decamers (Figure 1.3D). Whereas ISRIB-stabilized wild-type eIF2B sedimented with a broad profile, indicating dissociation of the decamer through the course of sedimentation (Figure 1.1F, Figure 1.3D), ISRIB-stabilized eIF2B(βH188Y) and eIF2B(βH188F) formed a sharp symmetric peak in fraction 10, indicative of enhanced complex integrity through sedimentation, presumably owing to enhanced C-H-π bonding interaction with ISRIB (Figure 1.3D, Figure 1.3F-G, Figure 1.S8).

ISRIB induces dimerization of tetrameric eIF2B subcomplexes

Because ISRIB bridges the symmetry interface of the decamer without making direct contacts with eIF2B(α_2), we sought to understand how the small molecule promotes eIF2B(α_2) incorporation into the decamer. We imaged purified eIF2B(βγδε) tetramers in the presence and absence of ISRIB by cryoEM. In the presence of ISRIB, the images revealed a predominant species consistent with an octameric complex of eIF2B lacking the α subunits (Figure 1.4A). By contrast, in the absence of ISRIB, the predominant species was consistent with a tetrameric complex divided along the symmetry axis of the octamer (Figure 1.4B). In accordance with the ISRIB-dependent stabilization of the decamer by mutations in βH188 to other aromatic residues, βH188F and βH188Y mutants also stabilized the octamer in high salt conditions (Figure 1.S9). These images suggest a model in which ISRIB dimerizes eIF2B(βγδε) by "stapling" the tetramers together to form the octameric binding platform for α subunit binding, consistent with the architecture of the ISRIB-bound decamer.

We next substantiated eIF2B(βγδε) dimerization by analytical ultracentrifugation under physiological salt conditions. In the absence of ISRIB, eIF2B(βγδε) sedimented as a predominant 8.0S peak and a minor 11.7S peak, corresponding to eIF2B(βγδε) and eIF2B$(\beta\gamma\delta\varepsilon)_2$, respectively (Figure 1.4C). By contrast, in the presence of ISRIB, we observed a dramatic increase in the 11.7S peak, demonstrating ISRIB's role in stabilizing the eIF2B$(\beta\gamma\delta\varepsilon)_2$ octamer. Together with the observation that eIF2B(βγδε) has greater activity in the presence of ISRIB (Figure 1.1I), these data show the importance of octamer assembly in activating GEF activity.

Dimerization of eIF2B(βγδε) effectively doubles the surface area for eIF2B(α_2) binding, suggesting that the ISRIB-enhanced incorporation of eIF2B(α_2) into the decamer originates from ISRIB's ability to shift the tetramer/octamer equilibrium. To test this prediction, we combined

eIF2B(α_2) and eIF2B($\beta\gamma\delta\varepsilon$) in the presence and absence of ISRIB and assessed decamer assembly by analytical ultracentrifugation. Under the high protein concentrations used in these assays, we observed a predominant peak corresponding to the assembled eIF2B decamer at 13.6S both in the presence and absence of ISRIB, together with minor peaks corresponding to unincorporated eIF2B($\beta\gamma\delta\varepsilon$) at 8.0S and eIF2B($\alpha_2$) at 4.1S (Figure 1.4D). Importantly, we did not observe an octamer peak, suggesting the octamer has a high affinity for eIF2B(α_2) and assembles the full decamer under these conditions. Together with the cryoEM images, these data demonstrate that eIF2B(α_2) and ISRIB synergistically promote dimerization of eIF2B($\beta\gamma\delta\varepsilon$). Given that ISRIB binds across the eIF2B$(\beta\gamma\delta\varepsilon)_2$ interface such that each tetramer contributes half of the ISRIB binding site, we reasoned that high ISRIB concentrations may occupy half-sites within the tetramers and interfere with octamer formation. Indeed, ISRIB promoted eIF2B$(\beta\gamma\delta\varepsilon)_2$ assembly at 1 μM but failed to do so at 10 μM (Figure 1.4E). Similarly, ISRIB stimulated GEF activity of eIF2B($\beta\gamma\delta\varepsilon$) at 200 nM but failed to do so at 5 μM (Figure 1.4F). Importantly, the high ISRIB concentrations used in this assay did not reduce GEF activity below that of eIF2B($\beta\gamma\delta\varepsilon$), demonstrating that the effect did not result from non-specific enzymatic inhibition.

Loss and gain-of-function dimerization mutants resist or bypass the effects of ISRIB

To visualize the determinants of octamerization, we highlighted the solvent-excluded surface area along the symmetry interface of the β and δ subunits in adjacent tetramers (Figure 1.5A-B, light yellow, light blue, green) and labeled the residues of the ISRIB binding pocket on this surface (Figure 1.5A-B, gray). The tetramer-tetramer contact residues form a thin strip along each neighboring β and δ subunit. Most of the β subunit residues contact the δ subunit across the symmetry interface, while a small number of residues also cement β-β' contacts. Of these,

βH160 and βR228 reside at the junction of β-β' and β-δ' subunits, suggesting that they play key roles in stabilizing the octamer. Accordingly, we observed that mutation of βH160 to aspartic acid, which we predicted would be repulsed by δD450, completely precluded octamer assembly. Analytical ultracentrifugation of eIF2B(βγδε) containing the βH160D mutation revealed a sharp tetramer peak at 7S both in the absence and presence of ISRIB (Figure 1.5C), and ISRIB was unable to enhance GEF activity for this mutant (Figure 1.5D). Thus, the effect of this mutation on octamerization cannot be overcome by ISRIB binding, despite the fact that ISRIB binding buries an additional ~11% of solvent-exposed surface area—an increase from 3420 $Å^2$ to 3790 $Å^2$—upon stapling of tetramers (Figure 1.5A-B).

Serendipitously, we also identified a gain-of-function mutation in eIF2B. We initially engineered a δL179V mutation alongside the δL179A mutation used above to accommodate the methylated analog ISRIB-A19(*R,R*) (Figure 1.2F, Figure 1.S6). To our surprise, we discovered that the predominant species of δL179V-eIF2B(βγδε) sedimented as a remarkably stable octamer in the absence of ISRIB (Figure 1.5E). GEF activity assays revealed that δL179V-eIF2B$(\beta\gamma\delta\varepsilon)_2$ was five-fold more active than the wild-type octamers formed in the presence of ISRIB, and was not further activated by ISRIB (compare Figure 1.5F and Figure 1.1I, eIF2B(δL179V) k_{obs} = 0.027 +/- 0.001 min^{-1}, eIF2B(δL179V) + ISRIB k_{obs} = 0.024 +/- 0.001 min^{-1}, WT + ISRIB k_{obs} = 0.005 +/- 0.001 min^{-1}). Together with the ISRIB-bound structure, these mutants indicate that the major contribution of ISRIB to increased GEF activity lies at the step of tetramer dimerization and assembly of the bipartite surface for α subunit homodimer binding (Figure 1.6).

DISCUSSION

We determined the structure of human eIF2B at sufficiently high resolution to characterize the binding-site and coordination of a small molecule with therapeutic potential. In concomitant work, Zyryanova et al. report similar findings (*49*). The atomic model of ISRIB-bound eIF2B reconciles structure-activity-relationships described previously (*28*, *34*), predicted both loss- and gain-of-function mutations, and facilitates the rational design of small molecule modulators of eIF2B activity. The structure provides an intuitive view of how ISRIB activates nucleotide exchange: ISRIB stabilizes the active decameric form of the eIF2B holoenzyme by stapling the constituents together across a 2-fold symmetry axis.

Given that a catalytic residue essential for nucleotide exchange resides in the still unresolved HEAT repeat of the ε subunit, how does assembly of the decameric holoenzyme enhance activity? Crosslinking studies suggest that eIF2 binds across the decameric interface, engaging the eIF2B α subunit, and β and δ subunits from opposing tetramers (*8*). We surmise that decamer assembly creates a composite surface for eIF2 binding that allows the flexibly attached HEAT domain to reach and engage its target. While we consider it likely that the effects of ISRIB binding can be explained by the degree of holoenzyme assembly, additional ligand-induced allosteric changes may also contribute to its activity.

These observations provide a plausible model for ISRIB's ability to ameliorate the inhibitory effects of eIF2α phosphorylation on ternary complex formation. ISRIB staples tetrameric building blocks together into an octamer, which enhances activity three-fold, and forms a platform for association of the dimeric α subunits. The integrated effect of these sequential steps is an order of magnitude enhancement of activity. The inhibition resulting from a limiting amount of phosphorylated eIF2 would be reduced by the surplus of GEF activity provided by

ISRIB. By contrast, an excess of ISRIB poisoned the assembly reaction by saturating half-binding sites on unassembled tetramers. Thus, within its effective concentration range, ISRIB will enhance ternary complex formation even in unstressed conditions, opening an untapped reservoir of additional enzymatic capacity. We surmise that in vivo these activities are likely to be realized near the equilibrium points of the assembly reactions for the holoenzyme, allowing for ISRIB's observed phenotypic effects. Thus, eIF2B is poised to integrate diverse signals that impact translation initiation. Phosphorylation of eIF2 may be just one of many mechanisms for modulating its activity. Post-translational modifications, expression of other modulatory components, or binding of yet-to-be-identified endogenous ligands to the ISRIB binding pocket or elsewhere are likely to modulate eIF2B activity under varying physiological conditions. Understanding the different modes of regulation of this vital translational control point will be of particular importance in the nervous system where ISRIB has been shown to have a range of effects.

Figure 1.1

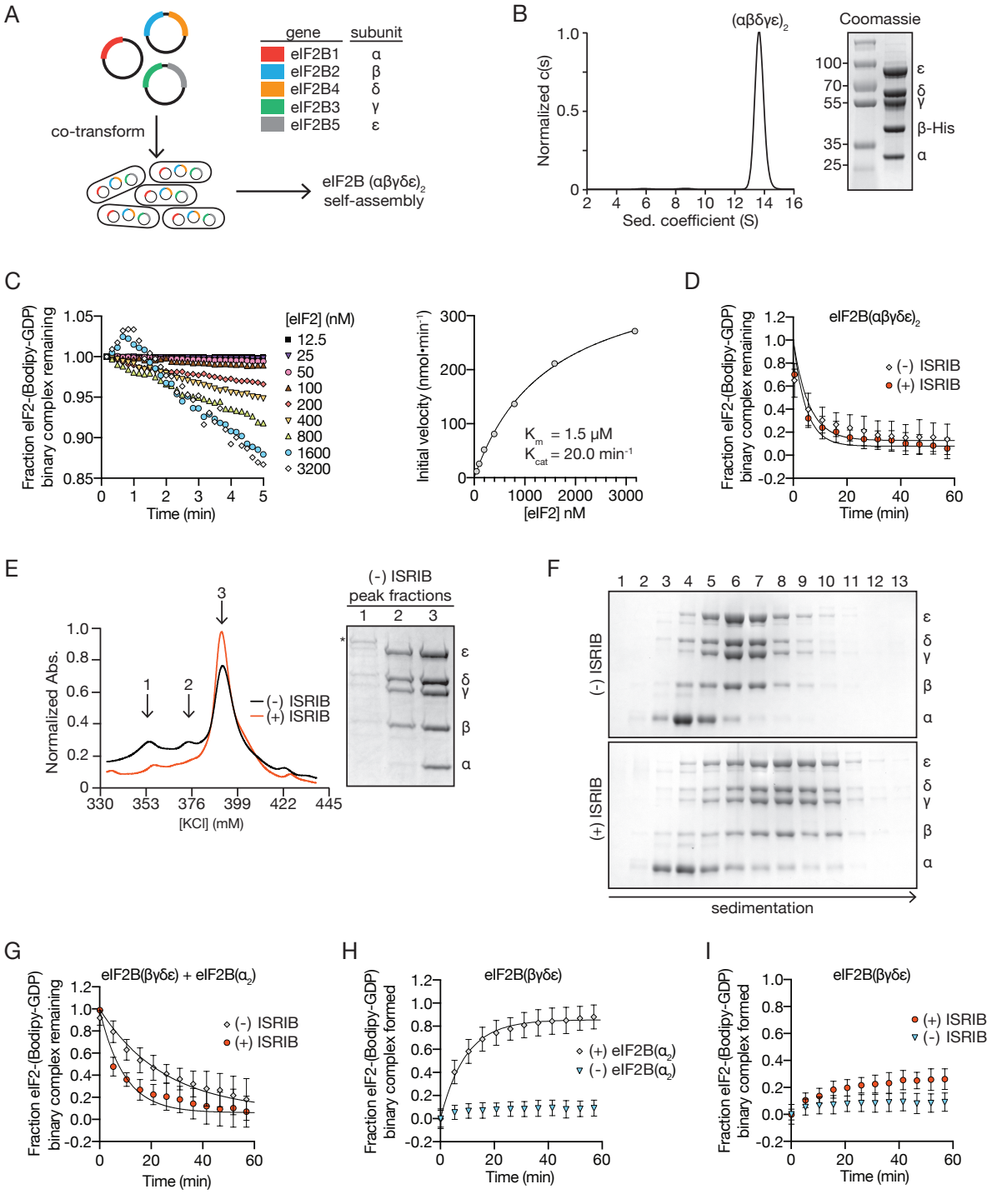
A
co-transform
gene
subunit
eIF2B1
α
eIF2B2
β
eIF2B4
δ
eIF2B3
γ
eIF2B5
ε
eIF2B (αβγδε)2
self-assembly
B
(αβδγε)2
Coomassie
Normalized c(s)
Sed. coefficient (S)
ε
δ
γ
β-His
α
C
Fraction eIF2-(Bodipy-GDP) binary complex remaining
Time (min)
[eIF2] (nM)
12.5
25
50
100
200
400
800
1600
3200
Initial velocity (nmol•min-1)
[eIF2] nM
Km = 1.5 μM
Kcat = 20.0 min-1
D
eIF2B(αβγδε)2
(-) ISRIB
(+) ISRIB
E
(-) ISRIB
peak fractions
Normalized Abs.
[KCl] (mM)
F
(-) ISRIB
(+) ISRIB
sedimentation
G
eIF2B(βγδε) + eIF2B(α2)
H
eIF2B(βγδε)
Fraction eIF2-(Bodipy-GDP) binary complex formed
(+) eIF2B(α2)
(-) eIF2B(α2)
I

Figure 1.1

ISRIB stabilizes decameric eIF2B, accelerating GEF activity. (A) Schematic diagram for three plasmid expression of all five eIF2B genes in *E. coli*. (B) Characterization of eIF2B$(\alpha\beta\gamma\delta\varepsilon)_2$ by sedimentation velocity analytical ultracentrifugation and SDS-PAGE followed by Coomassie blue staining. (C) Initial rate of nucleotide exchange (right panel) plotted as a function of substrate concentration. Note that at high eIF2 concentration we reproducibly observed a transient increase in fluorescence that peaked at the 1 min time point (left panel). Such increase was reported previously (*29*) and remains unexplained. (D) GEF activity of eIF2B$(\alpha\beta\gamma\delta\varepsilon)_2$ as measured by unloading of fluorescent GDP from eIF2 in the presence and absence of ISRIB. (E) Representative absorbance 280 nm traces from an anion exchange column used in the purification of eIF2B in the presence (red) and absence (black) of ISRIB (n=3). Traces were normalized to total protein eluted in respective runs. Peak fractions from the (-) ISRIB purification were analyzed by SDS-PAGE and Coomassie-stained. eIF2B subunits are labeled (α-ε) and an asterisk denotes the presence of a contaminating protein that contributes to peak 1. (F) Stability of eIF2B$(\alpha\beta\gamma\delta\varepsilon)_2$ was assessed by sedimentation velocity on a 5-20% sucrose gradient in a 400 mM salt buffer. eIF2B$(\beta\gamma\delta\varepsilon)$ and eIF2B(α_2) were combined with and without 500 nM ISRIB. Fractions were analyzed by SDS-PAGE and Coomassie-stained. (G) GEF activity of eIF2B assembled from purified eIF2B$(\beta\gamma\delta\varepsilon)$ and eIF2B(α_2) in the presence and absence of ISRIB. (H) GEF activity of eIF2B$(\beta\gamma\delta\varepsilon)$ in the presence and absence of eIF2B(α_2). (I) GEF activity of eIF2B$(\beta\gamma\delta\varepsilon)$ in the presence and absence of ISRIB.

Figure 1.2

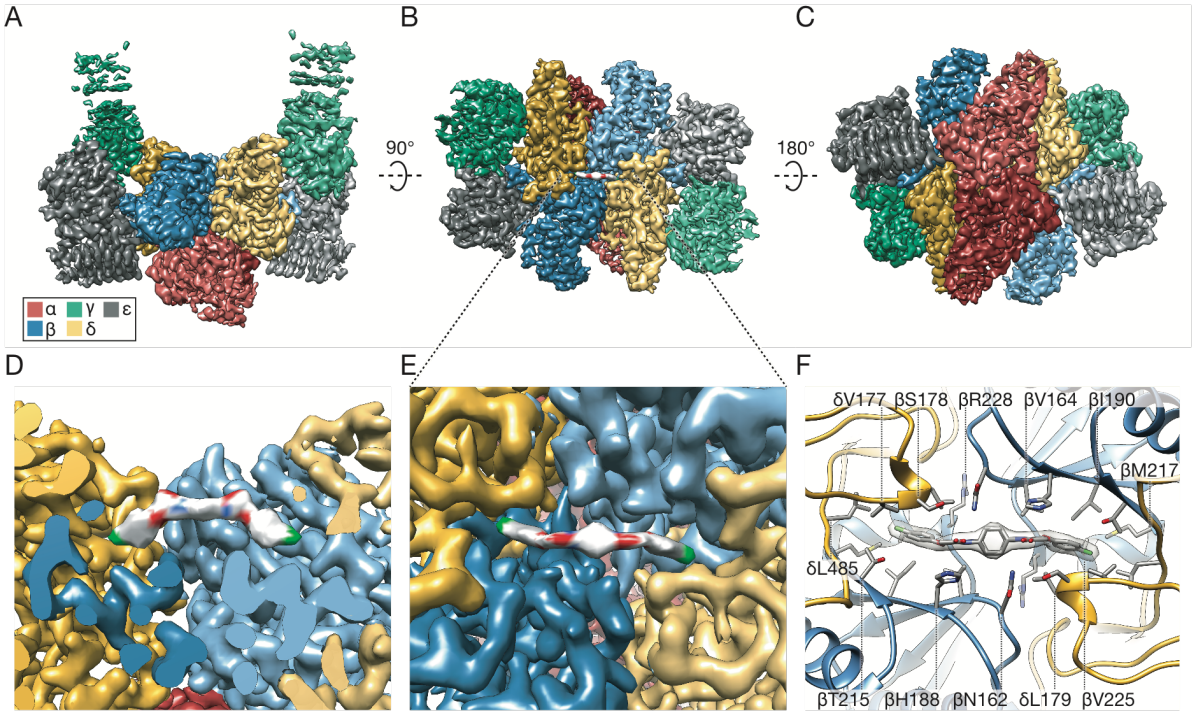

Atomic resolution reconstruction of ISRIB-bound eIF2B. (A-C) Three views of cryoEM density for eIF2B$(\alpha\beta\gamma\delta\varepsilon)_2$, colored in distinct shades for each subunit copy: red for α, blue for β, green for γ, gold for δ, and gray for ε (color code used throughout this manuscript). Density assigned to ISRIB depicted in CPK coloring: oxygens highlighted in red, nitrogens in blue and chlorines in green. The rotational relationships between the views depicted in A, B, and C are indicated. (D) Cross-section of (A), revealing view of the ISRIB binding pocket at the central decamer symmetry interface and density assigned to ISRIB CPK-colored by element. (E) Close-up view of density assigned to ISRIB and its binding pocket in (B) at the intersection of two β and two δ subunits. (F) Two conformers of ISRIB modeled into the density and all residues within a 3.7Å distance from the ligand rendered as sticks.

Figure 1.3

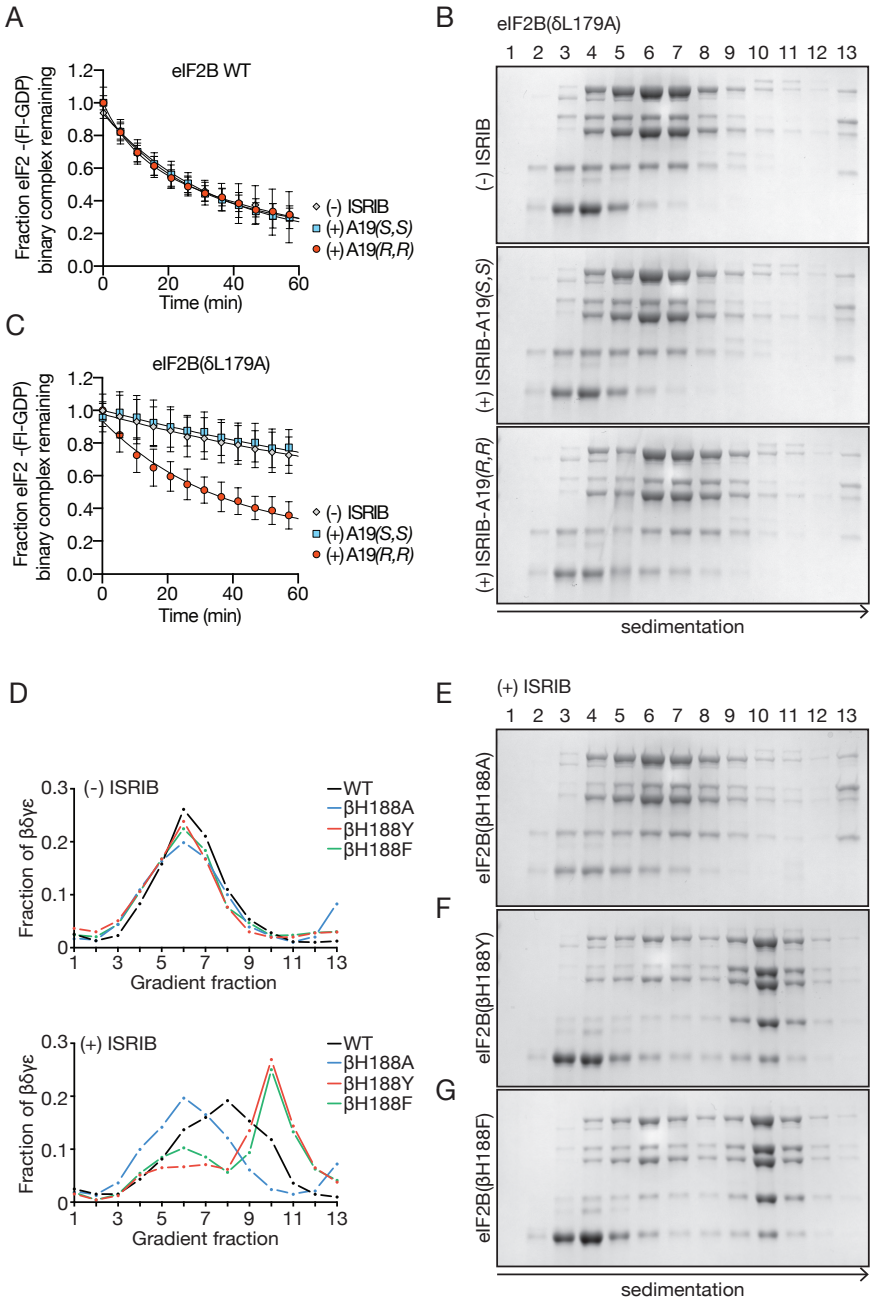
A
eIF2B WT
Fraction eIF2 -(FI-GDP) binary complex remaining
Time (min)
(-) ISRIB
(+) A19(S,S)
(+) A19(R,R)
B
eIF2B(δL179A)
(-) ISRIB
(+) ISRIB-A19(S,S)
(+) ISRIB-A19(R,R)
sedimentation
C
eIF2B(δL179A)
D
(-) ISRIB
(+) ISRIB
Fraction of βδγε
Gradient fraction
WT
βH188A
βH188Y
βH188F
E
(+) ISRIB
eIF2B(βH188A)
F
eIF2B(βH188Y)
G
eIF2B(βH188F)

Figure 1.3

eIF2B structure predicts activity of ISRIB analogs. (A) GEF activity of assembled eIF2B(βγδε) and eIF2B(α_2) in the presence and absence of ISRIB-A19*(R,R)* and ISRIB-A19*(S,S)*. (B) Stability of decameric eIF2B(δL179A) in the absence of ISRIB (top), presence of ISRIB-A19*(S,S)* (middle), or presence of ISRIB-A19*(R,R)* (bottom) as assessed by velocity sedimentation on sucrose gradients. (C) eIF2B GEF activity of assembled eIF2B(βγδε) and eIF2B(α_2) containing a δL179A mutation in the presence and absence of ISRIB-A19*(R,R)* and ISRIB-A19*(S,S)*. (D) Quantification of eIF2B decamer stability gradients plotted as fraction of eIF2B(βγδε) present in each of lanes 1-13. eIF2B (for comparison from data shown in Figure 1.1F), eIF2B(βH188A), eIF2B(βH188Y), eIF2B(βH188F) gradients are plotted in the presence (bottom panel) and absence (top panel) of 500 nM ISRIB. (E, F, G) Stability of decameric eIF2B(βH188A), eIF2B(βH188Y), and eIF2B(βH188F) in the presence of ISRIB as assessed by velocity sedimentation on sucrose gradients.

Figure 1.4

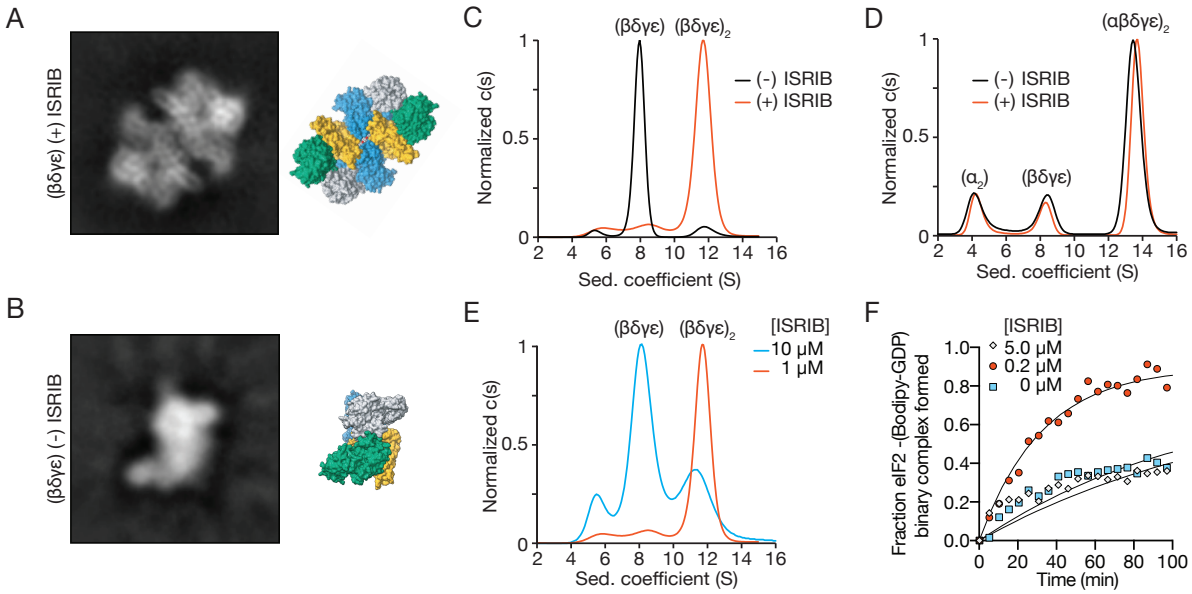

ISRIB induces dimerization of tetrameric eIF2B subcomplexes. The most abundant 2D class averages from cryoEM imaging of eIF2B(βγδε) in the presence (A) and absence (B) of ISRIB. (C) Characterization of eIF2B(βγδε) by sedimentation velocity analytical ultracentrifugation. eIF2B(βγδε) (1 μM) was analyzed in the presence and absence of 1 μM ISRIB. (D) Mixture of 1 μM eIF2B(βγδε) and 500 nM eIF2B(α_2) characterized by analytical ultracentrifugation in the presence and absence of 1 μM ISRIB. (E) eIF2B(βγδε) (1 μM) characterized by analytical ultracentrifugation in the presence of 1 μM or 10 μM ISRIB. (F) GEF activity of eIF2B(βγδε), here at a higher 100nM concentration to facilitate comparison of 0, 0.2, and 5 μM ISRIB.

Figure 1.5

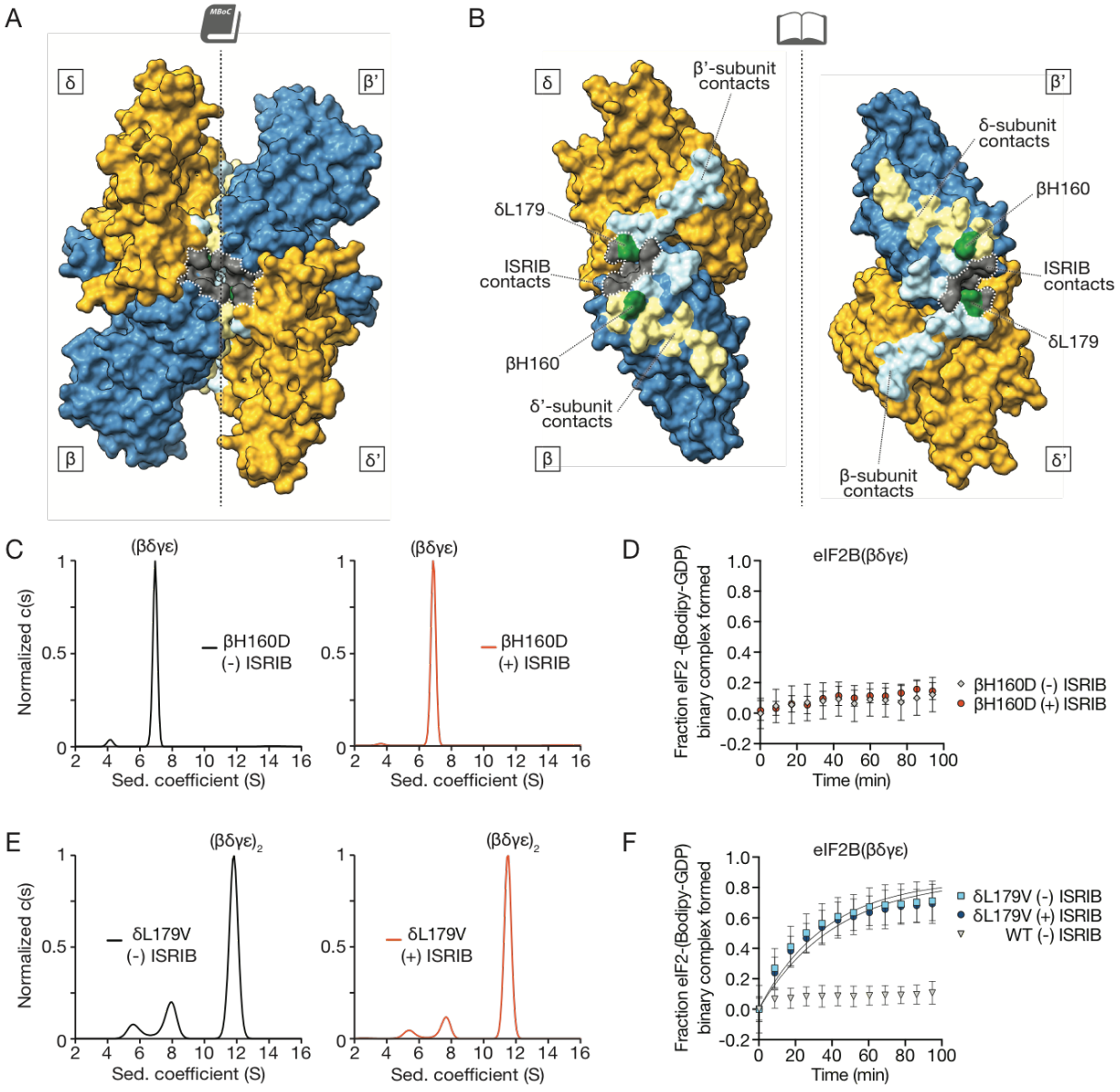
A
δ
β'
β
δ'
B
δ
β'-subunit contacts
δL179
ISRIB contacts
βH160
δ'-subunit contacts
β
β'
δ-subunit contacts
βH160
ISRIB contacts
δL179
β-subunit contacts
δ'
C
(βδγε)
Normalized c(s)
βH160D (-) ISRIB
Sed. coefficient (S)
(βδγε)
βH160D (+) ISRIB
Sed. coefficient (S)
D
eIF2B(βδγε)
Fraction eIF2 -(Bodipy-GDP) binary complex formed
βH160D (-) ISRIB
βH160D (+) ISRIB
Time (min)
E
(βδγε)2
Normalized c(s)
δL179V (-) ISRIB
Sed. coefficient (S)
(βδγε)2
δL179V (+) ISRIB
Sed. coefficient (S)
F
eIF2B(βδγε)
Fraction eIF2-(Bodipy-GDP) binary complex formed
δL179V (-) ISRIB
δL179V (+) ISRIB
WT (-) ISRIB
Time (min)

Figure 1.5

Loss- and gain-of-function dimerization mutants resist or bypass the effects of ISRIB. (A) Surface rendering of core eIF2Bβ (blue) and eIF2Bδ (gold) subunits with residues contacting ISRIB highlighted in gray and with dimer interface indicated by dashed line. Interface residues are highlighted in a lighter hue of the colors of the contacting subunits. (B) Open-book view of the dimer-dimer interface, such that each β and δ subunit is rotated by 90˚. βH160, in green, contacts both β' and δ'; δL179, also in green, contacts both β' and ISRIB. (C) Characterization of 1 μM eIF2B(βγδε) containing a βH160D mutation in the presence (right) and absence (left) of 1 μM ISRIB by analytical ultracentrifugation. (D) GEF activity of eIF2B(βγδε) containing a βH160D mutation in the presence and absence of ISRIB. (E) Characterization of 1 μM eIF2B(βγδε) containing a δL179V mutation in the presence (right) and absence (left) 1 μM ISRIB by analytical ultracentrifugation. (F) GEF activity of eIF2B(βγδε) containing a δL179V mutation in the presence and absence of ISRIB.

Figure 1.6

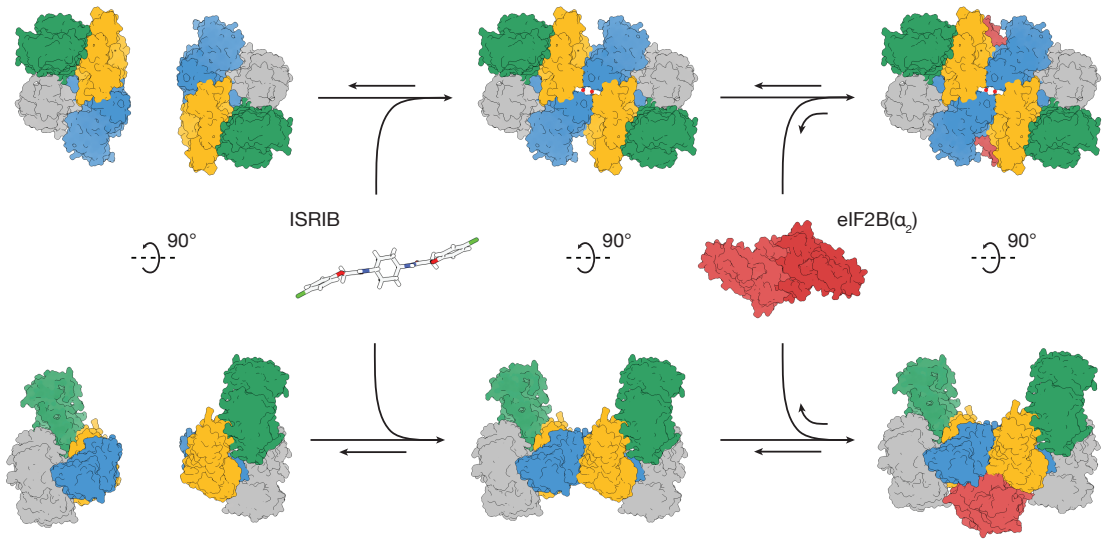

Model for ISRIB's mechanism of action. ISRIB staples together tetrameric eIF2B(βγδε) subcomplexes, building a more active eIF2B(βγδε)$_2$ octamer. In turn, the ISRIB-stabilized octamer binds eIF2B(α_2) with greater affinity, enhancing the formation of a fully-active, decameric holoenzyme.

Figure 1.S1

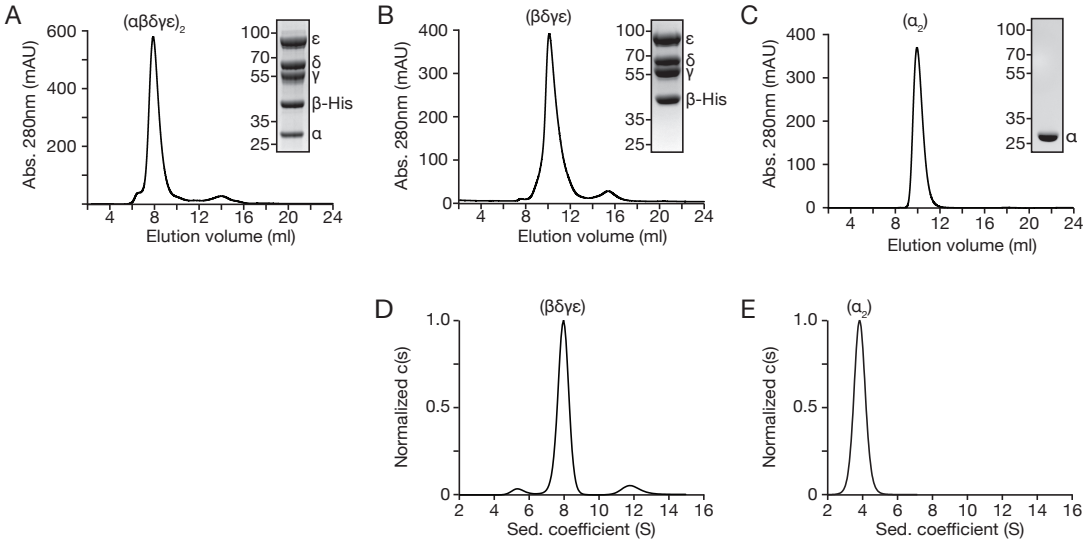

Purification and characterization of decameric eIF2B. Characterization of (A) eIF2B$(\alpha\beta\gamma\delta\varepsilon)_2$, (B) eIF2B$(\beta\gamma\delta\varepsilon)$, and (C) eIF2B$(\alpha_2)$, by size-exclusion chromatography. Peak fractions were concentrated and characterized further by SDS-PAGE followed by Coomassie blue staining. Characterization of (D) eIF2B$(\alpha\beta\gamma\delta\varepsilon)_2$ and (E) eIF2B(α_2) by analytical ultracentrifugation.

Figure 1.S2

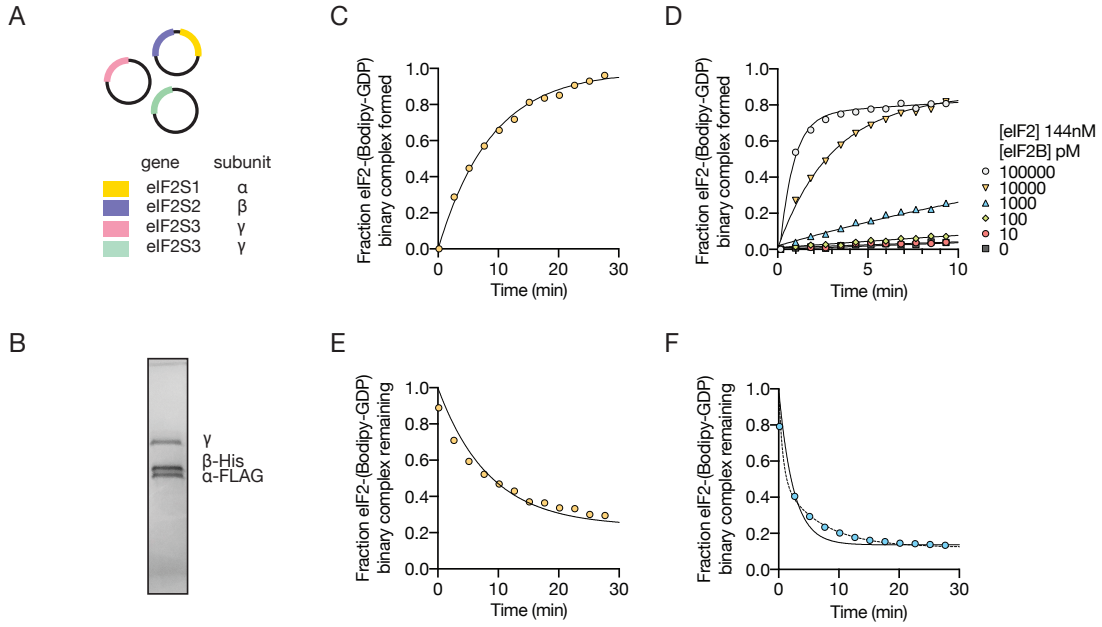

Purification of substrate eIF2 and implementation of GDP exchange assay. (A) Recombinant *S. cerevisiae* expression system for human eIF2 as described in (*30*). Two copies of eIF2γ compensate for low expression of this gene. (B) Characterization of purified eIF2 by SDS-PAGE followed by Coomassie blue staining. (C) Fluorescent GDP loading and subsequent (D) unloading curves in the presence of 10 nM eIF2B. (E) GEF activity varies with eIF2B$(\alpha\beta\gamma\delta\varepsilon)_2$ concentration as measured by loading of fluorescent GDP. (F) Comparison of single-(solid line) and double-exponential (dotted line) fits of ISRIB-mediated GDP unloading. Double-exponential fits correlate better with the data ($R^2 = 0.98$ for double, 0.88 for single) but cannot be explained by current models for nucleotide exchange.

Figure 1.S3

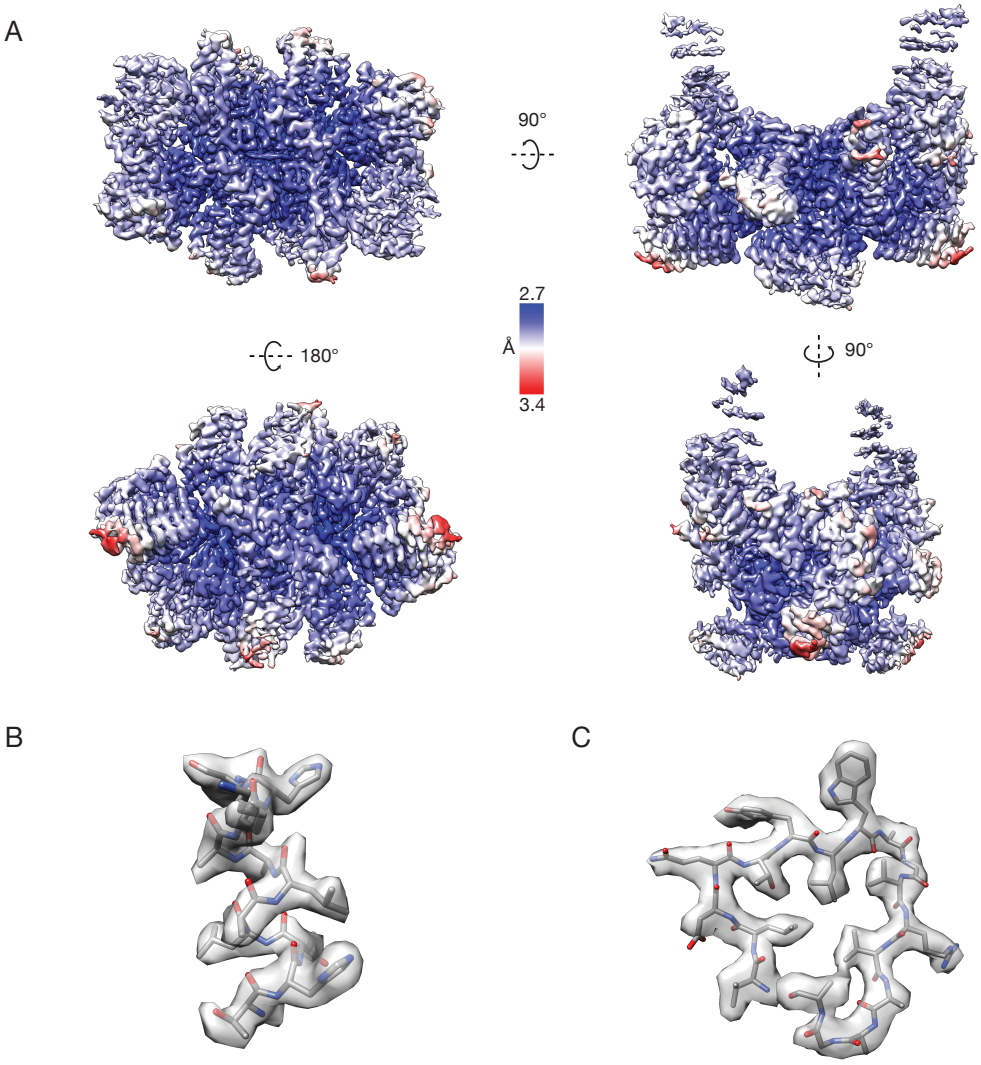

Local resolution. (A) Local resolution estimates determined using RELION 2.1 and displayed using UCSF Chimera. Superlative regions of the cryoEM map rendered as a transparent isosurface and interpreted with atomic coordinates for an (B) alpha-helix and a turn of a (C) beta-solenoid.

Figure 1.S4

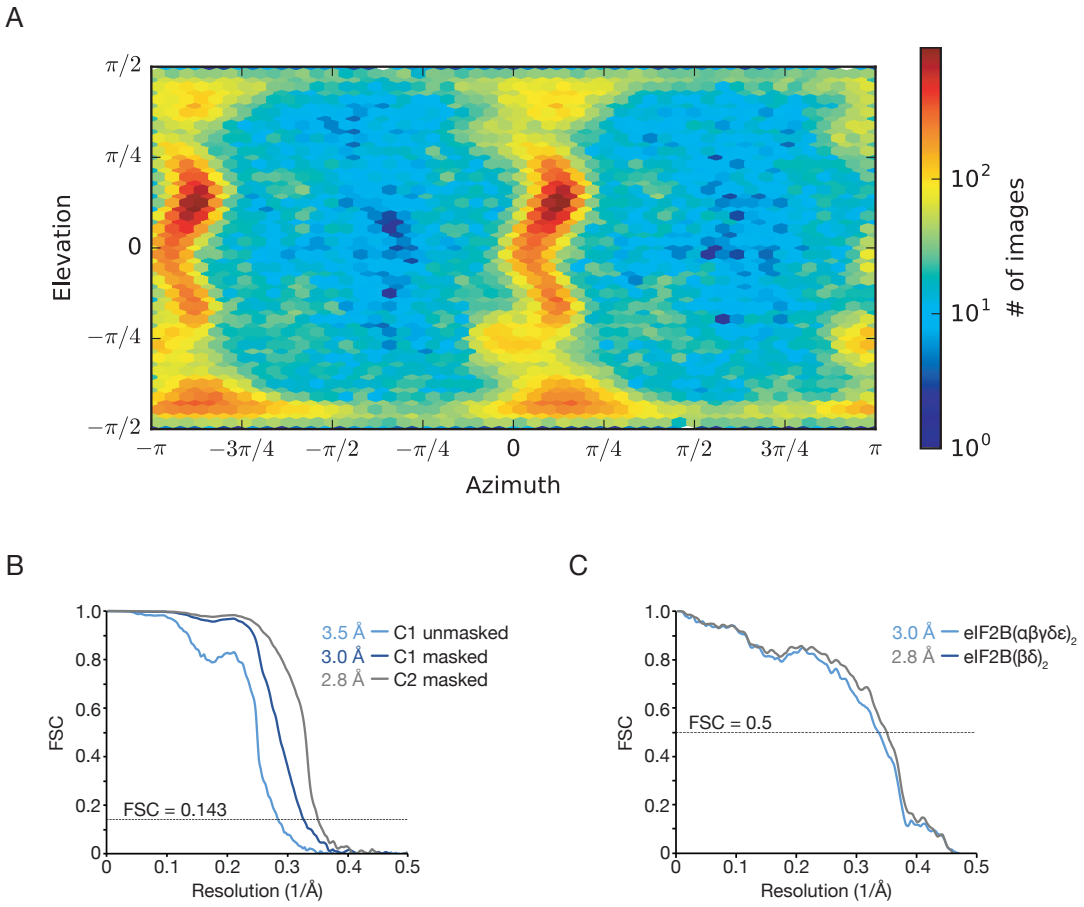

Particle orientation distribution and resolution determination. (A) Plot of per-particle direction distribution over azimuth and elevation angles using CryoSPARC. (B) Fourier shell correlations for independent half maps reconstructed without symmetry or masking, versus without symmetry and with soft masking, and versus with C2 symmetry and soft masking. (C) Fourier shell correlations for the final cryoEM density map versus simulated density maps for the atomic model of the intact decamer versus the ISRIB-stabilized subunits alone.

Figure 1.S5

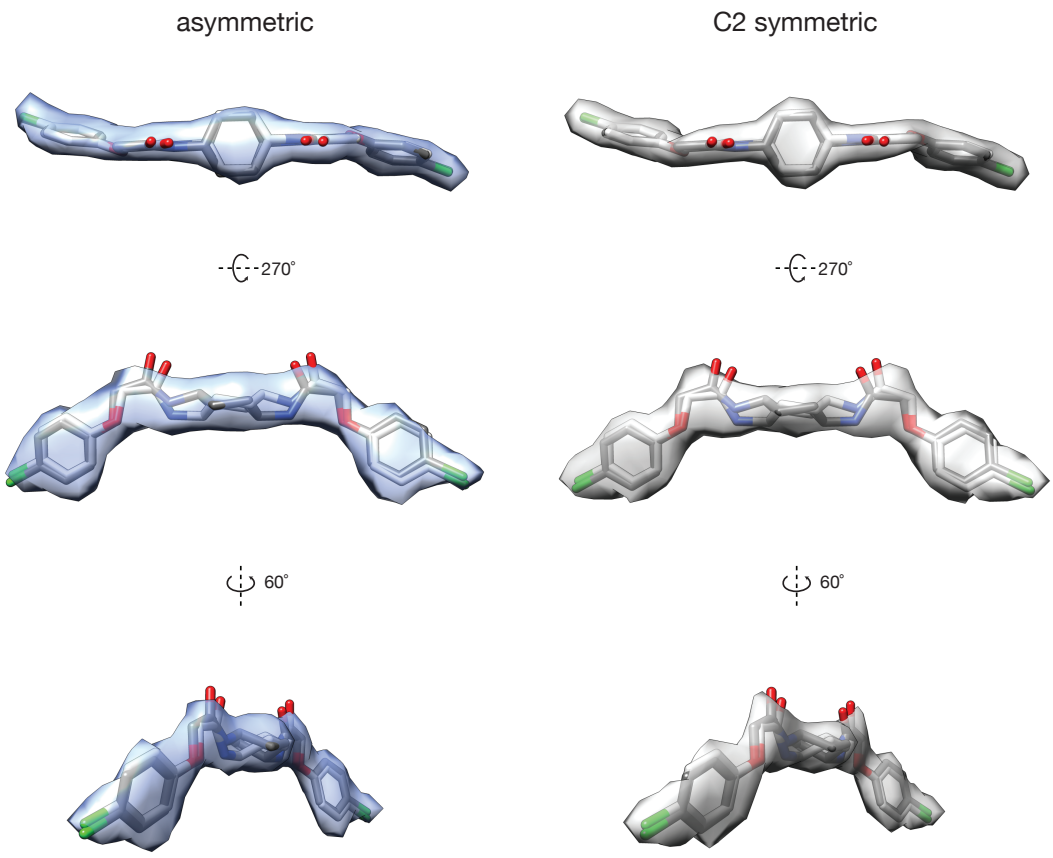

Symmetry and multiple conformer interpretation of the ligand density. Isosurface representations of the cryoEM density computed without symmetry (left, blue) versus with C2 symmetry imposed throughout refinement (right, gray). Although additional conformers of the ligand remain possible given the density, the pair of chair conformers shown are related by rotations of 180° about the N–C bonds to the central cyclohexane ring, or equivalently by rotation of the entire ligand 180° about the axis orthogonal to the plane of the cyclohexane ring. The U-shaped conformation of the O-arylglycolamide side chains is consistent with extensive structure–activity studies of ISRIB analogs (see Figure 1.S6, (*28*, *34*))

Figure 1.S6

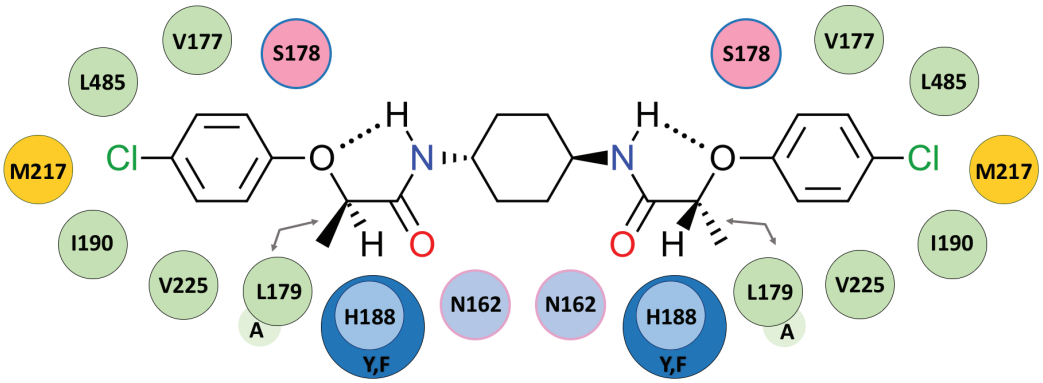

ISRIB binding environment and key mutants. A subset of residues lining the ISRIB binding pocket are rendered as bubbles and color-coded according to amino acid properties. βM217 (yellow) contributes to the hydrophobicity of the pocket and an apparent sulfur-halogen interaction. βI190, βV225, δL485, δV177 and δL179 (green) contribute to the hydrophobicity of deep pockets in the binding site. Mutagenizing δL179 to Ala (smaller, lighter green circle) opened the binding pocket and enabled the methyl-substituted ISRIB-A19(*R,R*) analog to bind (arrows point to the mutated residue and the added methyl group, also see Figures 1.2F and 1.5D). βN162 (blue), δS178 (pink), and βH188 (blue) coordinate polar moieties on ISRIB. Mutagenizing βH188 to more electron-rich aromatic residues, Tyr or Phe, (larger, darker blue circle), enhanced ISRIB binding, consistent with a stronger C-H-π interaction in the mutants (also see Figure 1.2F, Figure 1.3). The proposed upside-down "U-shaped" conformation of the ligand may be stabilized by weak intramolecular hydrogen bonds shown as dashed lines.

Figure 1.S7

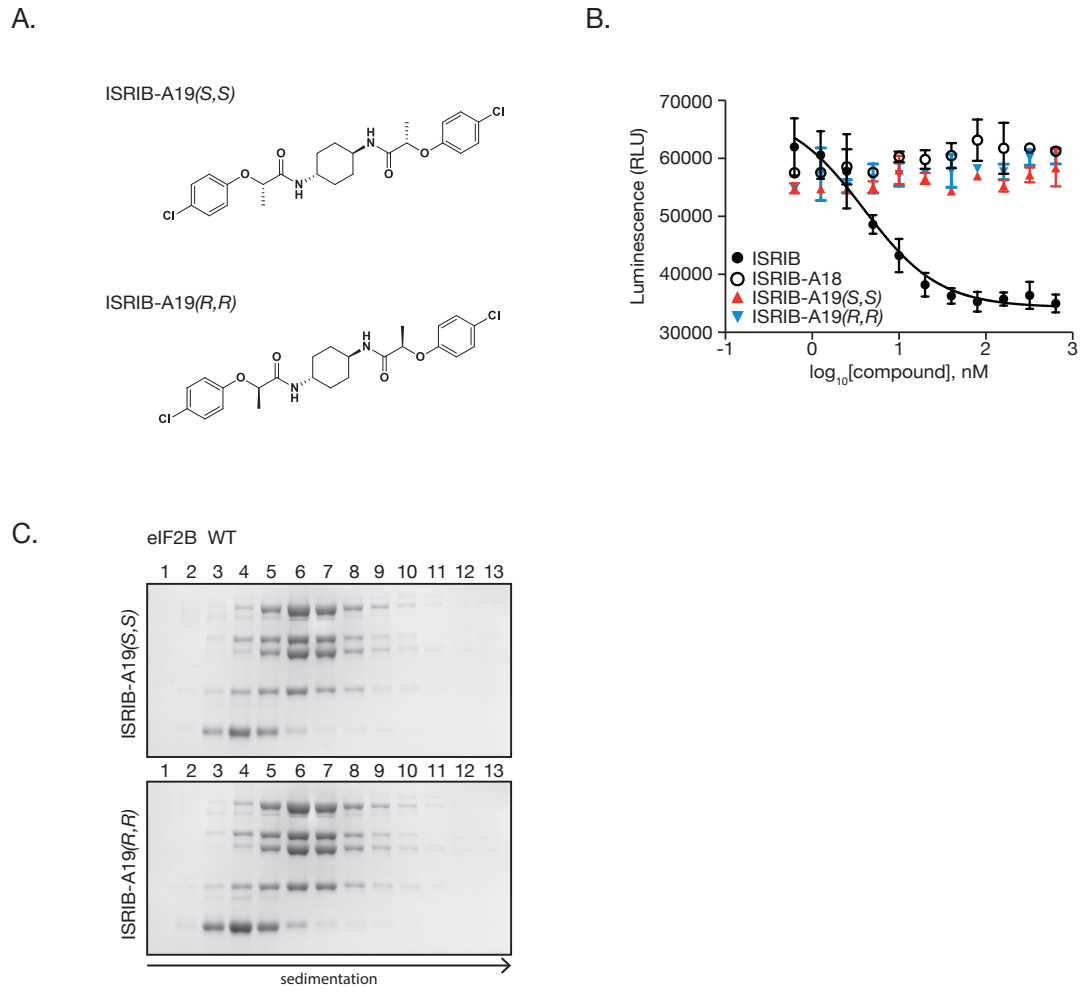

Characterization of ISRIB-A19 enantiomers A19*(R,R)* and A19*(S,S)*. (A) Chemical structure of ISRIB-A19*(R,R)* and ISRIB-A19*(S,S)*. (B) Cell-based ATF4-luciferase assay with ISRIB, a previously characterized inactive analog ISRIB-A18 (*28*), ISRIB-A19*(R,R)*, and ISRIB-*A19(S,S)* (n = 3). ISRIB was measured to have an EC_{50} of 3.94 nM for reversal of tunicamycin induced ATF-luciferase production. (C) Stability of eIF2B$(\alpha\beta\gamma\delta\varepsilon)_2$ in the presence of 500 nM ISRIB-A19*(R,R)* or ISRIB-*A19(S,S)* as assessed by velocity sedimentation on sucrose gradients.

Figure 1.S8

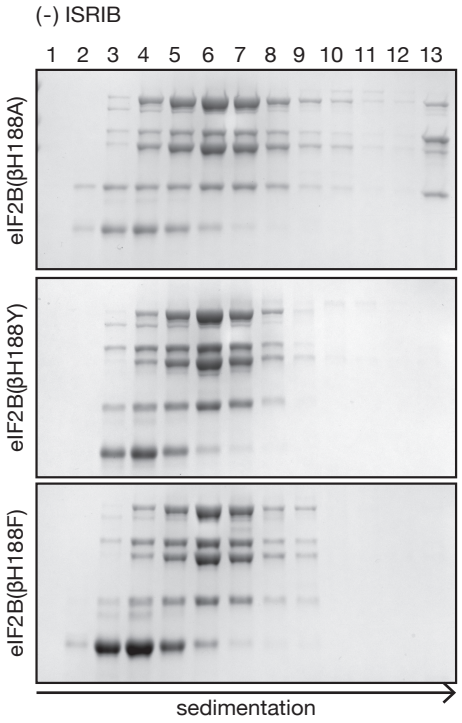

Characterization of βH188 mutations by sedimentation velocity. Stability of eIF2B$(\alpha\beta\gamma\delta\varepsilon)_2$ in the context of βH188A, βH188Y, and βH188F mutations as assessed by velocity sedimentation on sucrose gradients in the absence of ISRIB.

Figure 1.S9

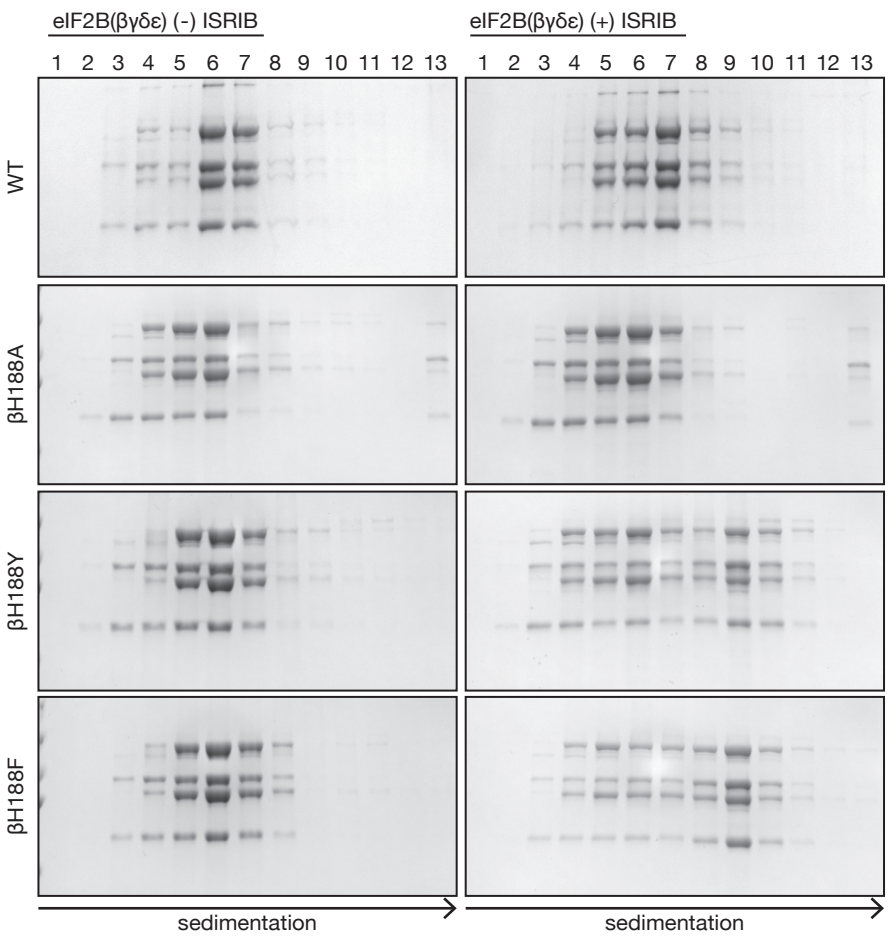

eIF2B(βγδε) mutants enhance ISRIB-mediated dimerization. Stability of eIF2B$(\beta\gamma\delta\varepsilon)_2$ in the context of wild-type, βH188A, βH188Y, and βH188F as assessed by velocity sedimentation on sucrose gradients in the presence and absence of ISRIB.

Table 1.S1

Data Collection Parameters

Data Collection				
	$eIF2B(\alpha\beta\gamma\delta\varepsilon)_2$ + ISRIB at Janelia	$eIF2B(\alpha\beta\gamma\delta\varepsilon)_2$ + ISRIB at Berkeley	$eIF2B(\alpha\beta\gamma\delta)$	$eIF2B(\alpha\beta\gamma\delta)$ + ISRIB
Pixel Size (Å)	1.02	0.838	1.15	1.15
Defocus Range (microns)	-0.3 to -3.9	-0.3 to -3.9	-0.7 to -5.5	-0.6 to -5.4
Defocus Mean (microns)	-2.0	-1.8	-1.9	-1.8
Voltage (kV)	300	300	200	200
Magnification (x)	29,000	29,000	36,000	36,000
Spherical Aberration (mm)	2.7	2.62	2.0	2.0
Detector	K2 Summit	K2 Summit	K2 Summit	K2 Summit
Detector Pixel Size (microns)	5.0	5.0	5.0	5.0
Per frame electron dose ($e^-/Å^2$)	1.19	1.63	1.2	1.2
# of frames	67	27	40	40
Frame Length (seconds)	0.15	0.18	0.2	0.2
Micrographs	1780	1515	129	67

Table 1.S2

Refinement Parameters

Refinement			
	eIF2B(αβγδε)$_2$ + ISRIB at Janelia	eIF2B(αβγδε)$_2$ + ISRIB at Berkeley	Combined
Particles following 2D classification	102599	99526	202,125
FSC Average Resolution, unmasked (Å)	3.8	3.5	3.0
FSC Average Resolution, masked (Å)	3.4	3.2	2.8
Map Sharpening B-factor	-75	-75	-78

Table 1.S3

Modeling

Model Statistics	
Number of Atoms, macromolecules	24208
Number of Atoms, ligands	60
Molprobity Score	1.62
Clashscore, all atoms	5.56
Favored Rotamers (%)	99.76
Outlier Rotamers (%)	0.24
RMS (bonds)	0.0047
RMS (angles)	1.16
Ramachandran Favored (%)	95.43
Ramachandran Outliers (%)	0.00
Ramachandran Allowed (%)	4.57

MATERIALS AND METHODS

Cloning of eIF2B expression plasmids

The five human eIF2B subunits were *E. coli*-codon optimized and synthesized on the BioXp 3200 System (SGI-DNA) in six blunt-end dsDNA fragments. Synthesized sequences are appended at the end of this document. Fragments were cloned into pCR-BluntII-TOPO vector with the Zero Blunt TOPO PCR Cloning Kit (Invitrogen), and verified by sequencing. In brief, subunits of eIF2B were PCR amplified from TOPO cloned vectors and Infusion (Clontech) cloned into multi-gene expression plasmids with compatible drug resistances and origins of replication: pETDuet-1 (Novagen 71146-3), pACYCDuet-1 (Novagen 71147-3), or pCOLADuet-1 (Novagen 71406-3) vectors. Each expression plasmid contains two cloning sites (site1 and site2), enabling simultaneous expression of up to two genes per plasmid. eIF2B1 (encoding the α subunit) was inserted into site1 of pETDuet-1 (pJT066). eIF2B2 (encoding the β subunit) and eIF2B4 (encoding the δ subunit) were inserted into site1 and site2 of pACYCDuet-1, respectively (pJT073). eIF2B3 (encoding the γ subunit) and eIF2B5 (encoding the ε subunit) were inserted into site1 and site2 of pCOLADuet-1, respectively (pJT074). To note eIF2B5 was synthesized in two fragments eIF2B5_1 and eIF2B5_2 that were simultaneously inserted into site2 by Infusion.

Purification of decameric eIF2B$(\alpha\beta\delta\gamma\varepsilon)_2$

pJT066, pJT073, and pJT074 were co-transformed into One Shot BL21 Star (DE3) chemically competent *E. coli* cells (Invitrogen) and grown in Luria-broth containing ampicillin, kanamycin, and chloramphenicol at 37˚ C on an orbital shaker. When the culture reached an OD600 of 0.6, the temperature was reduced to 16˚ C, induced with 0.8 mM IPTG (Gold Biotechnology), and

grown for 16 hours. Cells were harvested and lysed with the EmulsiFlex-C3 (Avestin) in a buffer containing [20 mM HEPES-KOH pH 7.5, 250 mM KCl, 1 mM tris(2-carboxyethyl)phosphine (TCEP), 5 mM $MgCl_2$, 15 mM imidazole, and complete EDTA-free protease inhibitor cocktail (Roche)]. The lysate was clarified at 30,000 x g for 20 min at 4˚ C. Subsequent purification steps were conducted on the ÄKTA Pure (GE Healthcare) system at 4˚ C.

The clarified lysate was loaded onto a HisTrap HP 5 ml, washed in binding buffer containing [20 mM HEPES-KOH pH 7.5, 200 mM KCl, 1 mM TCEP, 5 mM $MgCl_2$, 15 mM imidazole] and eluted with a linear gradient (75 ml) of 15 mM to 300 mM imidazole in the same buffer. The eIF2B fraction eluted from the HisTrap column at 80 mM imidazole. The eIF2B fraction was collected and loaded onto a 20 ml Mono Q HR16/10 column (GE Healthcare), washed in Buffer A [20 mM HEPES-KOH pH 7.5, 200 mM KCl, 1 mM TCEP, 5 mM $MgCl_2$] and eluted with a linear gradient (200 ml) of 200 mM to 500 mM KCl in the same buffer. The eIF2B fraction eluted off the Mono Q column at a conductivity of 46 mS/cm (corresponding to 390 mM KCl). Fractions were collected, concentrated with an Amicon Ultra-15 concentrator (EMD Millipore) with a 100,000 dalton molecular weight cut-off and loaded onto a Superdex 200 10/300 GL column (GE Healthcare) equilibrated with Buffer A. A typical preparation yielded approximately 0.5 mg of eIF2B$(\alpha\beta\delta\gamma\varepsilon)_2$ from a 1 liter culture.

EM Sample Preparation and Data Collection

Decameric eIF2B$(\alpha\beta\gamma\delta\varepsilon)_2$ + ISRIB: Following size exclusion chromatography, eIF2B$(\alpha\beta\gamma\delta\varepsilon)_2$ was diluted to 500 nM and a stock solution of 200 µM ISRIB in N-Methyl-2-pyrrolidone (NMP) was added to a final ISRIB concentration of 2 µM in a final solution containing [20 mM HEPES-KOH pH 7.5, 200 mM KCl, 1 mM TCEP, 5 mM $MgCl_2$, 0.5% NMP] and incubated on ice for 10

min. This sample was applied to either C-Flat 1.2/1.3-2C grids (EMS, USA) or Quantifoil R 1.2/1.3 200 Au mesh grids (Quantifoil, Germany). C-flat grids were used without additional cleaning or glow discharging. Quantifoil grids were soaked in chloroform for 30 min and desiccated overnight in a fume hood before use without glow discharging. Using a Vitrobot Mark IV at 4° C and 100% humidity, 3.5 µL of sample was applied to the grid, incubated for an additional 10 s, then blotted with -0.5 mm offset for ~6 s and plunge frozen in liquid ethane. Two datasets were collected on different microscopes. The first dataset was collected with the 300 kV Titan Krios "2" at the HHMI Janelia Research Campus using a K2 Summit detector operated in super-resolution mode. 1780 images were collected at a magnification of 29,000X (0.51 Å/pixel) as dose-fractionated stacks of 67 x 0.15 second exposures (1.19 $e^-/Å^2$) for a total dose of ~80 $e^-/Å^2$ (see Table S1). The second dataset was collected with the 300 kV Titan Krios at UC Berkeley using a K2 Summit detector operated in super-resolution mode. 1515 images were collected at a magnification of 29,000X (0.42 Å/pixel) as dose-fractionated stacks of 27 x 0.18 second exposures (1.83 $e^-/Å^2$) for a total dose of ~44 $e^-/Å^2$ (see Table S1).

Tetrameric eIF2B(αβγδ) +/- ISRIB: Following size exclusion chromatography, tetrameric eIF2B(αβγδ) was diluted to 800 nM and vitrified in the absence of ISRIB and in the presence of 2 µM ISRIB, as described above, but with ~4 s blot time. 129 micrographs of ligand-free and 67 micrographs of ISRIB-bound sample were collected on the 200 kV Talos Arctica at UCSF at 36,000X using a K2 Summit detector operated in super-resolution mode (1.15 Å/pixel).

Image Analysis and 3D Reconstruction

All dose-fractionated image stacks were corrected for motion artefacts, 2x binned in the Fourier domain, and dose-weighted using MotionCor2 (*35*), resulting in one dose-weighted and one

unweighted integrated image per stack with pixel sizes of 1.02Å (Janelia) or 0.838Å (UC Berkeley). The parameters of the Contrast Transfer Function (CTF) were estimated using GCTF-v1.06 (*36*) and the motion-corrected but unweighted images. ~1000 particles per dataset were manually selected and averaged in 2D using RELION 2.0 (*37*). The resulting class sums were then used as templates for automated particle picking using Gautomatch-v0.55 (*36*), followed by extraction and rescaling to a common pixel size of 0.838Å and four rounds of 2D classification (see Table S2).

For the 3D reconstruction of decameric eIF2B$(\alpha\beta\gamma\delta\varepsilon)_2$ + ISRIB, the resulting subset of particles were input into cryoSPARC (*38*) to compute an *ab-initio* reconstruction without symmetry, followed by homogeneous refinement in both cryoSPARC (dynamic masking) and in RELION 2.0 (unmasked) with no symmetry. Subsequent heterogeneous refinement (cryoSPARC) or multi-class 3D classification (RELION 2.0) removed less that 1% of the remaining particles (see Table S1).

High-resolution homogenous refinement was then performed in parallel in cryoSPARC, RELION 2.1, and FREALIGN (*39*) using soft-edged masks and imposed C2 symmetry (see Figure 1.S3-4). All three approaches yielded maps of similar visual quality and that differed in numerical resolution by ~0.1Å, as measured by Fourier shell correlation. All three maps were low-pass filtered and sharpened using automated procedures and used comparatively during model building in COOT and PHENIX (see below). Molecular graphics and analyses were performed with the UCSF Chimera package and the FREALIGN map. Chimera is developed by the Resource for Biocomputing, Visualization, and Informatics at UCSF (supported by NIGMS P41-GM103311, (*40*)). The map-versus-model FSC plots were generated using the FREALIGN map (see below and Figure 1.S4). Accession numbers for the human eIF2B structures

determined with FREALIGN, cryoSPARC, and RELION, respectively, are as follows: EMD-7442, EMD-7443, EMD-7444 (density maps; Electron Microscopy Data Bank) and 6CAJ (coordinates of atomic models; Protein Data Bank).

Atomic Modeling and Validation

An initial model of the human complex was generated using one-to-one threading as implemented in Phyre2 (*41*) using from the *S. pombe* crystal structure (PDB: 5B04, (*8*)) structure for the β, γ, δ, and ε subunits and the *H. sapiens* crystal structure (PDB: 3ECS, (*42*)) for the α subunit. The initial ISRIB ligand model was generated in PHENIX eLBOW (*43*) using the SMILES, manually adjusted in COOT (*44*), and then refined with phenix.real_space_refine (*45*) using global minimization and simulated annealing. This initial model was manually adjusted in COOT a second time and further refined in phenix.real_space_refine using global minimization, secondary structure restraints, and local grid search. This model was manually adjusted a third and final time in COOT, minimized in phenix.real_space_refine with per-residue B-factors, and the final model statistics were tabulated using Molprobity (*46*) (see Table S3). Map versus atomic model FSC plots for the entire decamer and the isolated βδβ'δ' chains were computed using EMAN 2 (*47*) using calculated density maps from e2pdb2mrc.py with heteroatoms (ISRIB) and per-residue B-factor weighting. Solvent accessible surfaces and buried surface areas were calculated from the atomic models using UCSF ChimeraX. Final atomic models have been deposited at the PDB with accession code 6CAJ.

Cloning of mutant eIF2B expression plasmids

Mutant eIF2B constructs were generated by site-directed mutagenesis on pJT073 using the primer indicated and its reverse complement. Highlighted bases indicate sites of mutagenesis.

δL179A (pJT091): 5’-tacggttctaaagtttctgctttctctcacctgccgcag-3’

βH188A (pJT089): 5’-gctgctcgtaaacgtaaattcgctgttatcgttgctgaatgcgct-3’

βH188F (pJT094): 5’-gctcgtaaacgtaaattcttcgttatcgttgctgaatg-3’

βH188Y (pJT095): 5’-gctgctcgtaaacgtaaattctacgttatcgttgctgaatg-3’

δL179V (pJT090): 5’-tacggttctaaagtttctgttttctctcacctgccgcag-3’

βH160D (pJT102): 5’-caggctctggaacacatcgactctaacgaagttatcatg-3’

Purification of tetrameric eIF2B(βδγε)

Tetrameric eIF2B(βδγε) and tetrameric eIF2B(βδγε) mutant proteins were purified using the same protocol as described for the decamer with the exception that expression strains were co-transformed without the eIF2B α subunit expressing plasmid. A typical preparation yielded approximately 0.75 mg of eIF2B(βδγε) from a 1 liter culture.

eIF2B(βδγε) tetramer with co-transformed plasmids: pJT073, pJT074

δL179A eIF2B(βδγε) tetramer with co-transformed plasmids: pJT091, pJT074

βH188A eIF2B(βδγε) tetramer with co-transformed plasmids: pJT089, pJT074

βH188F eIF2B(βδγε) tetramer with co-transformed plasmids: pJT094, pJT074

βH188Y eIF2B(βδγε) tetramer with co-transformed plasmids: pJT095, pJT074

δL179V eIF2B(βδγε) tetramer with co-transformed plasmids: pJT090, pJT074

βH160D eIF2B(βδγε) tetramer with co-transformed plasmids: pJT102, pJT074

Purification of eIF2B(α_2)

Purification of the eIF2B(α_2) was adapted from previously published purifications (*6*, *42*). The α subunit was N-terminally tagged with a 6x-His tag followed by a TEV cleavage site (pJT075). pJT075 was transformed into BL21 (DE3) *E. coli* cells and grown in Luria-broth containing ampicillin 37˚ C on an orbital shaker. When the culture reached an OD600 of 0.8, the temperature was reduced to 20˚ C, induced with 0.8 mM IPTG, and grown for 16 hours. Cells were harvested and lysed in a buffer containing [20 mM HEPES-KOH pH 7.5, 250 mM KCl, 1 mM TCEP, 5 mM $MgCl_2$, 20 mM imidazole, and 1x protease inhibitor cocktail] and clarified at 30,000 x g for 20 min at 4˚ C.

The clarified lysate was loaded onto a 5 ml HisTrap HP column, washed in a buffer containing [20 mM HEPES-KOH pH 7.5, 30 mM KCl, 1 mM TCEP, 5 mM $MgCl_2$, 20 mM imidazole] and eluted with 75 ml linear gradient of 20 mM to 300 mM imidazole. The HisTrap elution was then passed through a MonoQ HR 16/10 and subsequently a MonoS HR 10/10 (GE Healthcare), both equilibrated in a buffer containing [20 mM HEPES-KOH pH 7.5, 30 mM KCl, 1 mM TCEP, 5 mM $MgCl_2$]. eIF2B(α_2) was collected in the flow-through fractions of both MonoQ and MonoS columns. The eIF2B(α_2) containing fraction was incubated for 16 h at 4˚ C with TEV protease (50 μg TEV per liter of culture) and passed through on a HisTrap HP 5ml. Cleaved eIF2B(α_2) was recovered in the flow-through fraction, concentrated with an Amicon Ultra-15 concentrator (EMD Millipore) with a 30,000 Dalton molecular mass cut-off and chromatographed on a Superdex 75 10/300 GL (GE Healthcare) column equilibrated in a buffer containing [20 mM HEPES-KOH pH 7.5, 200 mM KCl, 1 mM TCEP, 5 mM $MgCl_2$, 5% glycerol]. A typical preparation yielded approximately 0.3 mg of eIF2B(α_2) from a 1 liter culture.

Preparation of human eIF2

Human eIF2 was prepared from an established recombinant *S. cerevisiae* expression protocol (*30*). In brief, the yeast strain GP6452 (kind gift from Graham Pavitt's lab, University of Manchester) containing yeast expression plasmids for human eIF2 subunits and a deletion of *GNC2* encoding the only eIF2 kinase in yeast, was grown to saturation in synthetic complete media (Sunrise Science Products) with auxotrophic markers (-Trp, -Leu, -Ura) in 2% dextrose. The β and α subunits of eIF2 were tagged with His6 and FLAG epitopes, respectively. A 12-liter yeast culture was grown in rich expression media containing yeast extract, peptone, 2% galactose and 0.2% dextrose. Cells were harvested and resuspended in lysis buffer [100 mM Tris pH 8.5, 300 mM KCl, 5 mM $MgCl_2$, 0.1% NP-40, 5 mM Imidazole, 10% glycerol (Thermo Fisher Scientific), 2 mM DTT, 1x protease inhibitor cocktail (Sigma Aldrich #11836170001), 1 µg/ml each aprotinin (Sigma Aldrich), leupeptin (Sigma Aldrich), pepstatin A (Sigma Aldrich)]. Cells were lysed in liquid nitrogen using a steel blender. The lysate was centrifuged at 10,000 x g for 1 h at 4˚C. Subsequent purification steps were conducted on the ÄKTA Pure (GE Healthcare) system at 4˚ C. Lysate was applied to a 5 ml HisTrap Crude column (Thermo Fisher Scientific) equilibrated in buffer [100 mM HEPES pH 7.5, 100 mM KCl, 5 mM $MgCl_2$, 0.1% NP-40, 5% glycerol, 1 mM dithiothreitol, 0.5x protease inhibitor cocktail, 1 µg/ml each aprotinin, leupeptin, pepstatin A]. eIF2 bound to the column, was washed with equilibration buffer and eluted using a 50 ml linear gradient of 5 mM to 500 mM imidazole. Eluted eIF2 was incubated with FLAG M2 magnetic affinity beads, washed with FLAG wash buffer [100 mM HEPES pH 7.5, 100 mM KCl, 5 mM $MgCl_2$, 0.1% NP-40, 5% glycerol, 1mM TCEP, 1x protease inhibitor cocktail, 1 µg/ml each aprotinin, leupeptin, pepstatin A] and eluted with FLAG elution buffer [identical to FLAG wash buffer but also containing 100 µg/ml 3x FLAG peptide (Sigma Aldrich)].

Concentration of purified protein was measured by BCA assay (Thermo Fisher Scientific # PI23225); protein was flash-frozen in liquid nitrogen and stored in elution buffer at -80° C. A typical preparation yielded 1 mg of eIF2 from a 12-liter culture.

GDP exchange assay

In vitro detection of GDP binding to eIF2 was adapted from a published protocol for a fluorescence intensity-based assay describing dissociation of eIF2 and nucleotide (*29*). We modified the procedure to establish both loading and unloading assays for fluorescent GDP.

For the 'GDP loading assay', purified eIF2 (200 pmol) was incubated with a molar equivalent Bodipy-FL-GDP (Thermo Fisher Scientific) in assay buffer [20 mM HEPES pH 7.5, 100 mM KCl, 5 mM $MgCl_2$, 1 mM TCEP, 1 mg/ml bovine serum albumin] to a volume of 18 µl in 384 square-well black-walled, clear-bottom polystyrene assay plates (Corning). The reaction was initiated by addition of 2 µl of buffer or purified eIF2B under various conditions to compare nucleotide exchange rates. For comparison of 'purified decamer' rates, eIF2B$(\alpha\beta\gamma\delta\varepsilon)_2$ (2 pmol) was pre-incubated in 0.1% NMP or 0.1% NMP and 2 µM ISRIB for 15 min. These concentrations of vehicle and ISRIB were used throughout, unless otherwise specified. To ensure equal concentrations of GEF catalytic sites in all experiments, comparisons with tetramer used eIF2B(βγδε) (4 pmol). 'Assembled decamer' was formed by incubating eIF2B(βγδε) (4 pmol) and eIF2B(α_2) (2 pmol) for 15 minutes in the presence or absence of ISRIB prior to mixing with substrate eIF2. For the 'GDP unloading assay', each reaction was initiated by addition of excess unlabeled GDP (200 nmol). Fluorescence intensity for both loading and unloading assays was recorded every ten seconds for 60 or 100 minutes using a TECAN Infinite M200 Pro plate reader

(excitation wavelength: 495 nm, bandwidth 5 nm, emission wavelength: 512 nm, bandwidth: 5 nm). Data collected were fit to a first-order exponential.

Analytical ultracentrifugation

Analytical ultracentrifugation sedimentation velocity experiments were conducted using the ProteomeLab XL-I system (Beckman Coulter) with a Ti60 rotor. Protein samples were loaded into cells in a buffer containing [20 mM HEPES-KOH pH 7.5, 150 mM KCl, 1 mM TCEP, 5 mM $MgCl_2$]. All runs were conducted at 20˚ C with a rotor speed of 40,000 rpm. Sedimentation was monitored at an absorbance of 280 nm. Subsequent data analysis was conducted with Sedfit (*48*) using a non-model based continuous c(s) distribution corrected for time invariant (TI) and radial invariant (RI) noise.

Sucrose gradients

Protocol was adapted from a previous study (*28*). 5-20% (w/v) sucrose gradients were prepared by tilted tube rotation on the Gradient Master 107ip (Biocomp) in a high salt buffer containing [20 mM HEPES-KOH pH 7.5, 400 mM KCl, 1 mM TCEP, 5 mM $MgCl_2$]. Protein samples contained 1 µM eIF2B(βδγε), 500 nM eIF2B(α_2), 500 nM ISRIB/analog (added from a 500 µM stock solution in NMP to yield a final NMP concentration of 0.1 %). For each gradient 200 µl of sample was loaded and centrifuges in a SW55 rotor (Beckman) for 14 hours at 40,000 rpm 4˚ C. Thirteen fractions of 400 µl were collected by aspirating from the top of the gradient, and protein was precipitated by addition of trichloroacetic acid to 15%. After incubation for 90 min on ice, the protein precipitate was collected by centrifugation, and the pellet was resuspended in SDS loading buffer, loaded on a 10% SDS-polyacrylamide gel (Bio-rad), and after electrophoresis

stained with Coomassie blue. Stained gels were then imaged on a ChemiDoc XRS+ imaging system (Bio-Rad). Quantification of gels was conducted in ImageJ. Fraction of total eIF2B(βγδε) in each of 13 lanes were quantified using a built-in gel-analyzer function. Area under each densitometry plot was calculated and divided by the sum of all areas measured from lanes 1-13 to obtain 'fraction of eIF2B(βγδε)'.

In-cell luciferase assays

Luciferase assays were conducted using a HEK293T cell line carrying an ATF4 luciferase reporter (*18*, *28*). Cells were plated at a density of 30,000 cells/well in a 96 well poly-lysine coated plate (Greiner Bio-One). Cells were treated the next day with 1 μg / ml tunicamycin and varying ISRIB concentrations for 7 h. Luciferase activity was then assayed using One Glo (Promega) and luminescence quantified in a SpectraMax M5 (Molecular Devices).

ISRIB-A19*(R,R)* and *(S,S)* synthesis & validation

(2S)-2-(4-chlorophenoxy)propanoic acid was purchased from Enamine. Reagents and solvents were purchased from Sigma- Aldrich, Acros or TCI America and used as received unless otherwise indicated. Flash column chromatography was carried out using a Biotage Isolera Four system and Silia*Sep* silica gel cartridges from Silicycle. ^{1}H NMR spectra were recorded on a Varian INOVA-400 400MHz spectrometer. Chemical shifts are reported in δ units (ppm) relative to residual NMR solvent peaks. Coupling constants (*J*) are reported in hertz (Hz). Characterization data are reported as follows: chemical shift, multiplicity (s=singlet, d=doublet, t=triplet, q=quartet, br=broad, m=multiplet), coupling constants, number of protons, mass to charge ratio. LC/MS analyses were performed on a Waters Micromass ZQ/Waters 2795 Separation Module/Waters 2996 Photodiode Array Detector/Waters 2424 Evaporative Light Scattering Detector system. Separations were carried out on XTerra® MS C_{18} 5µm 4.6x50mm column at ambient temperature using a mobile phase of water-methanol containing 0.1% formic acid.

Synthesis of (2*S*)-2-(4-Chlorophenoxy)-N-[(1r,4r)-4-[(2S)-2-(4-chlorophenoxy)propanamido]cyclohexyl]propanamide (ISRIB-A19*(S,S)*):

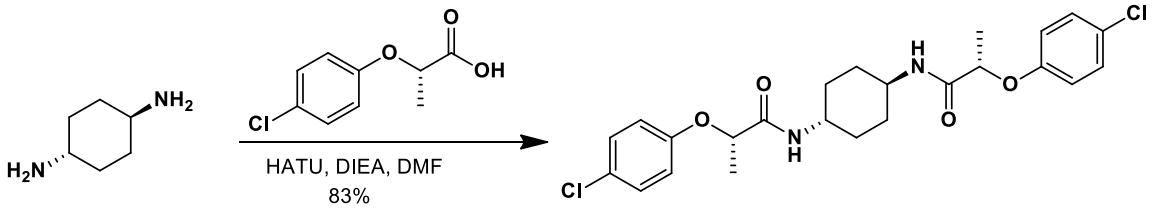

To a solution of the (2*S*)-2-(4-chlorophenoxy)propanoic acid (0.176 g, 0.88 mmol) in *N,N*-dimethylformamide (4 ml), was added HATU (0.35 g, 0.88 mmol), *trans*-1,4-diaminocyclohexane (0.05 g, 0.44 mmol), and *N,N*-diisopropylethylamine (0.3 ml, 1.76 mmol). The mixture was stirred at ambient temperature until the reaction was judged complete by LC/MS. The reaction mixture was then filtered and the collected material washed with diethyl ether, water, and then dried to obtain 175 mg (83%) of the title compound as a white solid. ^{1}H NMR (400 MHz, d_6-DMSO) δ 7.96 (d, *J* = 8 Hz, 2H), 7.30-7.34 (m, 4H), 6.89-6.93 (m, 4H), 4.63 (q, *J* = 6.6 Hz, 2H), 3.48 (br.s, 2H), 1.73 (d, *J* = 7.3 Hz, 2H), 1.64 (d, *J* = 7.3 Hz, 2H), 1.40(d, *J* = 6.6 Hz, 6H), 1.23-1.33 (m, 4H); 13C NMR (100 MHz, $CDCl_3$) δ 170.40, 156.85, 129.65, 125.17, 117.41, 74.31, 47.33, 31.16, 19.10; LCMS *m/z* 479 (MH+).

Synthesis of ethyl (2*R*)-2-(4-chlorophenoxy)propanoate:

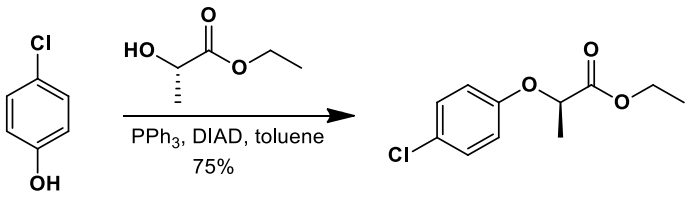

To a cooled (-20^o C) solution of ethyl (2*S*)-2-hydroxypropanoate (0.330 g, 2.8 mmol), 4-chlorophenol (0.359 g, 2.8 mmol) and triphenylphosphine (0.733 g, 2.8 mmol, 1.0 equiv.) in toluene was added diisopropyl azodicarboxylate (0.550 ml, 2.8 mmol). The mixture was stirred at -20^o C for an hour and then at ambient temperature for 24 hours. The reaction mixture was concentrated *in vacuo* to remove the toluene solvent. To the resulting residue was added hexanes and the precipitate that formed was filtered off. The filtrate was concentrated *in vacuo* and purified by flash column chromatography (25 g, 0-10% EA/hex) to obtain 0.48 g (75%) of the

product as a yellow oil. ^{1}H NMR (400 MHz, $CDCl_3$) δ 7.21-7.26 (m, 2H), 6.80-6.84 (m, 2H), 4.71 (q, *J* = 6.8 Hz, 1H), 4.20-4.25 (m, 2H), 1.62 (d, *J* = 6.8 Hz, 3H), 1.26 (t, *J* = 7.2 Hz, 3H); LCMS *m/z* 228 (MH+).

Synthesis of (2R)-2-(4-Chlorophenoxy)-N-[(1r,4r)-4-[(2R)-2-(4-chlorophenoxy)propanamido]cyclohexyl]propanamide (ISRIB-A19*(R,R)*):

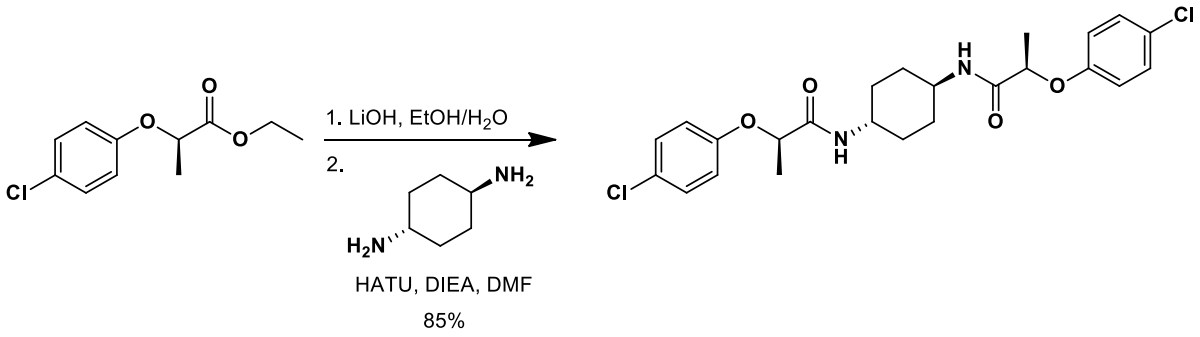

To a solution of ethyl (2R)-2-(4-chlorophenoxy)propanoate (0.150 g, 0.7 mmol) in 2:1 mixture of ethanol-water (6 ml) was added 1 M aqueous lithium hydroxide solution (1.312 ml, 1.3 mmol). The mixture was stirred at ambient temperature for 24 h. The reaction mixture was concentrated *in vacuo* to remove ethanol, diluted with water and adjusted to pH 2 with 1 N aqueous hydrochloric acid solution. The mixture was extracted with ethyl acetate. The organic extracts were washed with brine, dried over magnesium sulfate and concentrated to obtain 123 mg of (2R)-2-(4-chlorophenoxy)propanoic acid as a white solid. This material was used directly in the next reaction.

To a solution of the (2R)-2-(4-chlorophenoxy)propanoic acid (0.1 g, 0.5 mmol) in *N,N*-dimethylformamide (2 ml), was added HATU (0.2 g, 0.525 mmol), *trans*-1,4-diaminocyclohexane (0.028 g, 0.25 mmol), and *N,N*-diisopropylethylamine (0.174 ml, 1.0 mmol). The mixture was stirred at ambient temperature until the reaction was judged complete

by LC/MS. The reaction mixture was filtered and the collected material was washed with diethyl ether, water, and then dried to obtain 100 mg (85%) of the title compound as a white solid. ^{1}H NMR (400 MHz, d_6-DMSO) δ 7.96 (d, J = 8.3 Hz, 2H), 7.30-7.34 (m, 4H), 6.88-6.92 (m, 4H), 4.63 (q, J = 6.5 Hz, 2H), 3.49 (br.s, 2H), 1.73 (d, J = 8.3 Hz, 2H), 1.64 (d, J = 7.3 Hz, 2H), 1.44 (d, J = 6.6 Hz, 6H), 1.22-1.30 (m, 4H); LCMS *m/z* 479 (MH+).

Confirmation of inversion of configuration in preparation of intermediates for ISRIB-A19*(R,R)* synthesis.

To confirm inversion of stereochemical configuration during the preparation of ethyl (2*R*)-2-(4-chlorophenoxy)propanoate, the (2*S*)-2-(4-chlorophenoxy)propanoic acid and (2*R*)-2-(4-chlorophenoxy)propanoic acid used in the preparation of ISRIB-A19*(S,S)* and ISRIB-A19*(R,R)*, respectively, were coupled to (*R*)-(+)-alpha-methylbenzylamine as detailed below. The resulting amides were found to be single and distinct diastereoisomers, confirming the enantiomeric relationship of the propanoic acids and accordingly of ISRIB-A19*(R,R) and* ISRIB-A19*(R,R)*.

Synthesis of (2*S*)-2-(4-chlorophenoxy)-N-[(1*R*)-1-phenylethyl]propanamide:

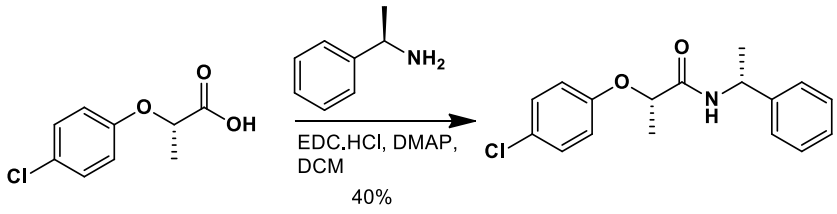

To a solution of (2*S*)-2-(4-chlorophenoxy)propanoic acid (0.050 g, 0.2 mmol) in CH_2Cl_2 (3 ml) was added 1-(3-dimethylaminopropyl)-3-ethylcarbodiimide hydrochloride (0.048 g, 0.3 mmol),

4-dimethylaminopyridine (0.003 g, 0.025 mmol), and finally (*R*)-(+)-alpha-methylbenzylamine (0.032 ml, 0.2 mmol). The mixture was stirred at ambient temperature for 24 h. The reaction mixture was then washed with saturated aqueous ammonium chloride, water and brine. The organic layer was separated, dried over magnesium sulfate, filtered and concentrated. The crude product was purified by flash column chromatography (0-50% EtOAc/hexanes) to yield 30 mg (40%) of the title compound as a white solid. ^{1}H NMR (400 MHz, $CDCl_3$) δ 7.36-7.40 (m, 2H), 7.27-7.32 (m, 5H), 6.86-6.90 (m, 2H), 6.59 (d, *J* = 7.8 Hz, 1H), 5.15-5.20 (m, 1H), 4.66 (q, *J* = 6.8 Hz, 1H), 1.56 (d, *J* = 6.6 Hz, 3H), 1.43 (d, *J* = 6.8 Hz, 3H); 13C NMR (100 MHz, $CDCl_3$) δ 170.84, 155.49, 142.68, 129.79, 127.53, 127.12, 126.05, 116.87, 75.59, 48.27, 21.63, 18.68; LCMS *m/z* 304 (MH+).

Synthesis of (2*R*)-2-(4-chlorophenoxy)-N-[(1*R*)-1-phenylethyl]propanamide:

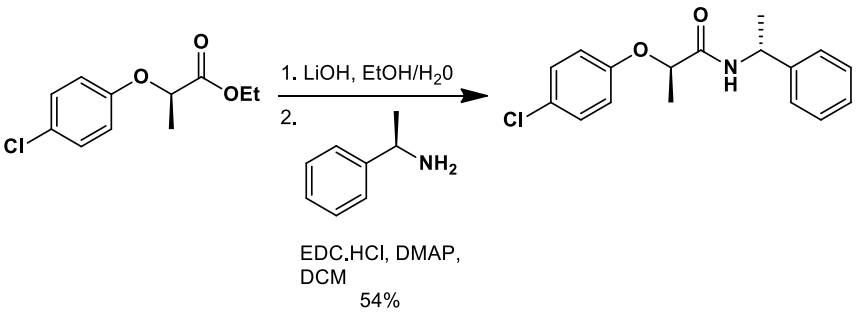

To a solution of ethyl (2*R*)-2-(4-chlorophenoxy)propanoate (0.1 g, 0.44 mmol) in a 2:1 mixture of ethanol-water (6 ml) was added 1 M aqueous lithium hydroxide solution (0.88 ml, 0.88 mmol). The mixture was stirred at ambient temperature for 18 h. The reaction mixture was concentrated *in vacuo* to remove ethanol, diluted with water and adjusted to pH 2 with 1N aqueous hydrochloric acid solution. The mixture was extracted with ethyl acetate. The organic extracts were washed with brine, dried over magnesium sulfate and concentrated to obtain 85 mg

of (2*R*)-2-(4-chlorophenoxy)propanoic acid as a white solid. This material was used directly in the next step.

To a solution of the (2*R*)-2-(4-chlorophenoxy)propanoic acid (0.085 g, 0.42 mmol) in CH_2Cl_2 (5 ml) was added 1-(3-dimethylaminopropyl)-3-ethylcarbodiimide hydrochloride (0.082 g, 0.43 mmol), 4-dimethylaminopyridine (0.005 g, 0.042 mmol), and finally (*R*)-(+)-alpha-methylbenzylamine (0.054 ml, 0.42 mmol). The mixture was stirred at ambient temperature for 24 hours. The reaction mixture was then washed with saturated aqueous ammonium chloride, water and brine. The organic layer was separated, dried over magnesium sulfate, filtered and concentrated. The crude product was purified by flash column chromatography (0-50% EtOAc/hexanes) to yield 70 mg (54%) of the title compound as a white solid. ^{1}H NMR (400 MHz, $CDCl_3$) δ 7.21-7.26 (m, 5H), 7.09-7.11 (m, 2H), 6.79-6.83 (m, 2H), 6.56-6.58 (m, 1H), 5.10-5.18 (m, 1H), 4.63 (q, *J* = 6.7 Hz, 1H), 1.61 (d, *J* = 6.6 Hz, 3H), 1.52 (d, *J* = 7.1 Hz, 3H); 13C NMR (100 MHz, $CDCl_3$) δ 170.96, 155.46, 142.67, 129.67, 128.58, 127.36, 127.08, 125.91, 116.89, 75.50, 48.30, 21.80, 18.77; LCMS *m/z* 304 (MH+).

Synthesis Validation

10/12/2017 12:32:42 PM
(2S)-2-(4-Chlorophenoxy)-N-[(1r,4r)-4-[(2S)-2-(4-chlorophenoxy)propanamido]cyclohexyl]propanamide (1014817)

Acquisition Time (sec)	4.1069	*Comment*	Z116098_0411 (PA BBO 400S1 BBF-H-D-05 Z SP)			*Date*	15 Feb 2017 14:24:00
Date Stamp	15 Feb 2017 14:24:00			*File Name*	C:\Users\priya\Desktop\NMRSpectra\NMR#149\149FTD's\PJ149-10\1\fid		
Frequency (MHz)	399.54	*Nucleus*	1H	*Number of Transients*	16	*Origin*	spect
Original Points Count	32768	*Owner*	SMDC_A	*Points Count*	32768	*Pulse Sequence*	zg30
Receiver Gain	166.07	*SW(cyclical) (Hz)*	7978.72	*Solvent*	DMSO-d6	*Spectrum Offset (Hz)*	2467.1362
Spectrum Type	STANDARD	*Sweep Width (Hz)*	7978.48	*Temperature (degree C)*	24.996		

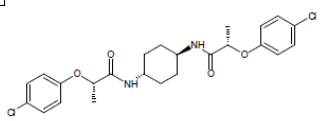

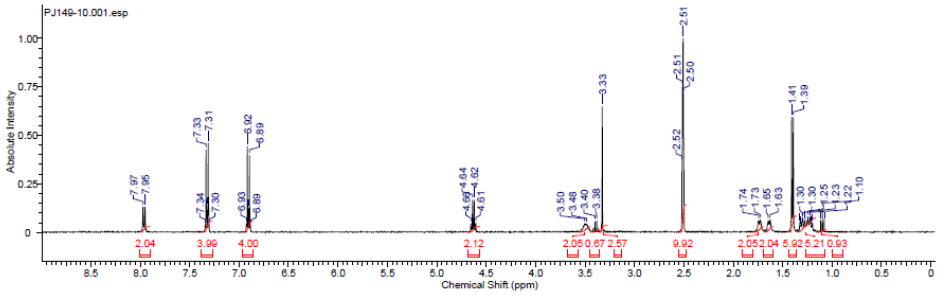

10/12/2017 12:35:49 PM
(2S)-2-(4-Chlorophenoxy)-N-[(1r,4r)-4-[(2S)-2-(4-chlorophenoxy)propanamido]cyclohexyl]propanamide (1014817)

Acquisition Time (sec)	1.3631	*Comment*	Z116098_0411 (PA BBO 400S1 BBF-H-D-05 Z SP)			*Date*	12 Oct 2017 09:42:40
Date Stamp	12 Oct 2017 09:42:40			*File Name*	C:\Users\priya\Desktop\NMRSpectra\NMR#149\149FTD's\PJ149-10C13\1\fid		
Frequency (MHz)	100.46	*Nucleus*	13C	*Number of Transients*	167	*Origin*	spect
Original Points Count	32768	*Owner*	SMDC_A	*Points Count*	32768	*Pulse Sequence*	zgpg30
Receiver Gain	208.51	*SW(cyclical) (Hz)*	24038.46	*Solvent*	DMSO-d6	*Spectrum Offset (Hz)*	10046.3408
Spectrum Type	STANDARD	*Sweep Width (Hz)*	24037.73	*Temperature (degree C)*	24.996		

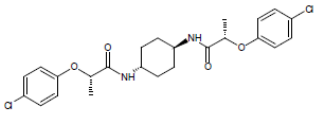

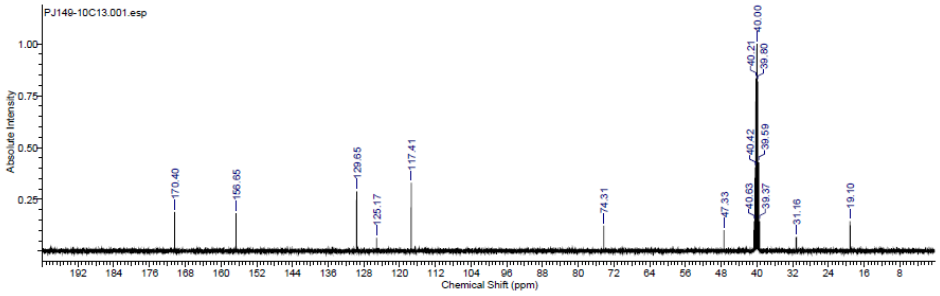

10/12/2017 12:38:37 PM
(2R)-2-(4-Chlorophenoxy)-N-[(1r,4r)-4-[(2R)-2-(4-chlorophenoxy)propanamido]cyclohexyl]propanamide (1014869)

Acquisition Time (sec)	4.1069	*Comment*	Z116098_0411 (PA BBO 400S1 BBF-H-D-05 Z SP)			*Date*	15 Mar 2017 09:23:28
Date Stamp	15 Mar 2017 09:23:26			*File Name*	C:\Users\priya\Desktop\NMRSpectra\NMR#149\149FTD's\PJ149-27\1\fid		
Frequency (MHz)	399.54	*Nucleus*	1H	*Number of Transients*	16	*Origin*	spect
Original Points Count	32768	*Owner*	SMDC_A	*Points Count*	32768	*Pulse Sequence*	zg30
Receiver Gain	185.41	*SW(cyclical) (Hz)*	7978.72	*Solvent*	DMSO-d6	*Spectrum Offset (Hz)*	2467.1362
Spectrum Type	STANDARD	*Sweep Width (Hz)*	7978.48	*Temperature (degree C)*	25.002		

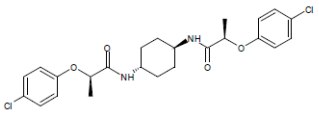

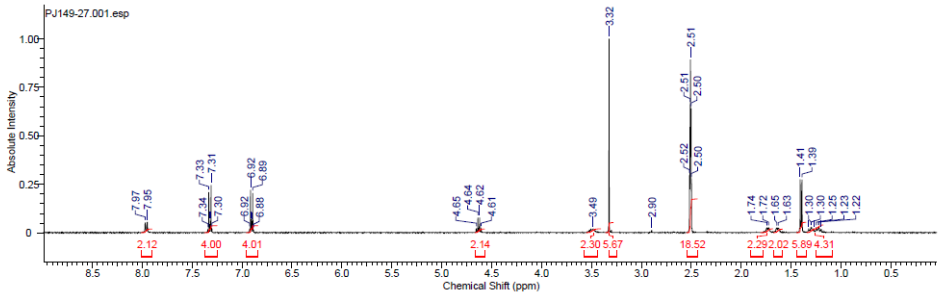

10/10/2017 11:16:06 AM
(2S)-2-(4-chlorophenoxy)-N-[(1R)-1-phenylethyl]propanamide

Acquisition Time (sec)	4.1069	*Comment*	Z116098_0411 (PA BBO 400S1 BBF-H-D-05 Z SP)			*Date*	25 Sep 2017 10:12:32
Date Stamp	25 Sep 2017 10:12:32			*File Name*	C:\Users\priya\Desktop\NMRSpectra\NMR#149\149FTD's\PJ149-127\1\fid		
Frequency (MHz)	399.54	*Nucleus*	1H	*Number of Transients*	16	*Origin*	spect
Original Points Count	32768	*Owner*	SMDC_A	*Points Count*	32768	*Pulse Sequence*	zg30
Receiver Gain	74.50	*SW(cyclical) (Hz)*	7978.72	*Solvent*	CHLOROFORM-d		
Spectrum Offset (Hz)	2467.1362	*Spectrum Type*	STANDARD	*Sweep Width (Hz)*	7978.48	*Temperature (degree C)*	25.002

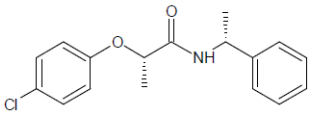

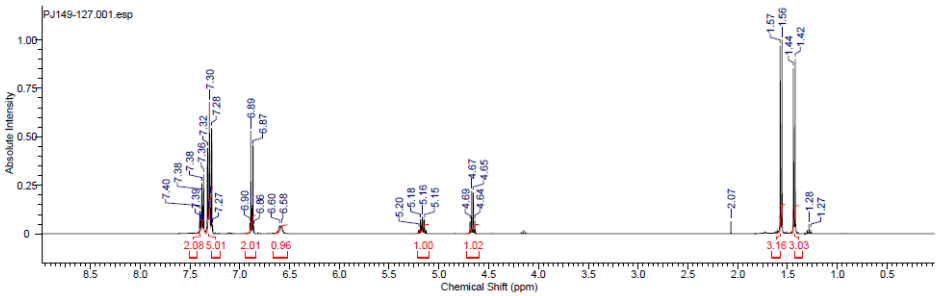

10/12/2017 11:22:58 AM
(2S)-2-(4-chlorophenoxy)-N-[(1R)-1-phenylethyl]propanamide

Acquisition Time (sec)	1.3631	*Comment*	Z116098_0411 (PA BBO 400S1 BBF-H-D-05 Z SP)			*Date*	25 Sep 2017 10:16:48
Date Stamp	25 Sep 2017 10:16:48			*File Name*	C:\Users\priya\Desktop\NMRSpectra\NMR#149\149FTD's\PJ149-127C13\1\fid		
Frequency (MHz)	100.46	*Nucleus*	13C	*Number of Transients*	130	*Origin*	spect
Original Points Count	32768	*Owner*	SMDC_A	*Points Count*	32768	*Pulse Sequence*	zgpg30
Receiver Gain	208.51	*SW(cyclical) (Hz)*	24038.46	*Solvent*	CHLOROFORM-d		
Spectrum Offset (Hz)	10046.3408	*Spectrum Type*	STANDARD	*Sweep Width (Hz)*	24037.73	*Temperature (degree C)*	25.008

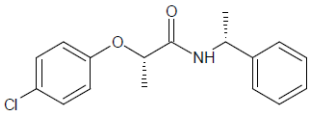

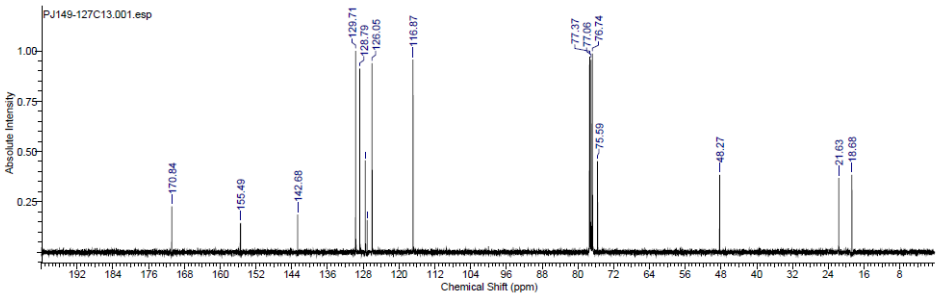

10/12/2017 11:29:54 AM
(2R)-2-(4-chlorophenoxy)-N-[(1R)-1-phenylethyl]propanamide

Acquisition Time (sec)	4.1069	*Comment*	Z116098_0411 (PA BBO 400S1 BBF-H-D-05 Z SP)			*Date*	27 Sep 2017 13:03:12
Date Stamp	27 Sep 2017 13:03:12			*File Name*	C:\Users\priya\Desktop\NMRSpectra\NMR#149\149FTD's\PJ149-129\1\fid		
Frequency (MHz)	399.54	*Nucleus*	1H	*Number of Transients*	16	*Origin*	spect
Original Points Count	32768	*Owner*	SMDC_A	*Points Count*	32768	*Pulse Sequence*	zg30
Receiver Gain	93.24	*SW(cyclical) (Hz)*	7978.72	*Solvent*	CHLOROFORM-d		
Spectrum Offset (Hz)	2467.1362	*Spectrum Type*	STANDARD	*Sweep Width (Hz)*	7978.48	*Temperature (degree C)*	24.999

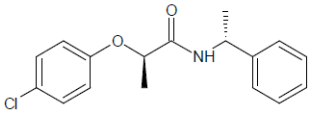

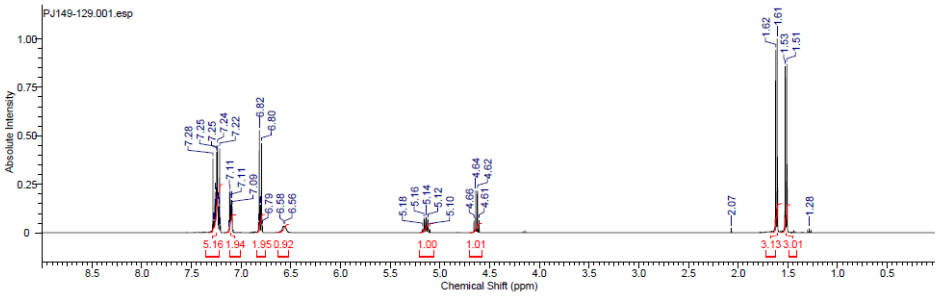

10/12/2017 12:26:50 PM
(2R)-2-(4-chlorophenoxy)-N-[(1R)-1-phenylethyl]propanamide

Acquisition Time (sec)	1.3631	*Comment*	Z116098_0411 (PA BBO 400S1 BBF-H-D-05 Z SP)			*Date*	27 Sep 2017 13:13:52
Date Stamp	27 Sep 2017 13:13:52			*File Name*	C:\Users\priya\Desktop\NMRSpectra\NMR#149\149FTD's\PJ149-129C13\2\fid		
Frequency (MHz)	100.46	*Nucleus*	13C	*Number of Transients*	131	*Origin*	spect
Original Points Count	32768	*Owner*	SMDC_A	*Points Count*	32768	*Pulse Sequence*	zgpg30
Receiver Gain	208.51	*SW(cyclical) (Hz)*	24038.46	*Solvent*	CHLOROFORM-d		
Spectrum Offset (Hz)	10046.3408	*Spectrum Type*	STANDARD	*Sweep Width (Hz)*	24037.73	*Temperature (degree C)*	24.999

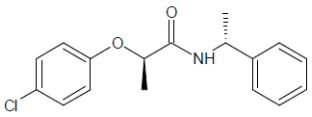

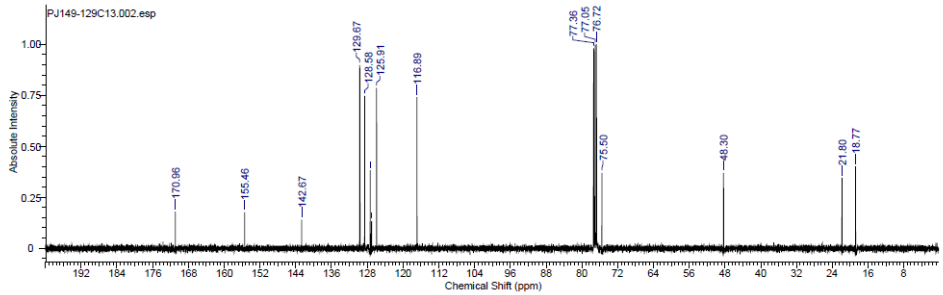

Sequences

> heIF2B1_alpha_codonopt

ATGGACGACAAAGAACTGATCGAATACTTCAAATCTCAGATGAAAGAAGACCC
GGACATGGCTTCTGCTGTTGCTGCTATCCGTACCCTGCTGGAGTTCCTGAAACGTGA
CAAAGGTGAAACCATCCAGGGTCTGCGTGCTAACCTGACCTCTGCTATCGAAACCCT
GTGCGGTGTTGACTCTTCTGTTGCTGTTTCTTCTGGTGGTGAACTGTTCCTGCGTTTC
ATCTCTCTGGCTTCTCTGGAATACTCTGACTACTCTAAATGCAAAAAAATCATGATC
GAACGTGGTGAACTGTTCCTGCGTCGTATCTCTCTGTCTCGTAACAAAATCGCTGAC
CTGTGCCACACCTTCATCAAAGACGGTGCTACCATCCTGACCCACGCTTACTCTCGT
GTTGTTCTGCGTGTTCTGGAAGCTGCTGTTGCTGCTAAAAAACGTTTCTCTGTTTACG
TTACCGAATCTCAGCCGGACCTGTCTGGTAAAAAAATGGCTAAAGCTCTGTGCCACC
TGAACGTTCCGGTTACCGTTGTTCTGGACGCTGCTGTTGGTTACATCATGGAAAAAG
CTGACCTGGTTATCGTTGGTGCTGAAGGTGTTGTTGAAAACGGTGGTATCATCAACA
AAATCGGTACCAACCAGATGGCTGTTTGCGCTAAAGCTCAGAACAAACCGTTCTACG
TTGTTGCTGAATCTTTCAAATTCGTTCGTCTGTTCCCGCTGAACCAGCAGGACGTTCC
GGACAAATTCAAATACAAAGCTGACACCCTGAAAGTTGCTCAGACCGGTCAGGACC
TGAAAGAAGAACACCCGTGGGTTGACTACACCGCTCCGTCTCTGATCACCCTGCTGT
TCACCGACCTGGGTGTTCTGACCCCGTCTGCTGTTTCTGACGAACTGATCAAACTGT
ACCTGTAA

>heIF2B2_beta_codonopt | 6x His tag, TEV site

ATGCATCACCATCATCACCACGGTGGTGGTTCTGAAAACCTGTACTTCCAGTCT
CCGGGTTCTGCTGCTAAAGGTTCTGAACTGTCTGAACGTATCGAATCTTTCGTTGAA
ACCCTGAAACGTGGTGGTGGTCCGCGTTCTTCTGAAGAAATGGCTCGTGAAACCCTG
GGTCTGCTGCGTCAGATCATCACCGACCACCGTTGGTCTAACGCTGGTGAACTGATG
GAACTGATCCGTCGTGAAGGTCGTCGTATGACCGCTGCTCAGCCGTCTGAAACCACC
GTTGGTAACATGGTTCGTCGTGTTCTGAAAATCATCCGTGAAGAATACGGTCGTCTG
CACGGTCGTTCTGACGAATCTGACCAGCAGGAATCTCTGCACAAACTGCTGACCTCT
GGTGGTCTGAACGAAGACTTCTCTTTCCACTACGCTCAGCTGCAGTCTAACATCATC
GAAGCTATCAACGAACTGCTGGTTGAACTGGAAGGTACGATGGAAAACATCGCTGC
TCAGGCTCTGGAACACATCCACTCTAACGAAGTTATCATGACCATCGGTTTCTCTCG
TACCGTTGAAGCTTTCCTGAAAGAAGCTGCTCGTAAACGTAAATTCCACGTTATCGT
TGCTGAATGCGCTCCGTTCTGCCAGGGTCACGAAATGGCTGTTAACCTGTCTAAAGC
TGGTATCGAAACCACCGTTATGACCGACGCTGCTATCTTCGCTGTTATGTCTCGTGTT
AACAAAGTTATCATCGGTACCAAAACCATCCTGGCTAACGGTGCTCTGCGTGCTGTT
ACCGGTACCCACACCCTGGCTCTGGCTGCTAAACACCACTCTACCCCGCTGATCGTT
TGCGCTCCGATGTTCAAACTGTCTCCGCAGTTCCCGAACGAAGAAGACTCTTTCCAC
AAATTCGTTGCTCCGGAAGAAGTTCTGCCGTTCACCGAAGGTGACATCCTGGAAAAA
GTTTCTGTTCACTGCCCGGTTTTCGACTACGTTCCGCCGGAACTGATCACCCTGTTCA
TCTCTAACATCGGTGGTAACGCTCCGTCTTACATCTACCGTCTGATGTCTGAACTGTA
CCACCCGGACGACCACGTTCTGTAA

>heIF2B3_gamma_codonopt

ATGGAGTTCCAGGCTGTTGTTATGGCTGTTGGTGGTGGTTCTCGTATGACCGAC
CTGACCTCTTCTATCCCGAAACCGCTGCTGCCGGTTGGTAACAAACCGCTGATCTGG

TACCCGCTGAACCTGCTGGAACGTGTTGGTTTCGAAGAAGTTATCGTTGTTACCACC
CGTGACGTTCAGAAAGCTCTGTGCGCTGAGTTCAAAATGAAAATGAAACCGGACAT
CGTTTGCATCCCGGACGACGCTGACATGGGTACCGCTGACTCTCTGCGTTACATCTA
CCCGAAACTGAAAACCGACGTTCTGGTTCTGTCTTGCGACCTGATCACCGACGTTGC
TCTGCACGAAGTTGTTGACCTGTTCCGTGCTTACGACGCTTCTCTGGCTATGCTGATG
CGTAAAGGTCAGGACTCTATCGAACCGGTTCCGGGTCAGAAAGGTAAAAAAAAAGC
TGTTGAACAGCGTGACTTCATCGGTGTTGACTCTACCGGTAAACGTCTGCTGTTCAT
GGCTAACGAAGCTGACCTGGACGAAGAACTGGTTATCAAAGGTTCTATCCTGCAGA
AACACCCGCGTATCCGTTTCCACACCGGTCTGGTTGACGCTCACCTGTACTGCCTGA
AAAAATACATCGTTGACTTCCTGATGGAAAACGGTTCTATCACCTCTATCCGTTCTG
AACTGATCCCGTACCTGGTTCGTAAACAGTTCTCTTCTGCTTCTTCTCAGCAGGGTCA
GGAAGAAAAAGAAGAAGACCTGAAAAAAAAAGAACTGAAATCTCTGGACATCTAC
TCTTTCATCAAAGAAGCTAACACCCTGAACCTGGCTCCGTACGACGCTTGCTGGAAC
GCTTGCCGTGGTGACCGTTGGGAAGACCTGTCTCGTTCTCAGGTTCGTTGCTACGTTC
ACATCATGAAAGAAGGTCTGTGCTCTCGTGTTTCTACCCTGGGTCTGTACATGGAAG
CTAACCGTCAGGTTCCGAAACTGCTGTCTGCTCTGTGCCCGGAAGAACCGCCGGTTC
ACTCTTCTGCTCAGATCGTTTCTAAACACCTGGTTGGTGTTGACTCTCTGATCGGTCC
GGAAACCCAGATCGGTGAAAAATCTTCTATCAAACGTTCTGTTATCGGTTCTTCTTG
CCTGATCAAAGACCGTGTTACCATCACCAACTGCCTGCTGATGAACTCTGTTACCGT
TGAAGAAGGTTCTAACATCCAGGGTTCTGTTATCTGCAACAACGCTGTTATCGAAAA
AGGTGCTGACATCAAAGACTGCCTGATCGGTTCTGGTCAGCGTATCGAAGCTAAAGC
TAAACGTGTTAACGAAGTTATCGTTGGTAACGACCAGCTGATGGAAATCTAA

>heIF2B4_delta_codonopt | isoform 2

ATGGCTGCTGTTGCTGTTGCTGTTCGTGAAGACTCTGGTTCTGGTATGAAAGCTG
AACTGCCGCCGGGTCCGGGTGCTGTTGGTCGTGAAATGACCAAAGAAGAAAAACTG
CAGCTGCGTAAAGAAAAAAAACAGCAGAAAAAAAAACGTAAAGAAGAAAAAGGTG
CTGAACCGGAAACCGGTTCTGCTGTTTCTGCTGCTCAGTGCCAGGTTGGTCCGACCC
GTGAACTGCCGGAATCTGGTATCCAGCTGGGTACCCCGCGTGAAAAAGTTCCGGCTG
GTCGTTCTAAAGCTGAACTGCGTGCTGAACGTCGTGCTAAACAGGAAGCTGAACGT
GCTCTGAAACAGGCTCGTAAAGGTGAACAGGGTGGTCCGCCGCCGAAAGCTTCTCC
GTCTACCGCTGGTGAAACCCCGTCTGGTGTTAAACGTCTGCCGGAATACCCGCAGGT
TGACGACCTGCTGCTGCGTCGTCTGGTTAAAAAACCGGAACGTCAGCAGGTTCCGAC
CCGTAAAGACTACGGTTCTAAAGTTTCTCTGTTCTCTCACCTGCCGCAGTACTCTCGT
CAGAACTCTCTGACCCAGTTCATGTCTATCCCGTCTTCTGTTATCCACCCGGCTATGG
TTCGTCTGGGTCTGCAGTACTCTCAGGGTCTGGTTTCTGGTTCTAACGCTCGTTGCAT
CGCTCTGCTGCGTGCTCTGCAGCAGGTTATCCAGGACTACACCACCCCGCCGAACGA
AGAACTGTCTCGTGACCTGGTTAACAAACTGAAACCGTACATGTCTTTCCTGACCCA
GTGCCGTCCGCTGTCTGCTTCTATGCACAACGCTATCAAATTCCTGAACAAAGAAAT
CACCTCTGTTGGTTCTTCTAAACGTGAAGAAGAAGCTAAATCTGAACTGCGTGCTGC
TATCGACCGTTACGTTCAGGAAAAAATCGTTCTGGCTGCTCAGGCTATCTCTCGTTTC
GCTTACCAGAAAATCTCTAACGGTGACGTTATCCTGGTTTACGGTTGCTCTTCTCTGG
TTTCTCGTATCCTGCAGGAAGCTTGGACCGAAGGTCGTCGTTTCCGTGTTGTTGTTGT
TGACTCTCGTCCGTGGCTGGAAGGTCGTCACACCCTGCGTTCTCTGGTTCACGCTGGT
GTTCCGGCTTCTTACCTGCTGATCCCGGCTGCTTCTTACGTTCTGCCGGAAGTTTCTA
AAGTTCTGCTGGGTGCTCACGCTCTGCTGGCTAACGGTTCTGTTATGTCTCGTGTTGG

TACCGCTCAGCTGGCTCTGGTTGCTCGTGCTCACAACGTTCCGGTTCTGGTTTGCTGC
GAAACCTACAAATTCTGCGAACGTGTTCAGACCGACGCTTTCGTTTCTAACGAACTG
GACGACCCGGACGACCTGCAGTGCAAACGTGGTGAACACGTTGCTCTGGCTAACTG
GCAGAACCACGCTTCTCTGCGTCTGCTGAACCTGGTTTACGACGTTACCCCGCCGGA
ACTGGTTGACCTGGTTATCACCGAACTGGGTATGATCCCGTGCTCTTCTGTTCCGGTT
GTTCTGCGTGTTAAATCTTCTGACCAGTAA

>heIF2B5_epsilon1_codonopt | overlap

ATGGCTGCTCCGGTTGTTGCTCCGCCGGGTGTTGTTGTTTCTCGTGCTAACAAAC
GTTCTGGTGCTGGTCCGGGTGGTTCTGGTGGTGGTGGTGCTCGTGGTGCTGAAGAAG
AACCGCCGCCGCCGCTGCAGGCTGTTCTGGTTGCTGACTCTTTCGACCGTCGTTTCTT
CCCGATCTCTAAAGACCAGCCGCGTGTTCTGCTGCCGCTGGCTAACGTTGCTCTGAT
CGACTACACCCTGGAGTTCCTGACCGCTACCGGTGTTCAGGAAACCTTCGTTTTCTG
CTGCTGGAAAGCTGCTCAGATCAAAGAACACCTGCTGAAATCTAAATGGTGCCGTCC
GACCTCTCTGAACGTTGTTCGTATCATCACCTCTGAACTGTACCGTTCTCTGGGTGAC
GTTCTGCGTGACGTTGACGCTAAAGCTCTGGTTCGTTCTGACTTCCTGCTGGTTTACG
GTGACGTTATCTCTAACATCAACATCACCCGTGCTCTGGAAGAACACCGTCTGCGTC
GTAAACTGGAAAAAAACGTTTCTGTTATGACCATGATCTTCAAAGAATCTTCTCCGT
CTCACCCGACCCGTTGCCACGAAGACAACGTTGTTGTTGCTGTTGACTCTACCACCA
ACCGTGTTCTGCACTTCCAGAAAACCCAGGGTCTGCGTCGTTTCGCTTTCCCGCTGTC
TCTGTTCCAGGGTTCTTCTGACGGTGTTGAAGTTCGTTACGACCTGCTGGACTGCCAC
ATCTCTATCTGCTCTCCGCAGGTTGCTCAGCTGTTCACCGACAACTTCGACTACCAG
ACCCGTGACGACTTCGTTCGTGGTCTGCTGGTTAACGAAGAAATCCTGGGTAACCAG
ATCCACATGCACGTTACCGCTAAAGAATACGGTGCTCGTGTTTCTAACCTGCACATG
TACTCTGCTGTTTGCGCTGACGTTATCCGTCGTTGGGTTTACCCGCTGACCCCGGAAG
CTAACTTCACCGACTCTACCACCCAGTCTTGCACCCACTCTCGTCACAACATCTACC
GTGGTCCGGAAGTTTCTCTGGGTCACGGTTCTATCCTGGAAGAAAACGTTCTGCTGG
GTTCTGGTACCGTT

>heIF2B5_epsilon2_codonopt | overlap

CTGCTGGGTTCTGGTACCGTTATCGGTTCTAACTGCTTCATCACCAACTCTGTTA
TCGGTCCGGGTTGCCACATCGGTGACAACGTTGTTCTGGACCAGACCTACCTGTGGC
AGGGTGTTCGTGTTGCTGCTGGTGCTCAGATCCACCAGTCTCTGCTGTGCGACAACG
CTGAAGTTAAAGAACGTGTTACCCTGAAACCGCGTTCTGTTCTGACCTCTCAGGTTG
TTGTTGGTCCGAACATCACCCTGCCGGAAGGTTCTGTTATCTCTCTGCACCCGCCGG
ACGCTGAAGAAGACGAAGACGACGGTGAGTTCTCTGACGACTCTGGTGCTGACCAG
GAAAAAGACAAAGTTAAAATGAAAGGTTACAACCCGGCTGAAGTTGGTGCTGCTGG
TAAAGGTTACCTGTGGAAAGCTGCTGGTATGAACATGGAAGAAGAAGAAGAACTGC
AGCAGAACCTGTGGGGTCTGAAAATCAACATGGAAGAAGAATCTGAATCTGAATCT
GAACAGTCTATGGACTCTGAAGAACCGGACTCTCGTGGTGGTTCTCCGCAGATGGAC
GACATCAAAGTTTTCCAGAACGAAGTTCTGGGTACCCTGCAGCGTGGTAAAGAAGA
AAACATCTCTTGCGACAACCTGGTTCTGGAAATCAACTCTCTGAAATACGCTTACAA
CGTTTCTCTGAAAGAAGTTATGCAGGTTCTGTCTCACGTTGTTCTGGAGTTCCCGCTG
CAGCAGATGGACTCTCCGCTGGACTCTTCTCGTTACTGCGCTCTGCTGCTGCCGCTGC
TGAAAGCTTGGTCTCCGGTTTTCCGTAACTACATCAAACGTGCTGCTGACCACCTGG
AAGCTCTGGCTGCTATCGAAGACTTCTTCCTGGAACACGAAGCTCTGGGTATCTCTA

TGGCTAAAGTTCTGATGGCTTTCTACCAGCTGGAAATCCTGGCTGAAGAAACCATCC
TGTCTTGGTTCTCTCAGCGTGACACCACCGACAAAGGTCAGCAGCTGCGTAAAAACC
AGCAGCTGCAGCGTTTCATCCAGTGGCTGAAAGAAGCTGAAGAAGAATCTTCTGAA
GACGACTAA

ACKNOWLEDGEMENTS

We thank Jirka Peschek, Elif Karagöz, Robert Stroud, James Fraser, Geeta Narlikar, Ron Vale, Axel Brilot, Nicole Schirle Oakdale, Nathaniel Talledge, Pearl Tsai, Ni Mu, Joseph Choe, Christopher Upjohn, Matt Jacobson, Chakrapani Kalyanaraman, and the Walter and Frost labs for reagents, technical advice and helpful discussions. We thank Michael Braunfeld, David Bulkley, and Alexander Myasnikov of the UCSF Center for Advanced CryoEM and Daniel Toso and Paul Tobias of the Berkeley Bay Area CryoEM Facility, which are supported by in part from NIH grants S10OD020054 and 1S10OD021741 and the Howard Hughes Medical Institute (HHMI). We also thank Zhiheng Yu, Rick Huang, and Chuan Hong of the CryoEM Facility at the Janelia Research Campus of the HHMI. We thank the QB3 shared cluster and NIH grant 1S10OD021596-01 for computational support. The Titan X Pascal used for this research was donated by the NVIDIA Corporation. **Funding:** This work was supported by funding to AF from a Faculty Scholar grant from the HHMI, the Searle Scholars Program, and NIH grant 1DP2GM110772-01, and by funding to PW from Calico Life Sciences LLC, the Rogers Family Foundation, the Weill Foundation, and the HHMI. AF is a Chan Zuckerberg Biohub Investigator, and PW is an Investigator of the HHMI. **Author Contributions:** JCT, LMV, AAA, ARR, AF, PW: Conception & design, analysis and interpretation of data. JCT, LMV, AAA, PJ, HCN: Acquisition of data. JCT, LMV, AAA, AF, PW: Writing – original draft preparation. JCT, LMV, AAA, PJ, HCN, ARR, AF, PW: Writing – review & editing**. Competing Interests:** PW and ARR are inventors on US Patent 9708247 held by the Regents of the University of California that describes ISRIB and its analogs. Rights to the invention have been licensed by UCSF to Calico. **Accession Numbers:** Accession numbers for the human eIF2B structures determined with FREALIGN, cryoSPARC, and RELION, respectively, are as follows: EMD-7442, EMD-

7443, EMD-7444 (density maps; Electron Microscopy Data Bank) and 6CAJ (coordinates of atomic models; Protein Data Bank). **Data availability:** All data needed to evaluate the conclusions in the paper are present in the paper and/or the Supplementary Materials, and the structural data is available in public databases. All of the raw cryoEM particle images are available upon request. We thank Graham Pavitt for the GP6452 yeast strain used in the purification of eIF2 which is available under a material transfer agreement with The University of Manchester.

REFERENCES

1. R. P. Dalton, D. B. Lyons, S. Lomvardas, Co-Opting the Unfolded Protein Response to Elicit Olfactory Receptor Feedback. *CELL*. **155**, 321–332 (2013).
2. M. Costa-Mattioli *et al.*, Translational control of hippocampal synaptic plasticity and memory by the eIF2α kinase GCN2. *Nature*. **436**, 1166–1173 (2005).
3. D. H. Munn *et al.*, GCN2 kinase in T cells mediates proliferative arrest and anergy induction in response to indoleamine 2,3-dioxygenase. *Immunity*. **22**, 633–642 (2005).
4. N. C. Wortham, M. Martinez, Y. Gordiyenko, C. V. Robinson, C. G. Proud, Analysis of the subunit organization of the eIF2B complex reveals new insights into its structure and regulation. *The FASEB Journal*. **28**, 2225–2237 (2014).
5. Y. Gordiyenko *et al.*, eIF2B is a decameric guanine nucleotide exchange factor with a γ2ε2 tetrameric core. *Nat Commun*. **5**, 3902 (2014).
6. A. M. Bogorad *et al.*, Insights into the Architecture of the eIF2Bα/β/δ Regulatory Subcomplex. *Biochemistry*, 140520123219000 (2014).
7. B. Kuhle, N. K. Eulig, R. Ficner, Architecture of the eIF2B regulatory subcomplex and its implications for the regulation of guanine nucleotide exchange on eIF2. *Nucleic Acids Research*. **43**, 9994–10014 (2015).
8. K. Kashiwagi *et al.*, Crystal structure of eukaryotic translation initiation factor 2B. *Nature*. **531**, 122–125 (2016).
9. E. Gomez, S. S. Mohammad, G. D. Pavitt, Characterization of the minimal catalytic domain within eIF2B: the guanine-nucleotide exchange factor for translation initiation. *EMBO J.* **21**, 5292–5301 (2002).
10. W. M. Yang, A. G. Hinnebusch, Identification of a regulatory subcomplex in the guanine

nucleotide exchange factor eIF2B that mediates inhibition by phosphorylated eIF2. *Molecular and Cellular Biology*. **16**, 6603–6616 (1996).

11. G. D. Pavitt, K. Ramaiah, S. R. Kimball, A. G. Hinnebusch, eIF2 independently binds two distinct eIF2B subcomplexes that catalyze and regulate guanine-nucleotide exchange. *Genes & Development*. **12**, 514–526 (1998).
12. T. Krishnamoorthy, G. D. Pavitt, F. Zhang, T. E. Dever, A. G. Hinnebusch, Tight binding of the phosphorylated alpha subunit of initiation factor 2 (eIF2alpha) to the regulatory subunits of guanine nucleotide exchange factor eIF2B is required for inhibition of translation initiation. *Molecular and Cellular Biology*. **21**, 5018–5030 (2001).
13. A. G. Hinnebusch, J. R. Lorsch, The Mechanism of Eukaryotic Translation Initiation: New Insights and Challenges. *Cold Spring Harbor Perspectives in Biology*. **4**, a011544–a011544 (2012).
14. A. G. Hinnebusch, The scanning mechanism of eukaryotic translation initiation. *Annu. Rev. Biochem.* **83**, 779–812 (2014).
15. H. P. Harding *et al.*, Regulated translation initiation controls stress-induced gene expression in mammalian cells. *Molecular Cell*. **6**, 1099–1108 (2000).
16. K. M. Vattem, R. C. Wek, Reinitiation involving upstream ORFs regulates ATF4 mRNA translation in mammalian cells. *Proc. Natl. Acad. Sci. U.S.A.* **101**, 11269–11274 (2004).
17. H. P. Harding *et al.*, An integrated stress response regulates amino acid metabolism and resistance to oxidative stress. *Molecular Cell*. **11**, 619–633 (2003).
18. C. Sidrauski *et al.*, Pharmacological brake-release of mRNA translation enhances cognitive memory. *eLife*. **2**, e00498–e00498 (2013).
19. C. Sidrauski, A. M. McGeachy, N. T. Ingolia, P. Walter, The small molecule ISRIB

reverses the effects of eIF2α phosphorylation on translation and stress granule assembly. *eLife*. **4** (2015), doi:10.7554/eLife.05033.

20. G. V. Di Prisco *et al.*, Translational control of mGluR-dependent long-term depression and object-place learning by eIF2α. *Nature Neuroscience*. **17**, 1073–1082 (2014).

21. H. P. Harding, D. Ron, in *Translational Control in Biology and Medicine*, M. B. Mathews, N. Sonenberg, J. W. B. Hershey, Eds. (Cold Spring Harbor, NY, 2007), pp. 345–368.

22. P. Remondelli, M. Renna, The Endoplasmic Reticulum Unfolded Protein Response in Neurodegenerative Disorders and Its Potential Therapeutic Significance. *Front Mol Neurosci*. **10**, 187 (2017).

23. J. Obacz *et al.*, Endoplasmic reticulum proteostasis in glioblastoma—From molecular mechanisms to therapeutic perspectives. *Sci. Signal.* **10**, eaal2323 (2017).

24. G. Martínez, C. Duran-Aniotz, F. Cabral-Miranda, J. P. Vivar, C. Hetz, Endoplasmic reticulum proteostasis impairment in aging. *Aging Cell*. **16**, 615–623 (2017).

25. P. A. J. Leegwater *et al.*, Subunits of the translation initiation factor eIF2B are mutant in leukoencephalopathy with vanishing white matter. *Nature Genetics*. **29**, 383–388 (2001).

26. M. Halliday *et al.*, Partial restoration of protein synthesis rates by the small molecule ISRIB prevents neurodegeneration without pancreatic toxicity. *Cell Death & Dis.* **6**, e1672–9 (2015).

27. A. Chou *et al.*, Inhibition of the integrated stress response reverses cognitive deficits after traumatic brain injury. *Proc. Natl. Acad. Sci. U.S.A.* **114**, E6420–E6426 (2017).

28. C. Sidrauski *et al.*, Pharmacological dimerization and activation of the exchange factor eIF2B antagonizes the integrated stress response. *Elife*. **4**, e07314 (2015).

29. Y. Sekine *et al.*, Mutations in a translation initiation factor identify the target of a

memory-enhancing compound. *Science*. **348**, aaa6986–1030 (2015).

30. R. A. de Almeida *et al.*, A Yeast Purification System for Human Translation Initiation Factors eIF2 and eIF2Bε and Their Use in the Diagnosis of CACH/VWM Disease. *PLoS ONE*. **8**, e53958–11 (2013).

31. A. G. Rowlands, R. Panniers, E. C. Henshaw, The catalytic mechanism of guanine nucleotide exchange factor action and competitive inhibition by phosphorylated eukaryotic initiation factor 2. *J. Biol. Chem.* **263**, 5526–5533 (1988).

32. D. D. Williams, N. T. Price, A. J. Loughlin, C. G. Proud, Characterization of the mammalian initiation factor eIF2B complex as a GDP dissociation stimulator protein. *J. Biol. Chem.* **276**, 24697–24703 (2001).

33. B. L. Craddock, C. G. Proud, The alpha-subunit of the mammalian guanine nucleotide-exchange factor eIF-2B is essential for catalytic activity in vitro. *Biochem. Biophys. Res. Commun.* **220**, 843–847 (1996).

34. B. R. Hearn *et al.*, Structure-Activity Studies of Bis-O-Arylglycolamides: Inhibitors of the Integrated Stress Response. *ChemMedChem*. **11**, 870–880 (2016).

35. S. Q. Zheng *et al.*, MotionCor2: anisotropic correction of beam-induced motion for improved cryo-electron microscopy. *Nat Meth*. **14**, 331–332 (2017).

36. K. Zhang, Gctf: Real-time CTF determination and correction. *J. Struct. Biol.* **193**, 1–12 (2016).

37. D. Kimanius, B. O. Forsberg, S. H. Scheres, E. Lindahl, Accelerated cryo-EM structure determination with parallelisation using GPUs in RELION-2. *Elife*. **5**, e18722 (2016).

38. A. Punjani, J. L. Rubinstein, D. J. Fleet, M. A. Brubaker, cryoSPARC: algorithms for rapid unsupervised cryo-EM structure determination. *Nat Meth*. **14**, 290–296 (2017).

39. N. Grigorieff, Frealign: An Exploratory Tool for Single-Particle Cryo-EM. *Meth. Enzymol.* **579**, 191–226 (2016).

40. E. F. Pettersen *et al.*, UCSF Chimera--a visualization system for exploratory research and analysis. *J Comput Chem*. **25**, 1605–1612 (2004).

41. L. A. Kelley, S. Mezulis, C. M. Yates, M. N. Wass, M. J. E. Sternberg, The Phyre2 web portal for protein modeling, prediction and analysis. *Nat Protoc*. **10**, 845–858 (2015).

42. T. B. Hiyama, T. Ito, H. Imataka, S. Yokoyama, Crystal Structure of the α Subunit of Human Translation Initiation Factor 2B. *Journal of Molecular Biology*. **392**, 937–951 (2009).

43. N. W. Moriarty, R. W. Grosse-Kunstleve, P. D. Adams, electronic Ligand Builder and Optimization Workbench (eLBOW): a tool for ligand coordinate and restraint generation. *Acta Crystallogr. D Biol. Crystallogr.* **65**, 1074–1080 (2009).

44. P. Emsley, B. Lohkamp, W. G. Scott, K. Cowtan, Features and development of Coot. *Acta Crystallogr. D Biol. Crystallogr.* **66**, 486–501 (2010).

45. P. D. Adams *et al.*, PHENIX: a comprehensive Python-based system for macromolecular structure solution. *Acta Crystallogr. D Biol. Crystallogr.* **66**, 213–221 (2010).

46. V. B. Chen *et al.*, MolProbity: all-atom structure validation for macromolecular crystallography. *Acta Crystallogr. D Biol. Crystallogr.* **66**, 12–21 (2010).

47. S. J. Ludtke, Single-Particle Refinement and Variability Analysis in EMAN2.1. *Meth. Enzymol.* **579**, 159–189 (2016).

48. P. Schuck, Size-distribution analysis of macromolecules by sedimentation velocity ultracentrifugation and Lamm equation modeling. *Biophys. J.* **78**, 1606–1619 (2000).

49. A. F. Zyryanova *et al.*, Binding of the integrated stress response inhibitor, ISRIB, reveals

a regulatory site in the nucleotide exchange factor, eIF2B. *bioRxiv*. 224824 (2017).

Chapter 2

Structural basis of eIF2B-catalyzed GDP exchange and phosphoregulation by the integrated stress response

Structural basis of eIF2B-catalyzed GDP exchange and phosphoregulation by the integrated stress response

Aditya A. Anand[1,2†], Lillian R. Kenner[1†], Henry C. Nguyen[1], Alexander G. Myasnikov[1], Carolin J. Klose[1,2], Lea A. McGeever[1,2], Jordan C. Tsai[1,2], Lakshmi E. Miller-Vedam[1], Peter Walter[1,2,*], Adam Frost[1,3,*]

Affiliations:

[1] Department of Biochemistry and Biophysics, University of California at San Francisco, San Francisco, CA, USA

[2] Howard Hughes Medical Institute

[3] Chan Zuckerberg Biohub, San Francisco, CA, USA

*Correspondence to: PW: peter@walterlab.ucsf.edu; AF: adam.frost@ucsf.edu

†These authors contributed equally. In the spirit of equal contribution, the order of first authors has been switched in pre-print and print.

This work was first submitted to bioRxiv as a preprint at doi.org/10.1101/504654

ABSTRACT

The integrated stress response (ISR) tunes the rate of protein synthesis. Control is exerted by phosphorylation of the general translation initiation factor eIF2. eIF2 is a GTPase, that becomes activated by eIF2B, a two-fold symmetric and heterodecameric complex that functions as eIF2's dedicated nucleotide exchange factor. Phosphorylation converts eIF2 from a substrate into an inhibitor of eIF2B. We report cryoEM structures of eIF2 bound to eIF2B in the dephosphorylated state. The structures reveal that the eIF2B decamer is a static platform upon which one or two flexible eIF2 trimers bind and align with eIF2B's bipartite catalytic centers to catalyze nucleotide exchange. Phosphorylation refolds eIF2α, allowing it to contact eIF2B at a different interface and, we surmise, thereby sequesters it into a non-productive complex.

INTRODUCTION

Numerous factors regulate translation of the genetic code into proteins, including eukaryotic translation initiation factor 2 (eIF2), a GTPase composed of α, β, and γ subunits. During initiation, eIF2 binds $tRNA^{Met}$ and GTP to form a ternary complex that scans mRNAs for start codons. Following start codon detection, eIF2γ hydrolyzes its GTP and translation initiates. For eIF2 reactivation, GDP is replaced by GTP upon catalysis by a dedicated guanine nucleotide exchange factor (GEF), eIF2B.

eIF2 and eIF2B control translation initiation. Stress-responsive kinases phosphorylate eIF2α at conserved Ser51, transforming eIF2 from substrate into a competitive GEF inhibitor. Phosphoregulation of eIF2 is known as the integrated stress response (ISR)(*1*). Once activated, the ISR reduces overall protein synthesis, while enhancing translation of a small subset of mRNAs in response to cellular threats, including protein misfolding, infection, inflammation, and starvation(*1–3*).

eIF2B comprises two copies each of an α, β, γ, δ, and ε subunit that assemble into a two-fold symmetric heterodecamer(*4*,*5*). The eIF2Bε subunit contains the enzyme's catalytic center and associates closely with eIF2Bγ. Two copies each of the eIF2Bβ and δ subunits form the complex's core, bridged by two eIF2Bα subunits across the symmetry interface(*4*,*6*). Genetic and biochemical studies identified residues responsible for eIF2B's catalytic activity and suggested how eIF2 binding to eIF2B may differ following eIF2α-S51 phosphorylation(*4*,*7–10*). Yet, how eIF2 recognizes eIF2B and how eIF2B catalyzes nucleotide exchange remained unknown, as did the transformation of eIF2 from a substrate to high-affinity inhibitor of eIF2B following its phosphorylation.

A potent small-molecule, drug-like inhibitor of the integrated stress response, ISRIB, allays the effects of eIF2α phosphorylation by activating eIF2B(*11–13*). Upon adding ISRIB, cells undergoing the ISR resume translation(*12*,*13*). When administered to rodents, ISRIB enhances cognition and ameliorates cognitive deficits caused by traumatic brain injury(*14*) and prion-induced neurodegeneration(*15*). Furthermore, eIF2B activation rescues cognitive and motor function in mouse models of leukoencephalopathy with vanishing white matter disease (VWMD), a fatal familial disorder associated with mutations spread over all eIF2B subunits(*16*).
ISRIB bridges the symmetric interface of two eIF2B subcomplexes to enhance the formation of the decameric eIF2B holoenzyme(*17*,*18*), enhancing available GEF activity by promoting higher-order assembly of the eIF2B decamer. However, it has remained enigmatic why decameric eIF2B would be more active than its unassembled subcomplexes. To explore this question, we determined structures of eIF2B bound with both its substrate, eIF2α,β,γ, and inhibitor, eIF2α•P.

RESULTS

We co-expressed all five subunits of human eIF2B in *E. coli* and all three subunits of human eIF2 in *S. cerevisiae* (Figure 2.S1A-B). The yeast expression strain lacked *GCN2*, the eIF2 kinase, to ensure expression of homogenously non-phosphorylated eIF2(*19*). We incubated ISRIB and purified eIF2 at concentrations near the Michaelis constant of the nucleotide exchange reaction (K_m = ~1.5μM,(*17*)) and added an inter-amine crosslinker to stabilize complexes before sample vitrification and cryoEM analysis (Figure 2.S2A-C). We resolved two structures: eIF2B bound asymmetrically to a single eIF2 trimer and eIF2B bound symmetrically to two eIF2 trimers (Figures 1.1A-F, 1.S3A,1.S4-5, Table 1.S1-1.S3).

Snaking across the surface of eIF2B, we observed density consistent in size and shape with eIF2 subunits and the previously unresolved eIF2Bε HEAT domain. Comparison with homologous structures of eIF2α and eIF2γ revealed that the assembled eIF2•eIF2B complex retained similarity to the structures of these individually analyzed domains (*20*, *21*)(Figure 2.2,Figure 2.S6). We only resolved a single helix of eIF2β (Figure 2.1A,D,Figure 2.2A), consistent with other studies(*20*,*21*). In both reconstructions, all five subunits of eIF2B can be superimposed on previously determined structures lacking eIF2 (RMSD of ~0.6Å)(*17*). Thus, eIF2B retained its overall arrangement when bound to one or two eIF2s (Figure 2.1A-F), indicating that eIF2 binds via equivalent modes to both sides of a static eIF2B scaffold with no allostery in eIF2B upon eIF2 engagement. This is consistent with non-cooperative kinetics reported for nucleotide exchange by eIF2B decamers(*17*).

Bound to eIF2B, eIF2 adopted an extended 150Å conformation (Figures 2.1-2.2) with eIF2's central nucleotide-binding γ-subunit flanked by its α- and β-subunits at its opposing ends. eIF2γ contains classical GTP-binding motifs, including the nucleobase-binding G4 motif, the

phosphate-binding P-loop, and switch helices 1 and 2. eIF2B recognizes eIF2 via coincident binding of both eIF2α and eIF2γ. Binding to both eIF2 subunits involves bipartite elements of eIF2B(Figures 1.1,1.2A-C).

First, bipartite recognition of eIF2γ involves two domains of eIF2Bε that function together to splay open the nucleotide-binding site. Our nucleotide-free cryoEM model is similar to the γ-subunit of GTP-bound aIF2 from *S.solfataricus*(*24*) (Figure 2.2D-E, average RMSD ~2.3Å). Yet, surrounding the GTP binding pocket, the structures diverged considerably with the P-loop in eIF2B•eIF2 partially occluding the nucleotide-binding site (RMSD of ~12Å). Prior work implicated the HEAT domain in catalysis(*23*,*24*). In agreement, eIF2γ interacts with the HEAT domain, including a partially hydrophobic surface that includes eIF2Bε Y583(Figure 2.2C). On the opposing side of the nucleotide-binding pocket, the central core of eIF2Bε engaged with an open loop conformation of Switch 1. This change appears due to electrostatic interactions between eIF2γ R75 in Switch 1 and Q258 and D262 in eIF2Bε. Thus, both eIF2Bε's HEAT domain and core collaborate to open the nucleotide-binding site (Figure 2.2B-D).

The second example of bipartite recognition concerns eIF2α binding in the cleft between eIF2Bβ and eIF2Bδ' (δ' indicates the δ-subunit from the opposing tetramer, Figures 2.1-2.3). Notably, this binding site only exists when two tetramers of eIF2B(βγδε) associate to form the symmetry interface in octameric eIF2B$(\beta\gamma\delta\varepsilon)_2$. eIF2α contains two structured domains separated by a flexible linker(Figure 2.1-2,S6). The N-terminus consists of an OB-fold, common in tRNA-binding proteins(*20*). The OB-fold is further elaborated with a positively-charged loop (the S-loop), while the C-terminal αβ-fold connects eIF2α to eIF2γ. The S-loop harbors S51 and is responsible for all of the resolvable contacts between eIF2α and eIF2B's β subunit (Figure 2.3A). Prior work implicated a conserved 'K^{79}GYID^{83}' motif in eIF2α as being important for eIF2B

binding(*10*). Of note, an interaction between Y81 was well-resolved adjacent to the equally prominent R250 on eIF2Bδ' (Figure 2.3B). When we mutated R250 to either alanine or glutamate, neither mutation affected the residual GEF activity displayed by dissociated tetramers (Figure 2.3D;R250A k_{obs}=0.013min^{-1},R250E k_{obs}=0.023min^{-1},wild-type k_{obs}=0.016min^{-1}), while both mutants diminished the GEF activity of the ISRIB-stabilized eIF2B octamer when compared to wild-type (Figure 1.3E;R250A k_{obs}=0.012min^{-1},R250E k_{obs}=0.017min^{-1},wild-type k_{obs}=0.063min^{-1}). This is consistent with the notion that unphosphorylated eIF2α interacts with the *trans*-tetramer only upon assembly of octameric or decameric eIF2B across its symmetry interface.

On the *cis*-tetramer, eIF2α's positively-charged S-loop binds negatively charged and polar residues along the exposed surface of eIF2Bβ. This binding site is consistent with yeast studies suggesting that mutations in this site compromise eIF2 binding(*7*). Examination of the structure identified a potential hydrogen bond between eIF2Bβ N132 and eIF2α R52 (Figure 2.3C). We substituted N132 with aspartate, anticipating that the introduced charge complementarity would enhance binding to eIF2α R52. When compared to wild-type eIF2B tetramers, eIF2B-βN132D tetramers and ISRIB-stabilized octamers indeed proved to be gain-of-function mutations, exhibiting ~two-fold enhanced GEF activity (Figs.3F-G,S1D, eIF2B(βγδε) βN132D k_{obs}=0.044 min^{-1}, eIF2B$(\beta\gamma\delta\varepsilon)_2$ βN132D k_{obs}=0.169 min^{-1}). This is consistent with eIF2B tetramers possessing reduced activity when compared to assembled octameric or decameric holo-eIF2B. eIF2α binding in the cleft between tetramers further supports the notion that ISRIB enhances eIF2B's GEF activity by promoting higher-order assembly.

To understand how eIF2α phosphorylation on S51 transforms eIF2 from substrate to inhibitor, we co-expressed the isolated eIF2α subunit in *E.coli* with the kinase domain of PERK (Figure

2.S1C). We incubated pre-assembled eIF2B decamers with an excess of eIF2α-P, followed by crosslinking and vitrification. Reconstruction of the eIF2B decamer adorned with a two copies of eIF2α-P (Figs.4A,S7-S8,Tables 1.S1-1.S3), revealed eIF2α-P bridging the interface between eIF2Bδ and eIF2Bα(Figure 2.4A). Intriguingly, we observed no overlap between the binding sites of non-phosphorylated eIF2α described above and eIF2α-P (Figure 2.4B-C).

Density for both eIF2α S51-P and two arginines positioned ~4Å away, eIF2α R53 and R63, were well-resolved and suggestive of an electrostatic coordination responsible for phosphorylation-induced refolding of the S-loop (Movie 2.S1,Figure 2.4F-G), as initially observed by Kashiwagi, et al. The phosphorylation-induced rearrangement also positions hydrophobic residues on eIF2α for potential interactions with hydrophobic residues on eIF2B (including eIF2α I55, I58, and L61 and eIF2Bδ L314, A315, A318, and F322).

This structural model agrees with analyses in yeast and mammalian systems. First, eIF2Bα is dispensable for viability in yeast, yet eIF2Bα deletion impairs phospho-inhibition of eIF2B, consistent with the subunit's role in binding eIF2α-P(*27*). Point mutations with identical phenotypes cluster at the interface between eIF2Bα and eIF2Bδ, e.g., eIF2Bα F239 and eIF2Bδ M506 and P508(*28*, *29*). Importantly, eIF2Bδ L314 complements the hydrophobic surface of the eIF2α S-loop that is exposed upon refolding, and mutation of the equivalent position in *S. cerevisiae*, L381Q, impairs the ISR in yeast(*28*). These data validate the phosphorylation-induced refolding and relocation of eIF2α-P observed here.

Our analyses reveal the mechanistic basis of eIF2B's nucleotide exchange activity and suggest how phosphorylation converts eIF2 from substrate to inhibitor. The non-phosphorylated form of eIF2 binds to a composite surface created only in the assembled decamer, allowing both the core

and the flexibly attached HEAT domain of eIF2Bε to engage its target in concert for enhanced GEF activity.

By contrast, eIF2α-P adopts a new conformation and suggests how the S-loop may become incompatible for binding to the site where nonphosphorylated eIF2α binds as a substrate (Movie 2.S1). Phosphorylation thus enables a distinct binding mode on the opposite side of eIF2B where eIF2α-P lies exiled at the interface of eIF2Bα and eIF2Bδ. In eIF2•P, the rearrangement of the S-loop derives from an intramolecular electrostatic interaction between R63 and R53 and the phosphate, which also exposes a hydrophobic surface upon phosphorylation-induced refolding. We surmise that this new binding mode is nonproductive for nucleotide exchange on eIF2-P and sequesters the catalytic domains into an inhibited state that prevents the catalytic moieties of eIF2Bε from properly engaging in productive nucleotide exchange.

According to this view, the decameric core of eIF2B is a static scaffold. Control is exerted by regulation of its assembly state, which can be influenced by ISRIB and eIF2Bα_2. Additional control arises from binding of eIF2-P which binds as a competitive inhibitor but to a non-overlapping binding site for the alpha subunit. We note that eIF2-P inhibitor binding requires the presence of eIF2Bα_2 with which it interacts directly, whereas eIF2 substrate binding does not, as it can occur with the octamer. Atomic models of ISRIB-stabilized eIF2B bound to eIF2 reconcile numerous structure-activity relationships and are consistent with both loss- and gain-of-function mutations described here and previously. Together, the structures provide an intuitive view of how holoenzyme assembly activates nucleotide exchange as well as provides opportunities for regulation (Figure 1.5). Both the substrate eIF2α subunit, the regulatory eIF2Bα_2 subunit, and ISRIB stabilize the two-fold symmetric and fully active decameric form of eIF2B by “stapling”

the constituents together. By bridging between eIF2Bα and eIF2Bδ at its binding site, eIF2-P is likewise predicted to stabilize the eIF2B decamer, albeit now holding it in an inactive state. These structures also deepen our understanding of ISRIB's ability to ameliorate the inhibitory effects of eIF2α phosphorylation on ternary complex formation. ISRIB staples tetrameric building blocks together into an octamer, enhancing GEF activity three-fold, thus favoring association of the eIF2Bα_2 homodimer. The summed effect of these sequential steps is a an order of magnitude activity enhancement (*20*). Thus, the surplus of GEF activity provided by ISRIB-driven holoenzyme assembly will counteract inhibition of eIF2B by limiting amounts of eIF2-P. By contrast, under conditions where eIF2B decamer is maximally stabilized at saturating concentrations of eIF2-P, ISRIB cannot promote any additional eIF2B decamer assembly. This mechanism explains ISRIB's bell-shaped response profile to increasing stress (*19*), and its ability to mitigate the effects of eIF2 phosphorylation within a certain eIF2-P concentration range.

Figure 2.1

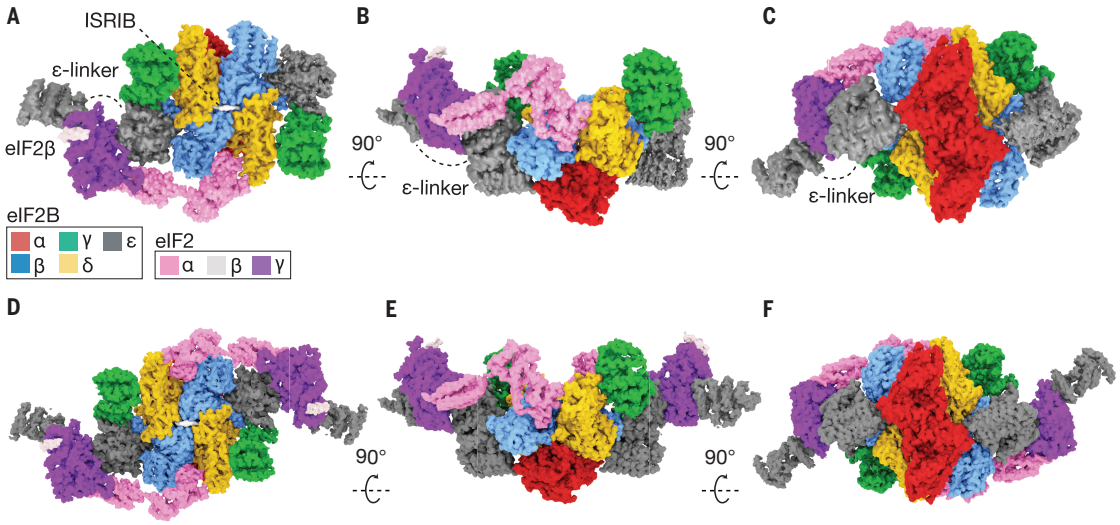

eIF2B heterodecamer bound to one or two eIF2 heterotrimers. (A-C) Orthogonal views of a single versus (D-E) a pair of elongated eIF2 heterotrimers bound to ISRIB-stabilized eIF2B decamers. ISRIB density is rendered in white.

Figure 2.2

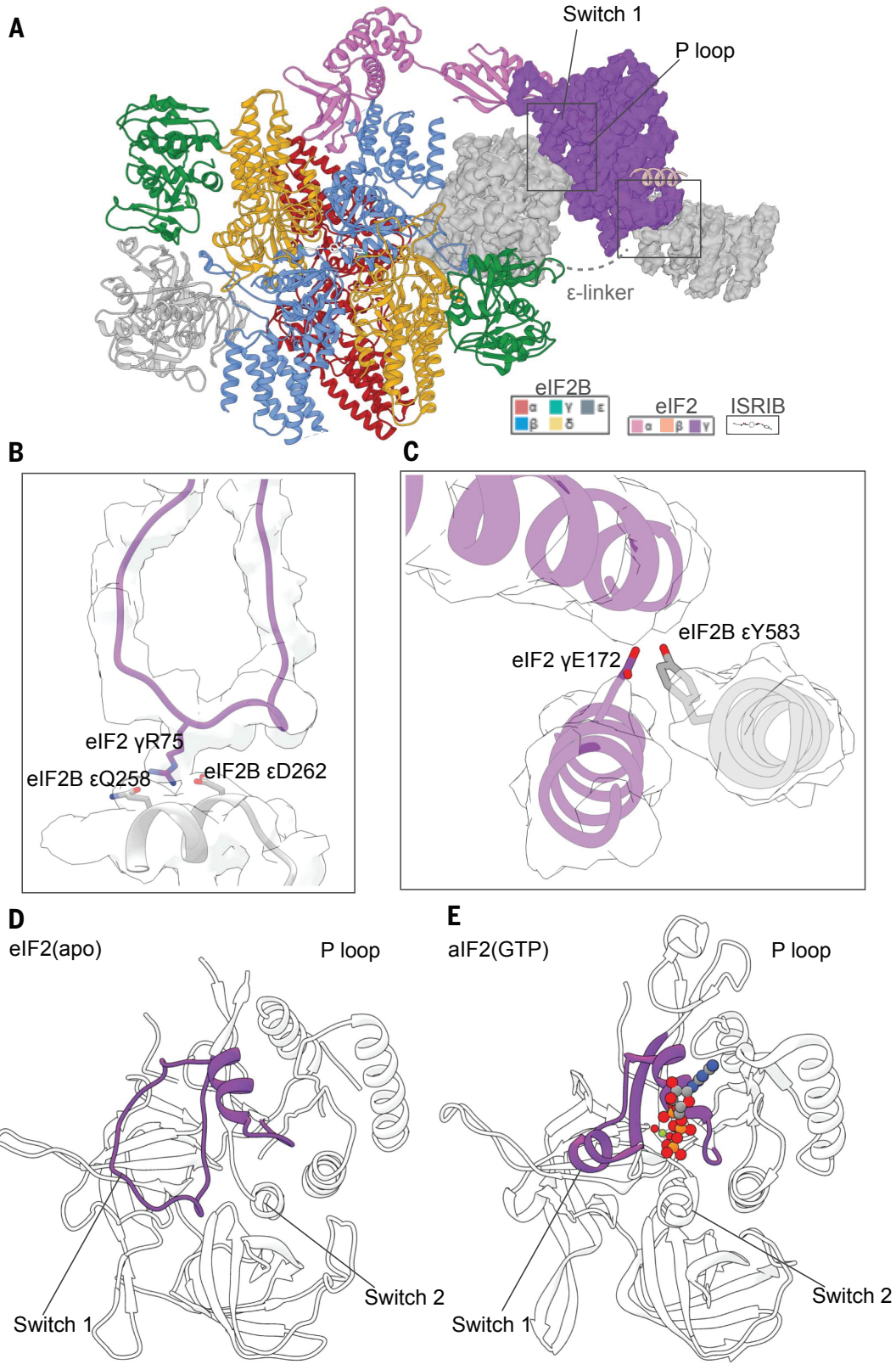
A
Switch 1
P loop
ε-linker
eIF2B
eIF2
ISRIB
B
eIF2 γR75
eIF2B εQ258
eIF2B εD262
C
eIF2B εY583
eIF2 γE172
D
eIF2(apo)
P loop
Switch 1
Switch 2
E
aIF2(GTP)
P loop
Switch 1
Switch 2

Figure 2.2

The bipartite basis of guanine nucleotide exchange by eIF2B. (A) Structural model of a single eIF2 heterotrimer bound to eIF2B decamer, emphasizing the cryoEM density for eIF2γ and its interactions with eIF2Bε. (B) Comparison of an aIF2 structure bound to GTP (PDB: 4RCY) and (C) GDP (PDB: 4RD6) with the open, nucleotide-free state of eIF2 (D) reported here.

Figure 2.3

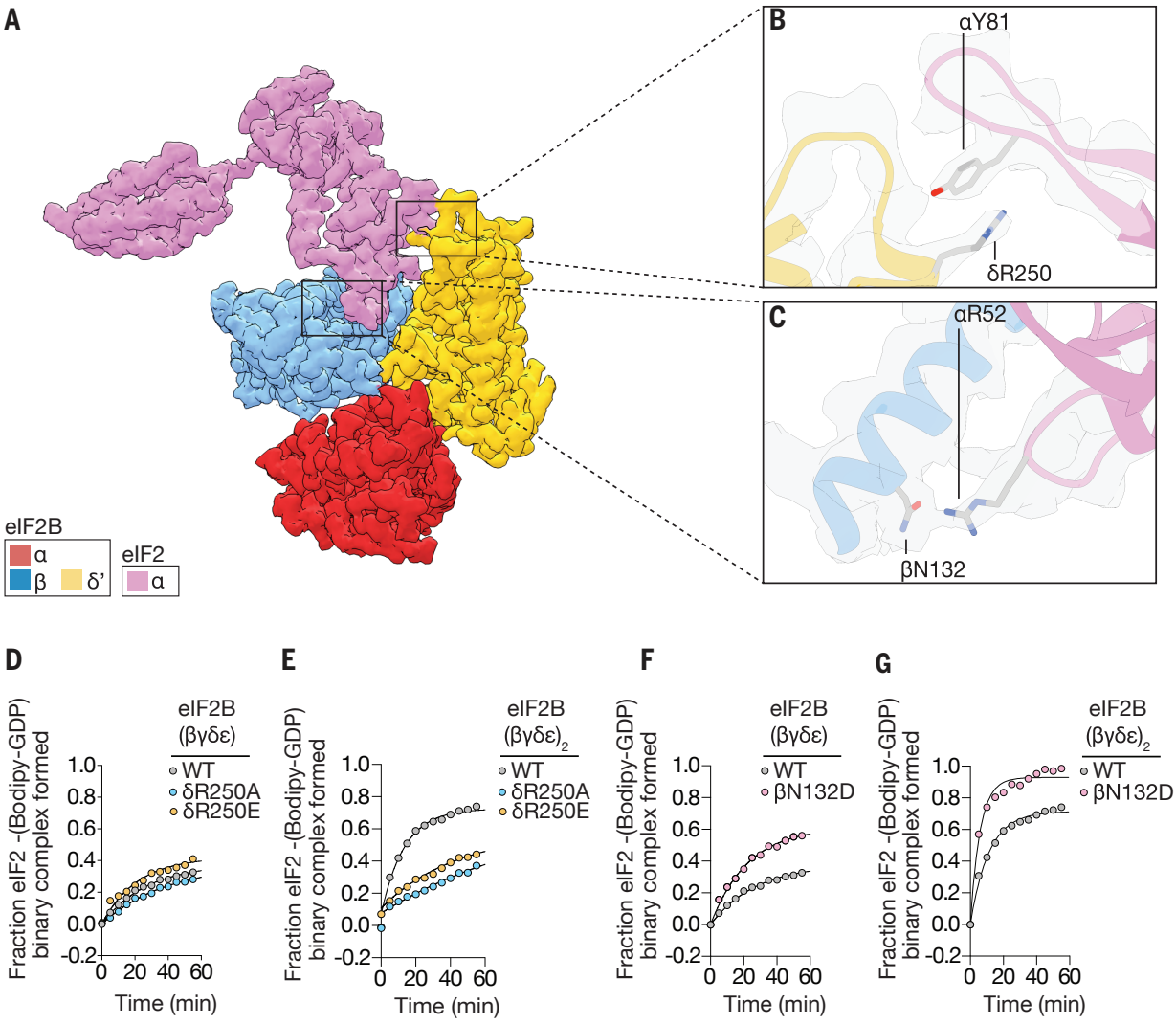

The bipartite basis of eIF2α recognition and assembly-stimulated activity. (A) cryoEM density for eIF2α bound to the regulatory subcomplex (α,β,δ or RSC) of eIF2B. (B) Density and zoom-in detail of a cation-π interaction between eIF2Bδ and eIF2α. (C) polar interactions between eIF2Bβ and the S-loop of eIF2α. (D,F) GEF activity of wildtype versus mutated eIF2B(βγδε) tetramers, and (E,G) ISRIB-stabilized eIF2B$(\beta\gamma\delta\varepsilon)_2$ octamers measured by loading of fluorescent GDP onto eIF2.

Figure 2.4

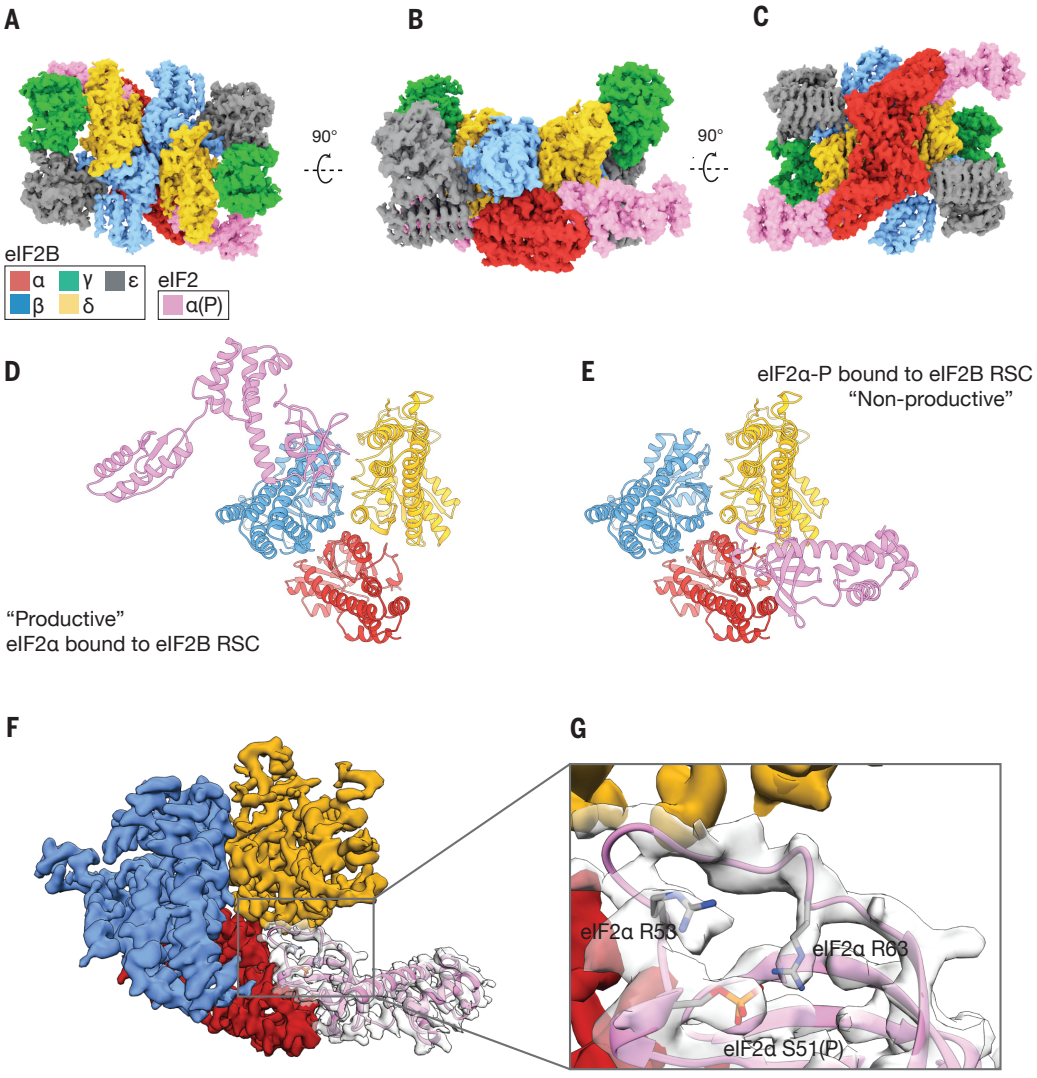

The structural basis of phosphoregulation by the ISR. (A-C) Orthogonal views of a pair of S51-phosphorylated eIF2α subunits bound to the eIF2B decamer. (D) Comparison of the productive binding mode of non-phosphorylated eIF2α, versus (E) the non-productive and non-overlapping binding mode of phosphorylated eIF2α. (F-G) CryoEM density and interpretation of the phosphorylated eIF2α binding mode and refolded conformation of the S-loop, placing the S51 phosphate moiety near eIF2α R53 and R63.

Figure 2.S1

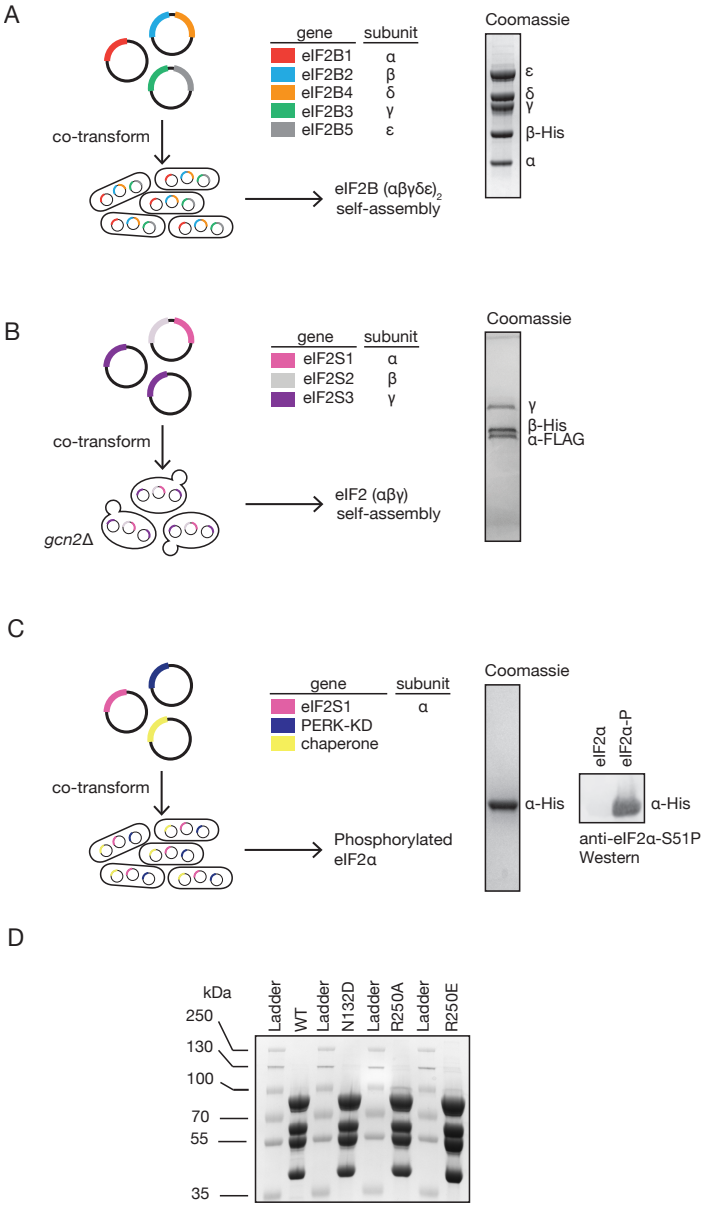

Purification of eIF2, eIF2α-P, eIF2B(αβγδε)$_2$, and mutant eIF2B(βγδε). (A) Recombinant *E. coli* expression system and SDS-PAGE analysis for human eIF2B(αβγδε)$_2$ as described in (*20*). (B) Recombinant *S. cerevisiae* expression system and SDS-PAGE analysis for human eIF2 as described in (*22*). (C) Recombinant expression *E. coli* system for phosphorylated eIF2α and SDS-PAGE and Western blot analysis as described in (*38*). This expression protocol was modified to include the chaperones GroEL, GroES and tig. (D) SDS-PAGE analysis of mutant eIF2B(βγδε).

Figure 2.S2

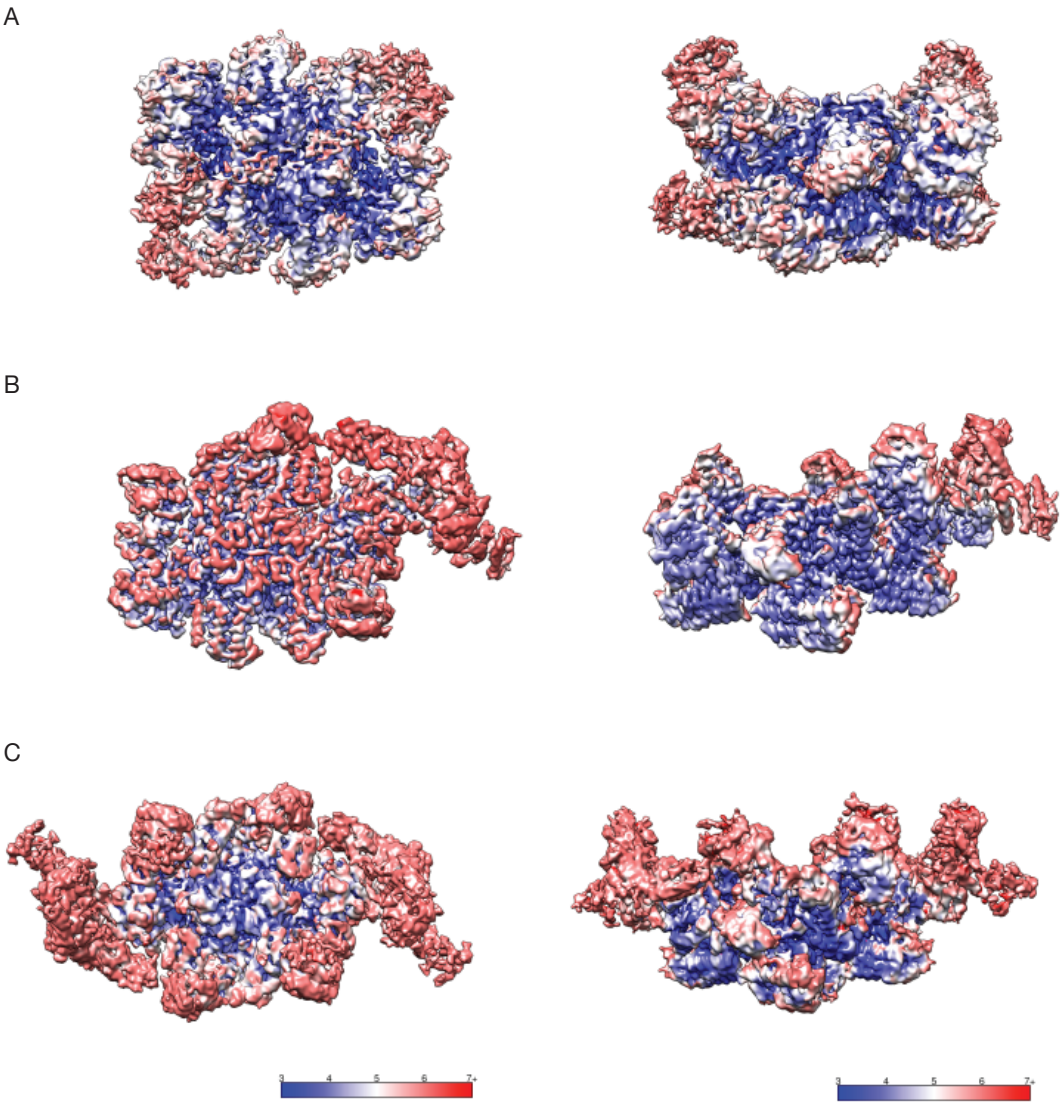

Local resolution estimates. (A) Local resolution estimates determined using cryoSPARC v0.6.5 and displayed using UCSF Chimera for eIF2α-P bound to eIF2B with C2 symmetry, (B) eIF2 bound to eIF2B with C1 symmetry and (C) two copies of eIF2 bound to eIF2B with C2 symmetry.

Figure 2.S3

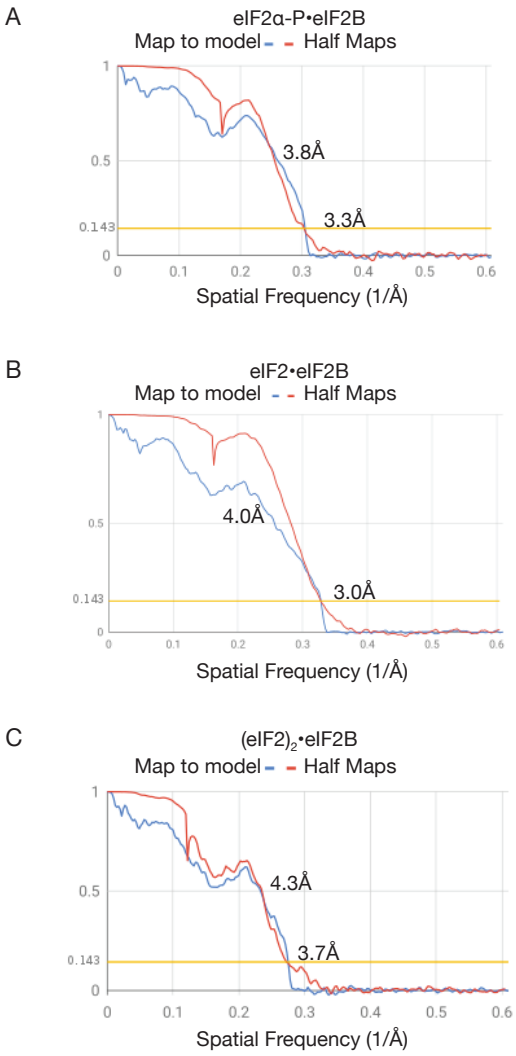

Fourier shell correlations. (A) eIF2α-P bound to eIF2B with C2 symmetry. Correlations between the independent half maps (red), and the final cryoEM density map versus simulated density maps for the atomic models (blue). (B) eIF2 bound to eIF2B with C1 symmetry, and (C) two copies of eIF2 bound to eIF2B with C2 symmetry**.**

Table 2.S1

Data collection parameters.

	eIF2 Alpha P bound to eIF2B	eIF2 bound to eIF2B and Two eIF2 bound to eIF2B
Pixel Size (Å)	0.822	0.822
Defocus Range	0.5 - 1.5	0.5 - 1.5
Voltage (kV)	300	300
Magnification	29,000	29,000
Spherical Aberration (mm)	2.7	2.7
Detector	K2 Summit	K2 Summit
Detector Pixel Size	5	5
Per frame electron dose (e-/Å2)	0.8	0.85
# of Frames	100	80
Frame Length (seconds)	0.1	0.1
Micrographs	3233	3947
Exposure (seconds)	10	8

Table 2.S2

Refinement parameters.

	eIF2 Alpha P bound to eIF2B	eIF2 bound to eIF2B	Two eIF2 bound to eIF2B
Particles	22165	44157	7,473
FSC Average Resolution, unmasked (Å)	3.48	3.15	3.78
FSC Average Resolution, masked (Å)	3.27	3.04	3.65
Map Sharpening B-factor	-78.7	-71.3	-41.8

Table 2.S3

Modeling statistics.

	eIF2 Alpha P bound to eIF2B	eIF2 bound to eIF2B	Two eIF2 bound to eIF2B
Number of Atoms, macromolecules	25100	28495	33629
Number of Atoms, ligands	0	60	60
Molprobity Score	2.2	1.28	1.53
Clashscore, all atoms	6.61	1.86	4.27
Outlier Rotamers (%)	3.16	0.12	0.26
RMS (bonds)	0.012	0.003	0.003
RMS (angles)	1.215	0.804	0.742
Ramachandran Favored (%)	92.82	95.24	95.39
Ramachandran Outliers (%)	0	0	0
Ramachandran Allowed (%)	7.18	4.76	4.61

Movie 2.S1

Conformational morphing between the non-phosphorylated and S51-phosphorylated structures of eIF2α, highlighting how phosphorylation leads to refolding of the S-loop and the exposure of a hydrophobic surface.

Link to movie originally appeared in Science at

https://science.sciencemag.org/highwire/filestream/726274/field_highwire_adjunct_files/1/aaw2922s1.mov

MATERIALS AND METHODS

Purification of decameric eIF2B(αβγδε)2

As previously described (*20*), pJT066, pJT073, and pJT074 were co-transformed into One Shot BL21 Star (DE3) chemically competent E. coli cells (Invitrogen) and grown in Luria broth containing ampicillin, kanamycin, and chloramphenicol at 37°C on an orbital shaker. When the culture reached an OD600 of ~0.6, the temperature was reduced to 16°C, and the culture was induced with 0.8 mM IPTG (Gold Biotechnology) and grown for 16 hours. Cells were harvested and lysed with EmulsiFlex-C3 (Avestin) in a buffer containing 20 mM HEPES-KOH, pH 7.5, 250 mM KCl, 1 mM tris(2-carboxyethyl)phosphine (TCEP), 5 mM $MgCl_2$, 15 mM imidazole, and complete EDTA-free protease inhibitor cocktail (Roche). The lysate was clarified at 30,000g for 20 min at 4°C. Subsequent purification steps were conducted on the ÄKTA Pure (GE Healthcare) system at 4°C. The clarified lysate was loaded onto a HisTrap HP 5 ml, washed in binding buffer (20 mM HEPES-KOH, pH 7.5, 200 mM KCl, 1 mM TCEP, 5 mM $MgCl_2$, and 15 mM imidazole), and eluted with a linear gradient (75 ml) of 15 mM to 300 mM imidazole in the same buffer. The eIF2B fraction eluted from the HisTrap column at 80 mM imidazole. The eIF2B fraction was collected and loaded onto a 20 ml Mono Q HR16/10 column (GE Healthcare), washed in Buffer A (20 mM HEPES-KOH, pH 7.5, 200 mM KCl, 1 mM TCEP, and 5 mM $MgCl_2$) and eluted with a linear gradient (200 ml) of 200 mM to 500 mM KCl in the same buffer. The eIF2B fraction eluted off the Mono Q column at a conductivity of 46 mS/cm (corresponding to 390 mM KCl). Fractions were collected, concentrated with an Amicon Ultra-15 concentrator (EMD Millipore) with a 100,000-dalton molecular weight cutoff, and loaded onto a Superdex 200 10/300 GL column (GE Healthcare) equilibrated with Buffer A. A typical preparation yielded approximately 0.5 mg of eIF2B$(a\beta\gamma\delta\varepsilon)_2$ from a 1-liter culture.

Purification of heterotrimeric human eIF2

Human eIF2 was prepared from an established recombinant *S. cerevisiae* expression protocol (*22*). In brief, the yeast strain GP6452 (gift from the Pavitt lab, University of Manchester) containing yeast expression plasmids for human eIF2 subunits and a deletion of GCN2 encoding the only eIF2 kinase in yeast, was grown to saturation in synthetic complete media (Sunrise Science Products) with auxotrophic markers (-Trp, -Leu, -Ura) in 2% dextrose. The β and α subunits of eIF2 were tagged with His6 and FLAG epitopes, respectively. A 12-liter yeast culture was grown in rich expression media containing yeast extract, peptone, 2% galactose, and 0.2% dextrose. Cells were harvested and resuspended in lysis buffer [100 mM Tris, pH 8.5, 300 mM KCl, 5 mM $MgCl_2$, 0.1% NP-40, 5 mM imidazole, 10% glycerol (Thermo Fisher Scientific), 2 mM DTT, 1× protease inhibitor cocktail (Sigma Aldrich #11836170001), 1 μg/ml each aprotinin (Sigma Aldrich), leupeptin (Sigma Aldrich), pepstatin A (Sigma Aldrich). Cells were lysed in liquid nitrogen using a steel blender. The lysate was centrifuged at 10,000g for 1 hour at 4°C. Subsequent purification steps were conducted on the ÄKTA Pure (GE Healthcare) system at 4°C. Lysate was applied to a 5-ml HisTrap Crude column (Thermo Fisher Scientific) equilibrated in buffer (100 mM HEPES, pH 7.5, 100 mM KCl, 5 mM $MgCl_2$, 0.1% NP-40, 5% glycerol, 1 mM dithiothreitol, 0.5× protease inhibitor cocktail, 1 μg/ml each aprotinin, leupeptin, pepstatin A). eIF2 bound to the column, was washed with equilibration buffer and eluted using a 50 ml linear gradient of 5 mM to 500 mM imidazole. Eluted eIF2 was incubated with FLAG M2 magnetic affinity beads, washed with FLAG wash buffer (100 mM HEPES, pH 7.5, 100 mM KCl, 5 mM $MgCl_2$, 0.1% NP-40, 5% glycerol, 1 mM TCEP, 1× protease inhibitor cocktail, 1 μg/ml each aprotinin, leupeptin, pepstatin A) and eluted with FLAG elution buffer [identical to FLAG wash buffer but also containing 3× FLAG peptide (100 μg/ml, Sigma Aldrich)]. Concentration of

purified protein was measured by BCA assay (Thermo Fisher Scientific # PI23225); protein was flash-frozen in liquid nitrogen and stored in elution buffer at –80° C. A typical preparation yielded 1 mg of eIF2 from a 12-liter culture.

Purification of human eIF2α

Human eIF2 was *E. coli* codon-optimized, synthesized and cloned into a pUC57 vector by GenScript Inc. PCR-amplified dsDNA fragments containing the eIF2α sequence were cloned into a pET28a vector using an In-Fusion HD Cloning Kit (Takara Bio), resulting in the kanamycin-resistant expression plasmid, pAA007. pAA007 was co-transformed into One Shot BL21 Star (DE3) chemically competent E. coli cells (Invitrogen), along with the tetracycline-inducible, chloramphenicol-resistant plasmid, pG-Tf2, containing the chaperones groES, groEL, and tig (Takara Bio). Transformed cells were grown in Luria broth containing kanamycin and chloramphenicol at 37°C on an orbital shaker.

When the culture reached an OD600 of ~0.2, 1ng/mL tetracycline was added to induce expression of chaperones. At an OD600 of ~0.8, the temperature was reduced to 16°C, eIF2α expression was induced with 1 mM IPTG (Gold Biotechnology) and the culture was grown for 16 hours. Cells were harvested and lysed with EmulsiFlex-C3 (Avestin) in a buffer containing 100 mM HEPES-KOH, pH 7.5, 300 mM KCl, 2 mM dithiothreitol (DTT), 5 mM $MgCl_2$, 5 mM imidazole, 10% glycerol, 0.1% NP-40, and complete EDTA-free protease inhibitor cocktail (Roche). The lysate was clarified at 10,000g for 60 min at 4°C. Subsequent purification steps were conducted on the ÄKTA Pure (GE Healthcare) system at 4°C.

The clarified lysate was loaded onto a 5-ml HisTrap FF Crude column (GE Healthcare), washed in a buffer containing 20 mM HEPES-KOH, pH 7.5, 100 mM KCl, 5% glycerol, 1 mM

DTT, 5 mM $MgCl_2$, 0.1% NP-40, and 20 mM imidazole, and eluted with 75-ml linear gradient of 20 to 500 mM imidazole. The eIF2α containing fractions were then collected and applied to a MonoS HR 10/10 (GE Healthcare) equilibrated in a buffer containing 20 mM HEPES-KOH, pH 7.5, 100 mM KCl, 1 mM DTT, 5% glycerol, and 5 mM $MgCl_2$. The column was washed in the same buffer and eluted with a 75-mL linear gradient of 100 mM to 1 M KCl. eIF2α containing fractions were collected and concentrated with an Amicon Ultra-15 concentrator (EMD Millipore) with a 30,000-dalton molecular mass cutoff and chromatographed on a Superdex 75 10/300 GL (GE Healthcare) column equilibrated in a buffer containing 20 mM HEPES-KOH, pH 7.5, 100 mM KCl, 1 mM TCEP, 5 mM $MgCl_2$, and 5% glycerol. A typical preparation yielded approximately 2 mg of eIF2α from a 1-liter culture.

Purification of phosphorylated human eIF2α

eIF2α and PKR were expressed and purified as above, but with the following modifications: One Shot BL21 Star (DE3) *E. coli* were co-transformed with pAA007, pG-Tf2, a third plasmid expressing the kinase domain of PERK (PERK 4: PERKKD-pGEX4T-1, Addgene plasmid #21817 donated by Dr. David Ron) and a resistance marker towards ampicillin. Transformed bacteria were grown in Luria broth containing ampicillin, kanamycin, and chloramphenicol. For purification, 1x PhosSTOP (Roche) was added to the lysis and purification buffers. Phosphorylation was confirmed by Phos-Tag SDS-PAGE (Wako) as described previously (*38*), and by Western blot with an eIF2α S51 phosphorylation-specific antibody (Cell Signaling, #9721).

Purification of tetrameric eIF2B(βγδε)

Tetrameric eIF2B(βγδε) and tetrameric eIF2B(βγδε) mutant proteins were purified using the same protocol as described for the decamer with the exception that expression strains were cotransformed without the eIF2B a subunit expressing plasmid. A typical preparation yielded approximately 0.75 mg of eIF2B(βγδε) from a 1-liter culture.

eIF2B(βγδε) tetramer with co-transformed plasmids: pJT073, pJT074

βN132D eIF2B(βγδε) tetramer with co-transformed plasmids: pAA012, pJT074

δR250A eIF2B(βγδε) tetramer with co-transformed plasmids: pAA013, pJT074

δR250E eIF2B(βγδε) tetramer with co-transformed plasmids: pAA014, pJT074

Cloning of mutant eIF2B expression plasmids

Mutant eIF2B constructs were generated by site-directed mutagenesis on pJT073 for β and δ, and pJT066 for α, using the primer indicated and its reverse complement.

βN132D (pAA012): 5′-

CCACTACGCTCAGCTGCAGTCTGACATCATCGAAGCTATCAACG-3′

δR250A (pAA013): 5′-

CCCCGCCGAACGAAGAACTGTCTGCTGACCTGGTTAACAAACTGAAACCG-3′

δR250E (pAA014): 5′-

CCCCGCCGAACGAAGAACTGTCTGAGGACCTGGTTAACAAACTGAAACCG-3′

EM sample preparation and data collection for ISRIB-bound eIF2•eIF2B and eIF2α•eIF2B complexes

Decameric eIF2B$(\alpha\beta\gamma\delta\varepsilon)_2$ + eIF2$(\alpha\beta\gamma)$ + ISRIB: eIF2B$(\alpha\beta\gamma\delta\varepsilon)_2$ was diluted to 800 nM eIF2B, eIF2 to 2 μM, and a stock solution of 200 μM ISRIB in N-methyl-2-pyrrolidone (NMP) was added to a final ISRIB concentration of 2 μM in a final solution containing 20 mM HEPES-KOH, pH 7.5, 100 mM KCl, 1 mM TCEP, 5 mM $MgCl_2$, 0.1% NMP, and incubated on ice for 10 min. An inter-amine bifunctional crosslinker (Pierce premium BS3, #PG82084) was then added at a concentration of 0.25mM, and the mixture was incubated on ice for 2 hours before quenching with 10mM Tris HCl.

Decameric eIF2B$(\alpha\beta\gamma\delta\varepsilon)_2$ + eIF2α(P): eIF2B$(\alpha\beta\gamma\delta\varepsilon)_2$ was diluted to 800 nM and eIF2α(P) to 2.4 μM in a final solution containing 20 mM HEPES-KOH, pH 7.5, 100 mM KCl, 1 mM TCEP, 5 mM $MgCl_2$, 0.1% NMP, and incubated on ice for 10 min and cross-linked as described above.

Each sample was applied to Quantifoil R 1.2/1.3 200 or 400 Au mesh grids (Quantifoil, Germany). Quantifoil grids were used without glow discharging. Using a Vitrobot Mark IV at 4°C and 100% humidity, 3.5 μl of sample was applied to the grid, incubated for an additional 10s, then blotted with 0 mm offset for ~6 s and plunge-frozen in liquid ethane. Two data sets were collected. Both data sets were collected with on a 300 kV Titan Krios at UCSF using a K2 Summit detector operated in super-resolution mode; 3233 images for eIF2P•eIF2B and 3947 images for eIF2•eIF2B were collected at a magnification of 29,000× (0.41Å per super-resolution pixel, binned by a factor of 2 to 0.82Å for subsequent processing). Dose-fractionated stacks were collected according to the parameters in Table S1.

Image analysis and 3D reconstruction

All dose-fractionated image stacks were corrected for motion artifacts, 2× binned in the Fourier domain, and dose-weighted using MotionCor2 (*39*), resulting in one dose-weighted and one unweighted integrated image per stack with pixel sizes of 0.822 Å. The parameters of the contrast transfer function (CTF) were estimated using GCTF-v1.06 (*40*) and the motion-corrected but unweighted images; automated particle picking was done using Gautomatch-v0.53 and averaged in 2D using Cryosparc v0.6.5 (*41*). For the 3D reconstruction, an ab initio reconstruction was done without symmetry, followed by homogeneous refinement. High-resolution homogeneous refinement was then performed in cryoSPARC, using dynamic masks and imposed C2 symmetry for eIF2P bound to eIF2B and 2 eIF2 bound to eIF2B, C1 symmetry was used for 1 eIF2 bound to eIF2B. All maps were low-pass filtered and sharpened in cryoSPARC. Molecular graphics and analyses were performed with the UCSF Chimera package. UCSF Chimera is developed by the Resource for Biocomputing, Visualization, and Informatics and supported by NIGMS P41-GM103311 (*42*). Accession numbers for the structures are as follows: EMD-XXXX, EMD-XXXX, EMD-XXXX (density maps; Electron Microscopy Data Bank).

Atomic modeling and validation

For all models, previously determined structures of the human eIF2B complex [PDB: 6CAJ (*8*)], human eIF2 alpha [PDBs: 1Q8K and 1KL9], the C-terminal HEAT domain of eIF2B epsilon [PDB: 3JUI], and mammalian eIF2 gamma [PDB: 5K0Y] were used for initial atomic interpretation. The models were manually adjusted and rebuilt in *Coot* (*43*) and then refined in

phenix.real_space_refine (*44*) using global minimization, morphing, secondary structure restraints, and local grid search. Then iterative cycles of manually rebuilding in *Coot* and phenix.real_space_refine, with previous strategies and additionally B-factor refinement, were performed. The final model statistics were tabulated using Molprobity (*45*) (Table S3). Map versus atomic model FSC plots were computed after masking using EMAN2 (*46*) calculated density maps from e2pdb2mrc.py with heteroatoms (ISRIB) and per-residue B-factor weighting. Solvent accessible surfaces and buried surface areas were calculated from the atomic models using UCSF Chimera. Final atomic models have been deposited at the PDB with the following accession codes: 1 eIF2•eIF2B•ISRIB (6O85); 2 eIF2•eIF2B•ISRIB (6O81); phosphorylated eIF2α•eIF2B (6O9Z). All structural figures were generated with UCSF Chimera (*42*) and BLENDER (http://www.blender.org).

GDP exchange assay

In vitro detection of GDP binding to eIF2 was adapted from a published protocol for a fluorescence intensity–based assay describing dissociation of eIF2 and nucleotide (*14*). We modified the procedure to establish a loading assay for fluorescent GDP as described (*20*). For the "GDP loading assay," purified eIF2 (200 pmol) was incubated with a molar equivalent Bodipy-FL-GDP (Thermo Fisher Scientific) in assay buffer (20 mM HEPES, pH 7.5, 100 mM KCl, 5 mM $MgCl_2$, 1 mM TCEP, 0.1% NMP, and 1 mg/ml bovine serum albumin) to a volume of 18 μl in 384 square-well black-walled, clear-bottom polystyrene assay plates (Corning). The reaction was initiated by addition of 2 μl of buffer or purified wild-type and mutant eIF2B(βγδε) (2 pmol) under various conditions to compare nucleotide exchange rates. For comparison of tetramer or ISRIB-assembled octamer, eIF2B(βγδε) (2 pmol) was preincubated in 0.1% NMP

and 2 mM ISRIB for 15 min before 10-fold dilution into the final reaction. These concentrations of vehicle and ISRIB were used throughout unless otherwise specified. Fluorescence intensity for both loading and unloading assays was recorded every 10 s for 60 or 100 min using a TECAN M1000 Pro plate reader (excitation wavelength: 495 nm, bandwidth 5 nm, emission wavelength: 512 nm, bandwidth: 5 nm). Data collected were fit to a first-order exponential.

ACKNOWLEDGEMENTS

Rights to the invention have been licensed by UCSF to Calico. We thank E. Pavolcak, J. Peschek, E. Karagöz, M. Boone, V. Belyy, G. Narlikar, R. Vale, the PHENIX and cryoSPARC developers, and members of the Walter and Frost labs for reagents, technical advice, and helpful discussions; M. Braunfeld, D. Bulkley, and M. Harrington of the UCSF Center for Advanced CryoEM, which are supported by NIH grants S10OD020054 and 1S10OD021741 and the Howard Hughes Medical Institute (HHMI); Z. Yu and H. Chou of the CryoEM Facility at the HHMI Janelia Research Campus; the QB3 shared cluster and NIH grant 1S10OD021596-01 for computational support; and G. Pavitt for the GP6452 yeast strain used in the purification of eIF2. A Titan X Pascal used for this research was donated by the NVIDIA Corporation.

Funding: This work was supported by an HHMI Faculty Scholar grant (A.F.) and by Calico Life Sciences LLC, the Rogers Family Foundation, the Weill Foundation, and HHMI (P.W.). L.R.K. was supported by a graduate research fellowship from the N.S.F. A.F. is a Chan Zuckerberg Biohub Investigator, and P.W. is an Investigator of HHMI.

REFERENCES

1. H. P. Harding *et al.*, An integrated stress response regulates amino acid metabolism and resistance to oxidative stress. *Mol. Cell*. **11**, 619–33 (2003).
2. L. R. Palam, T. D. Baird, R. C. Wek, Phosphorylation of eIF2 Facilitates Ribosomal Bypass of an Inhibitory Upstream ORF to Enhance *CHOP* Translation. *J. Biol. Chem.* **286**, 10939–10949 (2011).
3. K. M. Vattem, R. C. Wek, Reinitiation involving upstream ORFs regulates ATF4 mRNA translation in mammalian cells. *Proc. Natl. Acad. Sci.* **101**, 11269–11274 (2004).
4. Y. Gordiyenko *et al.*, eIF2B is a decameric guanine nucleotide exchange factor with a γ2ε2 tetrameric core. *Nat. Commun.* **5**, 3902 (2014).
5. K. Kashiwagi *et al.*, Crystal structure of eukaryotic translation initiation factor 2B. *Nature*. **531**, 122–125 (2016).
6. B. Kuhle, N. K. Eulig, R. Ficner, Architecture of the eIF2B regulatory subcomplex and its implications for the regulation of guanine nucleotide exchange on eIF2. *Nucleic Acids Res.* **43**, gkv930 (2015).
7. K. Dev *et al.*, The beta/Gcd7 subunit of eukaryotic translation initiation factor 2B (eIF2B), a guanine nucleotide exchange factor, is crucial for binding eIF2 in vivo. *Mol. Cell. Biol.* **30**, 5218–33 (2010).
8. G. D. Pavitt, K. V Ramaiah, S. R. Kimball, A. G. Hinnebusch, eIF2 independently binds two distinct eIF2B subcomplexes that catalyze and regulate guanine-nucleotide exchange. *Genes Dev.* **12**, 514–26 (1998).
9. S. R. Kimball, J. R. Fabian, G. D. Pavitt, A. G. Hinnebusch, L. S. Jefferson, Regulation of guanine nucleotide exchange through phosphorylation of eukaryotic initiation factor

eIF2alpha. Role of the alpha- and delta-subunits of eiF2b. *J. Biol. Chem.* **273**, 12841–5 (1998).

10. W. Yang, A. G. Hinnebusch, Identification of a regulatory subcomplex in the guanine nucleotide exchange factor eIF2B that mediates inhibition by phosphorylated eIF2. *Mol. Cell. Biol.* **16**, 6603–6616 (1996).
11. T. Krishnamoorthy, G. D. Pavitt, F. Zhang, T. E. Dever, A. G. Hinnebusch, Tight Binding of the Phosphorylated Subunit of Initiation Factor 2 (eIF2) to the Regulatory Subunits of Guanine Nucleotide Exchange Factor eIF2B Is Required for Inhibition of Translation Initiation. *Mol. Cell. Biol.* **21**, 5018–5030 (2001).
12. C. Sidrauski *et al.*, Pharmacological brake-release of mRNA translation enhances cognitive memory. *Elife*. **2** (2013), doi:10.7554/eLife.00498.
13. C. Sidrauski *et al.*, Pharmacological dimerization and activation of the exchange factor eIF2B antagonizes the integrated stress response. *Elife*. **4** (2015), doi:10.7554/eLife.07314.
14. Y. Sekine *et al.*, Stress responses. Mutations in a translation initiation factor identify the target of a memory-enhancing compound. *Science*. **348**, 1027–30 (2015).
15. A. Chou *et al.*, Inhibition of the integrated stress response reverses cognitive deficits after traumatic brain injury. *Proc. Natl. Acad. Sci. U. S. A.* **114**, E6420–E6426 (2017).
16. M. Halliday *et al.*, Partial restoration of protein synthesis rates by the small molecule ISRIB prevents neurodegeneration without pancreatic toxicity. *Cell Death Dis.* **6**, e1672 (2015).
17. Y. L. Wong *et al.*, eIF2B activator prevents neurological defects caused by a chronic Integrated Stress Response. *bioRxiv*, 462820 (2018).
18. Y. L. Wong *et al.*, The small molecule ISRIB rescues the stability and activity of

Vanishing White Matter Disease eIF2B mutant complexes. *Elife*. **7** (2018), doi:10.7554/eLife.32733.

19. H. H. Rabouw *et al.*, The small molecule ISRIB suppresses the integrated stress response within a defined window of activation. *Proc. Natl. Acad. Sci.* (2019).

20. J. C. Tsai *et al.*, Structure of the nucleotide exchange factor eIF2B reveals mechanism of memory-enhancing molecule. *Science*. **359**, eaaq0939 (2018).

21. A. F. Zyryanova *et al.*, Binding of ISRIB reveals a regulatory site in the nucleotide exchange factor eIF2B. *Science*. **359**, 1533–1536 (2018).

22. R. A. de Almeida *et al.*, A Yeast Purification System for Human Translation Initiation Factors eIF2 and eIF2Bε and Their Use in the Diagnosis of CACH/VWM Disease. *PLoS One*. **8**, e53958 (2013).

23. T. Ito, A. Marintchev, G. Wagner, Solution Structure of Human Initiation Factor eIF2α Reveals Homology to the Elongation Factor eEF1B. *Structure*. **12**, 1693–1704 (2004).

24. S. Dhaliwal, D. W. Hoffman, The Crystal Structure of the N-terminal Region of the Alpha Subunit of Translation Initiation Factor 2 (eIF2α) from Saccharomyces cerevisiae Provides a View of the Loop Containing Serine 51, the Target of the eIF2α-specific Kinases. *J. Mol. Biol.* **334**, 187–195 (2003).

25. J. Wei *et al.*, Crystal structure of the C-terminal domain of the ε subunit of human translation initiation factor eIF2B. *Protein Cell*. **1**, 595–603 (2010).

26. T. Boesen, S. S. Mohammad, G. D. Pavitt, G. R. Andersen, Structure of the Catalytic Fragment of Translation Initiation Factor 2B and Identification of a Critically Important Catalytic Residue. *J. Biol. Chem.* **279**, 10584–10592 (2004).

27. B. Eliseev *et al.*, Structure of a human cap-dependent 48S translation pre-initiation

complex. *Nucleic Acids Res.* **46**, 2678–2689 (2018).

28. V. Beilsten-Edmands *et al.*, eIF2 interactions with initiator tRNA and eIF2B are regulated by post-translational modifications and conformational dynamics. *Nat. Publ. Gr.*, 1 (2015).

29. E. Dubiez, A. Aleksandrov, C. Lazennec-Schurdevin, Y. Mechulam, E. Schmitt, Identification of a second GTP-bound magnesium ion in archaeal initiation factor 2. *Nucleic Acids Res.* **43**, 2946–2957 (2015).

30. J. L. Llácer *et al.*, Conformational Differences between Open and Closed States of the Eukaryotic Translation Initiation Complex. *Mol. Cell*. **59**, 399–412 (2015).

31. S. S. Mohammad-Qureshi, M. D. Jennings, G. D. Pavitt, Clues to the mechanism of action of eIF2B, the guanine-nucleotide-exchange factor for translation initiation. *Biochem. Soc. Trans.* **36**, 658–664 (2008).

32. M. D. Jennings, Y. Zhou, S. S. Mohammad-Qureshi, D. Bennett, G. D. Pavitt, eIF2B promotes eIF5 dissociation from eIF2*GDP to facilitate guanine nucleotide exchange for translation initiation. *Genes Dev.* **27**, 2696–707 (2013).

33. M. D. Jennings, G. D. Pavitt, Erratum: eIF5 has GDI activity necessary for translational control by eIF2 phosphorylation. *Nature*. **468**, 122–122 (2010).

34. R. Elsby *et al.*, The alpha subunit of eukaryotic initiation factor 2B (eIF2B) is required for eIF2-mediated translational suppression of vesicular stomatitis virus. *J. Virol.* **85**, 9716–25 (2011).

35. G. D. Pavitt, W. Yang, A. G. Hinnebusch, Homologous segments in three subunits of the guanine nucleotide exchange factor eIF2B mediate translational regulation by phosphorylation of eIF2. *Mol. Cell. Biol.* **17**, 1298–313 (1997).

36. C. R. Vazquez de Aldana, A. G. Hinnebusch, Mutations in the GCD7 subunit of yeast

guanine nucleotide exchange factor eIF-2B overcome the inhibitory effects of phosphorylated eIF-2 on translation initiation. *Mol. Cell. Biol.* **14**, 3208–22 (1994).

37. N. C. Wortham, M. Martinez, Y. Gordiyenko, C. V. Robinson, C. G. Proud, Analysis of the subunit organization of the eIF2B complex reveals new insights into its structure and regulation. *FASEB J.* **28**, 2225–2237 (2014).

38. A. Crespillo-Casado *et al.*, A Sephin1-insensitive tripartite holophosphatase dephosphorylates translation initiation factor 2α. *J. Biol. Chem.* **293**, 7766–7776 (2018).

39. S. Q. Zheng *et al.*, MotionCor2: anisotropic correction of beam-induced motion for improved cryo-electron microscopy. *Nat. Methods*. **14**, 331–332 (2017).

40. K. Zhang, Gctf: Real-time CTF determination and correction. *J. Struct. Biol.* **193**, 1–12 (2016).

41. A. Punjani, J. L. Rubinstein, D. J. Fleet, M. A. Brubaker, cryoSPARC: algorithms for rapid unsupervised cryo-EM structure determination. *Nat. Methods*. **14**, 290–296 (2017).

42. E. F. Pettersen *et al.*, UCSF Chimera: A visualization system for exploratory research and analysis. *J. Comput. Chem.* **25**, 1605–1612 (2004).

43. P. Emsley, B. Lohkamp, W. G. Scott, K. Cowtan, Features and development of *Coot*. *Acta Crystallogr. Sect. D Biol. Crystallogr.* **66**, 486–501 (2010).

44. P. D. Adams *et al.*, *PHENIX* : a comprehensive Python-based system for macromolecular structure solution. *Acta Crystallogr. Sect. D Biol. Crystallogr.* **66**, 213–221 (2010).

45. V. B. Chen *et al.*, *MolProbity* : all-atom structure validation for macromolecular crystallography. *Acta Crystallogr. Sect. D Biol. Crystallogr.* **66**, 12–21 (2010).

46. S. J. Ludtke, Single-Particle Refinement and Variability Analysis in EMAN2.1. *Methods Enzymol.* **579**, 159–89 (2016).

Chapter 3

Structural insights into a memory-enhancing inhibitor of the integrated stress response

Structural insights into a memory-enhancing inhibitor of the integrated stress response

Aditya A. Anand[1,2*], Peter Walter[1,2]

[1] Department of Biochemistry and Biophysics, University of California at San Francisco, San Francisco, CA, USA

[2] Howard Hughes Medical Institute

*Correspondence to: AAA: aditya@walterlab.ucsf.edu Genentech Hall, N316 600 16th Street San Francisco, CA 94158

This work was first appeared in The FEBS Journal at http://doi.org/10.1111/febs.15073

ABSTRACT

The integrated stress response regulates protein synthesis under conditions of stress. Phosphorylation of translation initiation factor eIF2 by stress-sensing kinases converts eIF2 from substrate to competitive inhibitor of its dedicated nucleotide exchange factor, eIF2B, arresting translation. A drug-like molecule called ISRIB reverses the effects of eIF2 phosphorylation and restores translation by targeting eIF2B. When administered to mice, ISRIB enhances cognition and limits cognitive decline due to brain injury. To determine ISRIB's mechanism of action we solved an atomic structure of ISRIB bound to the human eIF2B decamer. We found that ISRIB acts as a molecular staple, pinning together tetrameric subcomplexes of eIF2B along the assembly path to a fully-active, decameric enzyme. In this Structural Snapshot, we discuss ISRIB's mechanism, its ability to rescue disease mutations in eIF2B and conservation of the enzyme and ISRIB binding pocket.

INTRODUCTION

Proteins execute the majority of cellular functions and thus regulation of protein synthesis is vital for cell growth, health and survival. Translation initiation in particular offers a proteome-wide control point. The integrated stress response (ISR), a cellular signaling network, couples the detection of cellular stresses to the inhibition of translation initiation. Four kinases sense stress: PERK detects the accumulation of unfolded proteins in the lumen of the endoplasmic reticulum, PKR senses double-stranded RNA, GCN2 responds to amino acid deprivation, and HRI senses heme deficiency. Once activated, these kinases converge on the alpha subunit of eukaryotic translation initiation factor 2 (eIF2) at serine 51.

eIF2, a heterotrimeric GTPase composed of α, β and γ subunits, can bind GTP and methionine initiator tRNA to form a ternary complex. In conjunction with translation machinery, ternary complex scans along the 5' untranslated region of mRNAs to detect the translation start site. Once the AUG start codon is decoded, GTP is hydrolyzed and eIF2-GDP is released as a binary complex from the ribosome. Exchange of GDP for GTP enables a new round of translation initiation. This occurs with the aid of a dedicated nucleotide exchange factor, translation initiation factor 2B (eIF2B).

eIF2B is a decameric nucleotide exchange factor composed of two copies of subunits α, β, γ, δ and ε. Upon ISR-induced phosphorylation, eIF2 is converted from substrate to competitive inhibitor of eIF2B, arresting general protein synthesis and upregulating translation of a select few mRNAs containing upstream open reading frames. These mRNAs encode stress-responsive factors such as the transcription factor ATF4.

A small drug-like molecule called ISRIB (integrated stress response inhibitor) targets eIF2B (1, 2) and, remarkably, enhances cognition in mice (3). In rodents, ISRIB is effective in a number of

disease models: treatment with the molecule can reverse cognitive deficits following traumatic brain injury (4), protect against prion-induced neurodegeneration (5), and prevent metastasis of a subset of cancers . In vitro studies determined that ISRIB activates and stabilizes a decameric eIF2B complex (6). To determine ISRIB's mechanism of action we solved a structure of the small molecule-bound eIF2B complex.

Structure of ISRIB-bound human eIF2B

We established a recombinant expression and purification system for the five subunits of eIF2B that self-assemble in E. coli to form a stable decamer. We imaged this complex in the presence of ISRIB by cryo-electron microscopy and determined a 2.8Å average resolution structure that identified the binding site and coordination of the small molecule (Figure 3.1). Our interpretation of the density afforded modeling of the majority of the ten-subunit decamer, with the exception of the flexible "ear" domains of eIF2Bγ and the leashed "HEAT" domain of eIF2Bε that is itself sufficient for basal catalytic activity. Future studies are aimed at resolving these critical regions. A 2.7Å resolution core enabled more accurate modeling of ISRIB and identification of residues important for it activity. Our density for ISRIB is best explained by the drug binding as multiple conformers, each with a pair related by 180° rotation. Further, our interpretation of the density indicated that eIF2B βH188 contributes to ISRIB binding by forming a C-H-pi bond with the methylene bridge adjacent to the ether oxygen on ISRIB. Replacement of this histidine with either tyrosine or phenylalanine enhanced ISRIB binding, serving to validate our observation. A number of other residues contribute to the shape specificity and hydrophobicity of the pocket, and are critical for ISRIB binding. For example, eIF2Bδ L179 blocks binding of a methylated ISRIB analog, presumably due to steric hindrance. This methylated ISRIB has greatly reduced

activity that can be restored by mutation of leucine to alanine. Given this information one may surmise that ISRIB efficacy can be improved by enhancing shape complementarity towards the binding pocket. This observation may explain the high efficacy of a di-halogenated ISRIB that can occupy greater space within the binding pocket.

ISRIB mechanism of action

By analyzing eIF2B in the presence and absence of ISRIB using cryoEM and analytical ultracentrifugation techniques, we determined a functional model of ISRIB action. ISRIB staples together tetrameric eIF2B(βγδε) subcomplexes to form a more active octameric eIF2B(βγδε)2, that in turn possesses an avid binding surface for the dimeric alpha subunits. Consolidation of the alpha homodimer and the ISRIB-bound octamer produces the fully-active decamer, eIF2B(αβγδε)2. We surmise that the octameric and decameric complexes have greater activity when compared to the tetramer due to enhanced surface area for substrate binding. These differences in binding have been observed previously.

Given that ISRIB minimally activates a decameric complex isolated by size exclusion, we propose that complex assembly explains the majority of ISRIB action. Minute allosteric changes within the enzyme cannot be excluded at this time.

Interactions with eIF2 and phosphorylated eIF2

Crosslinking studies of S. pombe eIF2B (7) revealed that multiple eIF2B subunits mediate binding of the eIF2 heterotrimer. In particular, eIF2α was found to contact the three proteins of the regulatory subcomplex, eIF2B(αβδ)2, suggesting that it binds across the dimer interface.

Based on this data, it is plausible that binding of eIF2 is substantially enhanced by the composite binding surface present in the full eIF2B decamer.

Binding of eIF2α likely promotes productive interaction between the GTP-binding domain in eIF2γ and the flexibly attached eIF2Bε-HEAT by ensuring their close proximity. In its phosphorylated form, eIF2 may simply bind more tightly and sequester the limiting eIF2B to prevent exchange, or there may be additional conformational changes involved with more complex outcomes. Future structural studies aim to distinguish between these hypotheses.

Early studies of yeast eIF2B identified a number of mutations that regulate control of amino acid synthesis and the integrated stress response (8–11). Many of these were proposed to modulate binding to phosphorylated eIF2. However, with data that enhanced complex stability can reverse the ISR, it is conceivable that a destabilized eIF2B can constitutively activate the ISR independent of eIF2 phosphorylation. An analysis of how these mutations affect eIF2B stability, and how ISRIB acts in these contexts would be valuable.

Vanishing White Matter Disease

Numerous mutations in subunits of eIF2B lead to a neurodegenerative disease known as Vanishing White Matter Disease (VWMD). VWMD mutations have been identified in all eIF2B subunits (Figure 3.2A-C), with many clustering in the eIF2Bε subunit. Since catalysis is essential, these mutations likely affect the structural stability of the protein, the entire eIF2B complex or binding to eIF2.

Previous research demonstrated that VWMD mutations can lead to a decrease in GEF activity. Furthermore, Wong et al. reported that eIF2B activation can rescue defects in GEF activity due to VWMD mutations and ameliorate disease in rodent models (12, 13). A particularly deleterious

variant, δR483W, was dramatically restored to near full activity by ISRIB in cells. This mutation lies directly outside the ISRIB pocket (Figure 3.2D) and, when analyzed by size-exclusion chromatography, promotes dissociation of eIF2B into tetrameric subcomplexes. Given our findings on ISRIB action, it is plausible that ISRIB prevents complex dissociation by stapling eIF2B across its symmetry axis. Thus, ISRIB may have a particularly strong effect on mutations that destabilize eIF2B assembly. Two additional proximal mutations, βE213 and δY489, may similarly be rescued by ISRIB, though this remains to be shown. Finally, mutations distal to the ISRIB binding site that cause defective GEF activity may also be rescued by ISRIB through the molecule's ability to favor decameric complex production. We predict that the VWMD mutations resistant to ISRIB activity would be those that affect ISRIB binding directly or critically impair dimerization or binding to eIF2.

Conservation of eIF2B and ISRIB pocket

Structures of eIF2B show a conserved organization of subunits between S. pombe and H. sapiens. Furthermore, a tetrameric structure of C. thermophilum eIF2Bβ and eIF2Bδ indicates the likelihood of a similar arrangement (14). The eIF2B sequence is well-conserved from yeast to human as might be predicted from its critical role in translation initiation. Additionally the subunits of the regulatory subcomplex contain homology to archaeal sugar-phosphate isomerases, and subunits of the catalytic subcomplex are structurally similar to sugar transferases. These data raise the possibility that eIF2B may bind nucleotides or sugars that may regulate its function. Our structure of human eIF2B does not contain density that is immediately identifiable as nucleotide, but these possibilities remain open.

Intriguingly, the yeast eIF2B forms polymers under conditions of stress in vivo (15, 16). While this has not yet been shown for the mammalian counterpart, we ponder whether the extended "ear" domains of eIF2By may be involved in templating eIF2B filaments, and if this domain becomes stabilized in an elongated, multi-enzyme complex.

Strikingly, the cavity within which ISRIB binds is structurally conserved between S. pombe (Figure 3.3A), C. thermophilum (Figure 3.3B) and H. sapiens eIF2B. This raises the question of whether an endogenous ligand may bind within eIF2B and regulate its activity in a manner similar to ISRIB. Sequence alignments of eIF2B across yeast, zebrafish, fruit fly, round worm, mouse and human indicate that certain residues within the ISRIB pocket are more conserved than others (Figure 3.3E-F). The critical βH188 is not conserved in worms, flies or yeast, suggesting that ISRIB may not function in these organisms and that modifications of the compound may be required for use in these species. Empirical data is essential to validate these predictions.

We analyzed the structure using UCSF Chimera to visually render residues by conservation across eleven species (Figure 3.3C) as a saturation gradient of either blue or gold for eIF2Bb and eIF2Bd. Since eIF2B is a highly conserved enzyme, we amplified the differences in conservation by defining white as 50% conserved and the most saturated blue and gold as 100% conserved. As expected based on the sequence alignments, βH188 is a light blue in a close-up view of the ISRIB pocket (Figure 3.3D), as are other pocket residues. This suggests that the bonds between the enzyme and molecules within the pocket can change by species.

Interestingly the residues adjacent to βH188, βF187 and βV189, are more highly conserved and point away from the pocket. These presumably stabilize the fold of the pocket. Taken together, these data suggest that the shape of the pocket is more conserved than the sequence lining the pocket. Thus, with the correct pharmacological tools, eIF2B may offer a species-specific control

of eukaryotic translation. Endogenous ligands, if they exist, may be specific to certain species. In humans, such a molecule would be of great interest, especially if it functions similarly to ISRIB in the nervous system.

ACKNOWLEDGEMENTS

This work is supported by a HHMI Faculty Scholar grant, the Searle Scholars Program, and NIH grant 1DP2GM110772-01 (A.F.) and by Calico Life Sciences LLC, the Rogers Family Foundation, the Weill Foundation, and HHMI (P.W.). A.F. is a Chan Zuckerberg Biohub Investigator, and P.W. is an Investigator of HHMI.

We thank J. Tsai, L. Miller-Vedam, and the Walter and Frost labs for technical advice, and helpful discussions; M. Braunfeld, D. Bulkley, and A. Myasnikov of the UCSF Center for Advanced CryoEM and D. Toso and P. Tobias of the Berkeley Bay Area CryoEM Facility, which are supported by NIH grants S10OD020054 and 1S10OD021741 and the Howard Hughes Medical Institute (HHMI); Z. Yu, R. Huang, and C. Hong of the CryoEM Facility at the HHMI Janelia Research Campus; the QB3 shared cluster and NIH grant 1S10OD021596-01 for computational support; and G. Pavitt for the GP6452 yeast strain used in the purification of eIF2. The Titan X Pascal used for this research was donated by the NVIDIA Corporation.

REFERENCES

1. C. Sidrauski et al., Pharmacological dimerization and activation of the exchange factor eIF2B antagonizes the integrated stress response. Elife. 4 (2015), doi:10.7554/eLife.07314.
2. Y. Sekine et al., Stress responses. Mutations in a translation initiation factor identify the target of a memory-enhancing compound. Science. 348, 1027–30 (2015).
3. C. Sidrauski et al., Pharmacological brake-release of mRNA translation enhances cognitive memory. Elife. 2 (2013), doi:10.7554/eLife.00498.
4. A. Chou et al., Inhibition of the integrated stress response reverses cognitive deficits after traumatic brain injury. Proc. Natl. Acad. Sci. U. S. A. 114, E6420–E6426 (2017).
5. M. Halliday et al., Partial restoration of protein synthesis rates by the small molecule ISRIB prevents neurodegeneration without pancreatic toxicity. Cell Death Dis. 6, e1672 (2015).
6. J. C. Tsai et al., Structure of the nucleotide exchange factor eIF2B reveals mechanism of memory-enhancing molecule. Science. 359, eaaq0939 (2018).
7. K. Kashiwagi et al., Crystal structure of eukaryotic translation initiation factor 2B. Nature. 531, 122–125 (2016).
8. G. D. Pavitt, K. V Ramaiah, S. R. Kimball, A. G. Hinnebusch, eIF2 independently binds two distinct eIF2B subcomplexes that catalyze and regulate guanine-nucleotide exchange. Genes Dev. 12, 514–26 (1998).
9. G. D. Pavitt, W. Yang, A. G. Hinnebusch, Homologous segments in three subunits of the guanine nucleotide exchange factor eIF2B mediate translational regulation by phosphorylation of eIF2. Mol. Cell. Biol. 17, 1298–313 (1997).
10. C. R. Vazquez de Aldana, A. G. Hinnebusch, Mutations in the GCD7 subunit of yeast

guanine nucleotide exchange factor eIF-2B overcome the inhibitory effects of phosphorylated eIF-2 on translation initiation. Mol. Cell. Biol. 14, 3208–22 (1994).

11. T. Krishnamoorthy, G. D. Pavitt, F. Zhang, T. E. Dever, A. G. Hinnebusch, Tight Binding of the Phosphorylated Subunit of Initiation Factor 2 (eIF2) to the Regulatory Subunits of Guanine Nucleotide Exchange Factor eIF2B Is Required for Inhibition of Translation Initiation. Mol. Cell. Biol. 21, 5018–5030 (2001).
12. Y. L. Wong et al., The small molecule ISRIB rescues the stability and activity of Vanishing White Matter Disease eIF2B mutant complexes. Elife. 7 (2018), doi:10.7554/eLife.32733.
13. Y. L. Wong et al., eIF2B activator prevents neurological defects caused by a chronic Integrated Stress Response. bioRxiv, 462820 (2018).
14. B. Kuhle, N. K. Eulig, R. Ficner, Architecture of the eIF2B regulatory subcomplex and its implications for the regulation of guanine nucleotide exchange on eIF2. Nucleic Acids Res. 43, gkv930 (2015).
15. E. Nueske et al., Filament formation by the translation factor eIF2B regulates protein synthesis in starved cells. bioRxiv, 467829 (2018).
16. G. Marini, E. Nueske, W. Leng, S. Alberti, G. Pigino, Adaptive reorganization of the cytoplasm upon stress in budding yeast. bioRxiv, 468454 (2018).

Figure 3.1

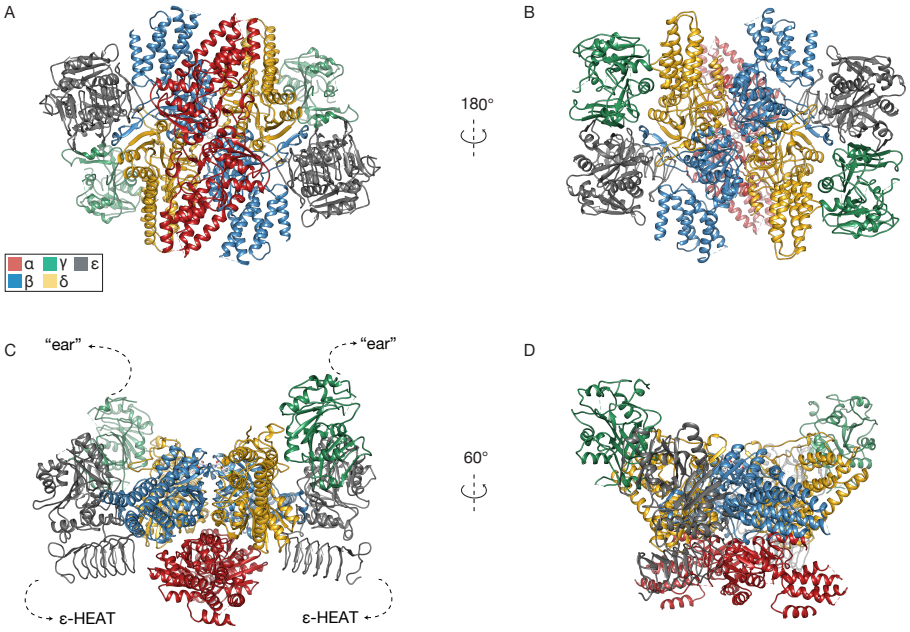

Human eIF2B bound to ISRIB. Four distinct views (A-D) of ISRIB-stabilized eIF2B with subunits colored in different shades (α in red, β in blue, γ in green, δ in gold, ε in gray, and ISRIB in CPK coloring). Dotted lines (C) indicate connection to the "ear" domains of gamma and HEAT domain of epsilon for which density is not clearly defined.

Figure 3.2

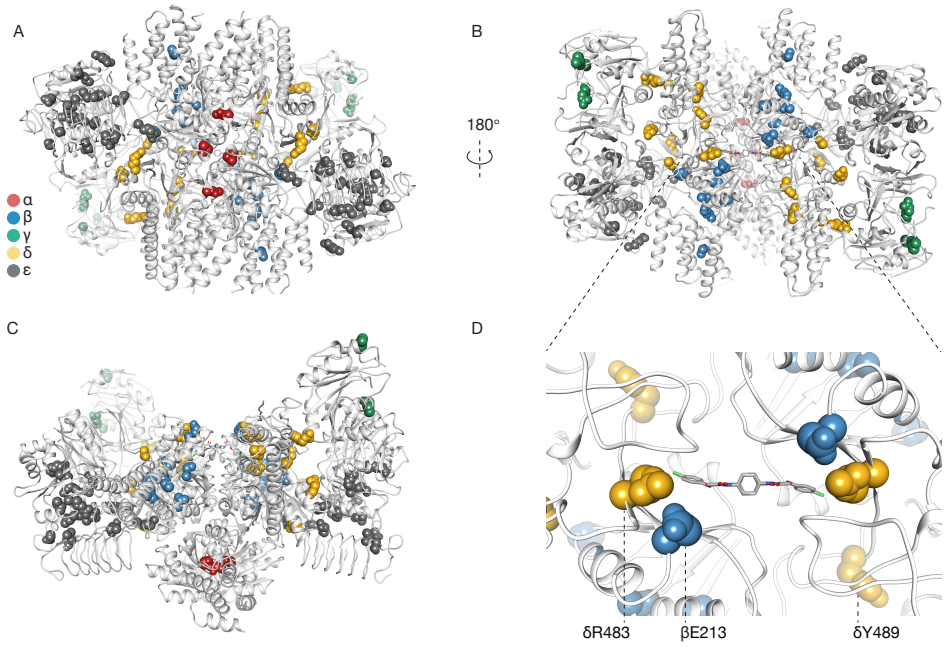

Vanishing white matter disease mutations. (A-C) Structure of human eIF2B depicted in light gray with disease mutations mapped in colored spheres (α in red, β in blue, γ in green, δ in gold, ε in gray). (D) Close-up view of ISRIB pocket labeled with the three most proximal identified mutations.

Figure 3.3

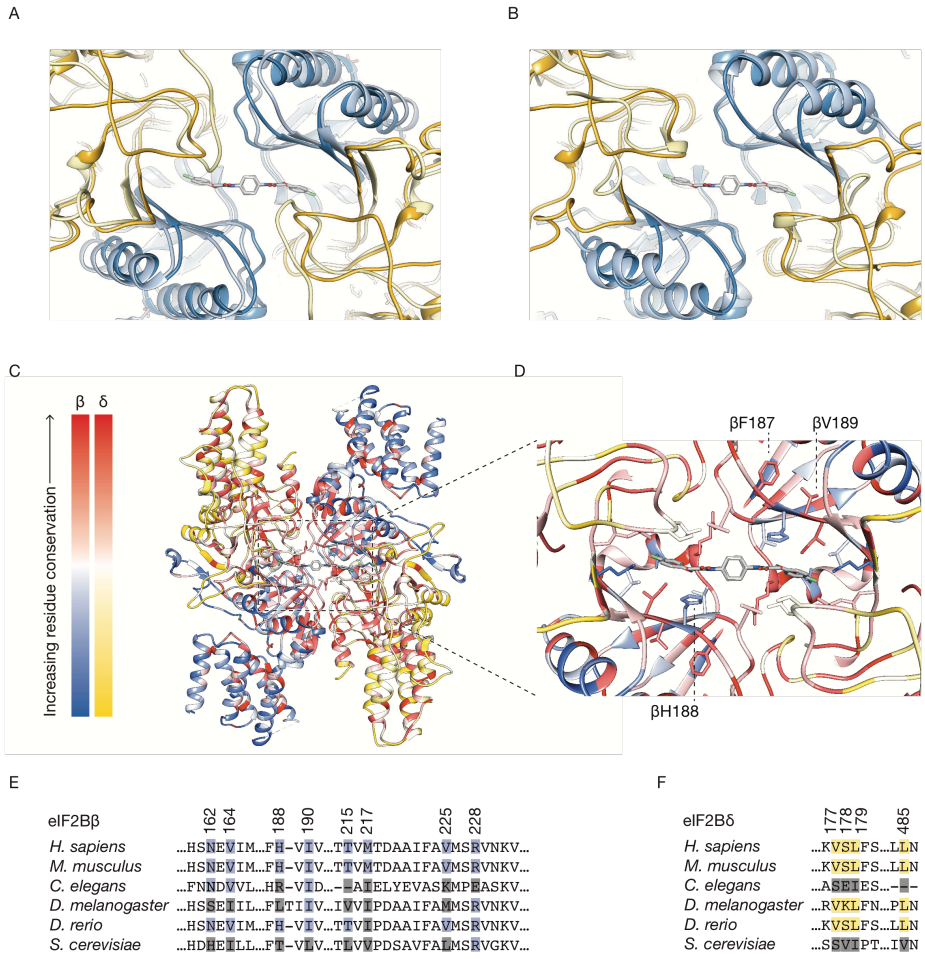

Conservation of the ISRIB pocket. eIF2Bβ and eIF2Bδ from (A) S. pombe and (B) C. thermophilum depicted in pale blue and pale gold respectively, and overlaid on the human structure (dark blue and gold, with ISRIB). (C) eIF2B tetrameric core rendered by residue conservation across 11 species (S. cerevisiae, S. pombe, C. elegans, D. melanogaster, D. rerio, X. laevis, M. musculus, R. norvegicus, B. taurus, H. sapiens). Extent of conservation is illustrated by saturation of blue for eIF2Bβ or gold eIF2Bδ. (D) Close-up view of ISRIB-binding pocket in C. (E-F) Sequence conservation for residues lining the ISRIB pocket highlighted in blue for eIF2Bβ and gold for eIF2Bδ.

Appendix A

Pharmacokinetics of ISRIB 1.5

Figure A.1

(A)

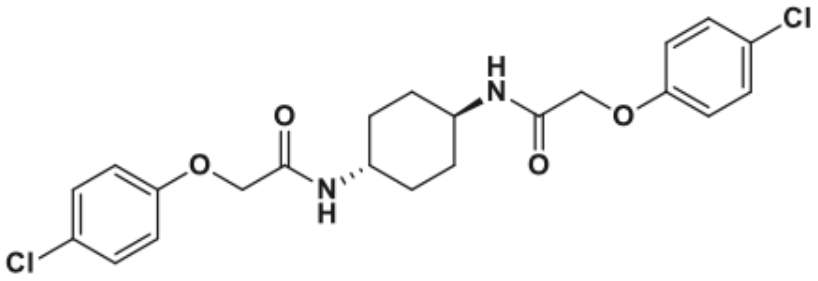

(B)

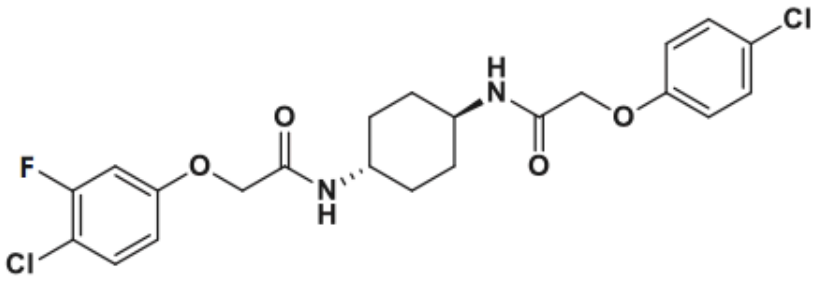

Structures. (A) ISRIB 1.0 and analog (B) ISRIB 1.5

Figure A.2

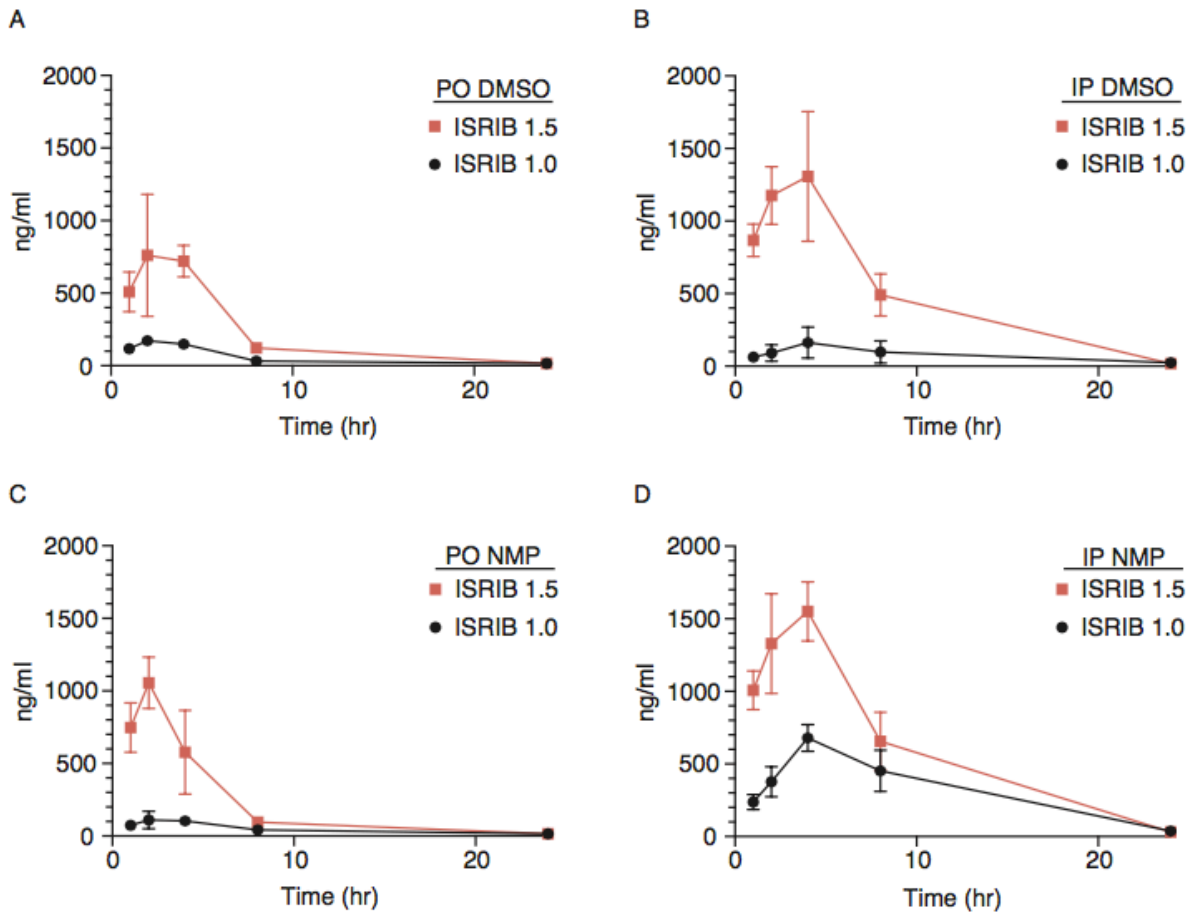

Pharmacokinetics summary. Plasma concentrations measured for (A) PO or (B) IP administration of ISRIB 1.0 and ISRIB 1.5 in a DMSO solvent. Plasma concentrations measured for (C) PO or (D) IP administration of ISRIB 1.0 and ISRIB 1.5 in a N-Methyl-2-pyrrolidone (NMP) solvent. Points displayed represent mean ± SD; n=3 for collection at 1, 2, 4, 8, and 24 hours after dosing.

Table A.1

Dosing route and volume

Ear tag	Weight (g)	ISRIB (solvent)	Route	Dosing Volume (µl)
341	30.6	1.0 (DMSO)	PO	306
342	28.1	1.0 (DMSO)	PO	281
343	30.8	1.0 (DMSO)	PO	308
344	30	1.0 (NMP)	PO	300
345	26.9	1.0 (NMP)	PO	269
346	30.7	1.0 (NMP)	PO	307
347	32.2	1.5 (DMSO)	PO	322
348	29.5	1.5 (DMSO)	PO	295
349	29	1.5 (DMSO)	PO	290
350	28.4	1.5 (NMP)	PO	284
351	27.6	1.5 (NMP)	PO	276
352	29.9	1.5 (NMP)	PO	299
353	30.2	1.0 (DMSO)	IP	302
354	30.1	1.0 (DMSO)	IP	301
355	26.4	1.0 (DMSO)	IP	264
356	29	1.0 (NMP)	IP	290
357	29.4	1.0 (NMP)	IP	294
358	26.8	1.0 (NMP)	IP	268
359	29.6	1.5 (DMSO)	IP	296
360	27.7	1.5 (DMSO)	IP	277
361	27.7	1.5 (DMSO)	IP	277
362	31.1	1.5 (NMP)	IP	311
363	31.2	1.5 (NMP)	IP	312
364	30.1	1.5 (NMP)	IP	301

MATERIALS AND METHODS

Formulation

ISRIB 1.0 or ISRIB 1.5 were prepared the day of administration and dissolved into 5 mg/ml in either DMSO or NMP by vortexing, heating, and sonication. Immediately prior to PO dosing nine volumes of HPMT was slowly added to 5 mg/ml solvent dissolved ISRIB to generate a milky suspension of 0.5 mg/ml. Mice were subsequently dosed at 10 ul/g. Immediately prior to IP dosing, solvent dissolved ISRIB 1.0 or ISRIB 1.5 was diluted to 4 mg/ml and combined 1:1 with PEG400. Mice were then dosed at 2.5 ul/g.

ACKNOWLEDGEMENTS

This work was done in collaboration with Byron Hann and Paul Phojanakong at the UCSF Preclinical Therapeutics Core. Design and conception by Jordan Tsai, Aditya Anand, and Peter Walter.

Publishing Agreement

It is the policy of the University to encourage open access and broad distribution of all theses, dissertations, and manuscripts. The Graduate Division will facilitate the distribution of UCSF theses, dissertations, and manuscripts to the UCSF Library for open access and distribution. UCSF will make such theses, dissertations, and manuscripts accessible to the public and will take reasonable steps to preserve these works in perpetuity.

I hereby grant the non-exclusive, perpetual right to The Regents of the University of California to reproduce, publicly display, distribute, preserve, and publish copies of my thesis, dissertation, or manuscript in any form or media, now existing or later derived, including access online for teaching, research, and public service purposes.

DocuSigned by:
Aditya Anand
5DE14CC562F0493...
Author Signature

8/26/2020
Date